

# Investigating the mechanism of cytotoxic lymphocyte resistance to perforin

Jesse Alexander Rudd-Schmidt

0000-0002-3033-2642

Master of Philosophy - MDHS (Medicine)

March 2020

The Sir Peter MacCallum Department of Oncology

Submitted in total fulfilment for the degree of Master  
of Philosophy - MDHS (Medicine) at the University of  
Melbourne

# Preface

The majority of the work performed during this masters degree has been included in the following publication:

**Rudd-Schmidt, J. A., Hodel, A. W., Noori, T., Lopez, J. A., Cho, H.-J., Verschoor, S., . . . Voskoboinik, I. (2019). Lipid order and charge protect killer T cells from accidental death. Nature Communications, 10(1), 5396. doi:10.1038/s41467-019-13385-x**

Co-author authorisation forms have been signed by all co-authors and submitted during the thesis submission process.

Sections of the text that describe experiments performed by co-author Dr Adrian Hodel are included for completeness of the study, and are clearly labelled in the text. A detailed methods section for the Atomic Force Microscopy experiments he conducted is included as Appendix 1 in this thesis.

Sections of text within the thesis which have originated from the published article are denoted by quotation marks, and the publication itself is included as Appendix 2 in this thesis.

Supplementary Videos 1,2 & 3 have been emailed to the examinations office.

Total word count including references and bibliography:

I, Jesse Alexander Rudd-Schmidt, declare that except where otherwise stated in the text, all work was performed by me.

Signature: \_\_\_\_\_

Date: \_\_\_\_\_

## **Abstract**

Cytotoxic lymphocytes are highly efficient killer cells of the immune system. They destroy cognate target cells by secreting highly toxic effector molecules, the pore-forming protein perforin and pro-apoptotic serine proteases granzymes, into the confines of the immune synapse. Despite both the lymphocyte and target cell plasma membrane being equally exposed to the perforin and granzymes, the lymphocytes invariably survive that encounter as they remain resistant to perforin pores. This project investigates the mechanisms behind this unique phenomenon.

# Acknowledgments

I would like to extend a most sincere thank you to everybody who has assisted me in undertaking this project!

Ilia, thank you so much for opportunity to manage my own project and to undertake this masters degree via the Research Training Scheme. Although I was hesitant to begin with, I never doubted it was a huge privilege, and I am very grateful that you encouraged me to do it. Same goes for getting me to fly around the world to conferences and collaborators facilities every other week! I love working in this lab, and thoroughly enjoy every moment spent researching and being creative!

Joe, thanks for your co-supervision and guidance throughout the preparation of both the manuscript and my thesis! I'm very glad that I impressed you with my poetry the first time we met and you have given me opportunity after opportunity since then ;)

Tahereh, you were my lifeline throughout this whole project, it would not have been completed if not for your assistance, both in the lab and as a friend. Thank you so much, and don't worry, now that the thesis is submitted I'll get back to being an RA now ;)

Adrian, you drove this project with me, and it was a super fun collaboration combining our very different scientific skill sets! Thanks for all your help and I'm looking forward to our next scientific collaborations now that you are here with us in Melbourne!

Sandra and Annette, thanks for all the perforin! It's a huge task you guys do, providing perforin and other proteins for the masses, and none of this work would have been possible without you both.

Bart, thanks for your guidance with the project from a far (and for your kindness in having me visit your laboratory in London, not once, but twice!), and looking forward to further collaborations ☺

Nachos, thank you for all your help over the last few years, I think having a fellow Nacho in the lab has helped me find my inner Nachito. Nachos.

Alejandro, Amy and Aji, you guys all get a A.A.A. rating as well! ...get it? ;)

To everybody else in Trapani, Voskoboinik and Oliaro laboratories, thank you!

Finally, to my Mum, Dad, Cassie and Tim, thanks for all your support not just over the last 4 years, but always! I'm super lucky to have such a great family to look after me...and deliver me home made food every other weekend! ☺

In particular though, a big shout out has to go the freshly cooked pasta Tim would serve me when I arrived home after late nights on the microscope ...I don't think I could have done this without all those carbs!



# Table of Contents:

Title Page .....	1
Preface .....	2
Abstract .....	3
Acknowledgements .....	4
Table of Contents .....	5
List of Figures .....	8
List of Abbreviations .....	10
<b>Chapter 1 Literature review and introduction .....</b>	<b>13</b>
1.1 Cytotoxic Lymphocytes .....	13
1.1.1 Immune system overview .....	13
1.1.2 Cytotoxic lymphocytes role in the immune system.....	14
1.1.3 Mechanisms of Killing.....	14
1.2 Perforin .....	16
1.2.1 Structure and function .....	16
1.2.2 Perforinopathy: The role of disrupted perforin function .....	18
1.2.3 Self-Protection of cytotoxic lymphocytes from perforin .....	19
1.2.3.1 Inside the cell .....	19
1.2.3.2 Following secretion by exocytosis .....	20
<b>Chapter 2 General Materials and Methods .....</b>	<b>21</b>
2.1 Molecular cloning and recombinant protein expression of Perforin constructs .....	21
2.1.1 Molecular cloning.....	21
2.1.2 Recombinant Perforin expression and purification .....	21
2.2 Cell Preparation and culture .....	22
2.2.1 Cell culture .....	22
2.2.2 Primary mouse OTI cells .....	22
2.2.3 Primary mouse natural killer cells .....	22
2.3 Cell transduction .....	23
2.3.1 Transduction of murine and human cell lines .....	23
2.3.2 Transduction of naive OTI CTL.....	23
2.4 Cytotoxicity Assays.....	24

2.4.1	<sup>51</sup> Cr release assay .....	24
2.4.2	Flow cytometry-based cytotoxicity assay.....	24
2.5	Atomic Force Microscopy (Experiments designed and performed by Dr Adrian Hodel) .....	25
2.5.1	Lipid vesicle and AFM sample preparation.....	25
2.5.2	AFM imaging and data processing.....	25
<b>Chapter 3</b>	<b>Cytotoxic lymphocytes are resistant to perforin binding and lysis.....</b>	<b>27</b>
3.1	Introduction .....	27
3.2	Materials and Methods.....	29
3.2.1	Cloning of LAMP-1 constructs .....	29
3.2.2	Transduction of LAMP-1 constructs .....	29
3.2.3	Flow Cytometry.....	29
3.2.3.1	Fluorescence activated cell sorting for equal protein expression .....	29
3.2.3.2	Surface staining.....	30
3.2.4	Recombinant perforin cytotoxicity assays.....	30
3.2.5	CTL cytotoxicity assay.....	30
3.2.6	Validation of TMH1-GFP-PRF.....	30
3.2.7	TMH1-GFP-PRF binding assay.....	31
3.3	Results.....	32
3.3.1	Does cell surface LAMP-1 protect cells against perforin? .....	32
3.3.2	Primary protection; primary cytotoxic lymphocytes are less sensitive to recombinant perforin lysis when compared to common cell lines.....	38
3.3.3	Differential perforin binding to CTLs and target cells.....	41
3.4	Discussion .....	43
<b>Chapter 4</b>	<b>High lipid order protects the plasma membrane from perforin binding.....</b>	<b>45</b>
4.1	Introduction .....	45
4.1.1	Lipids in Cellular Membranes .....	45
4.1.2	Cholesterol and membrane order .....	48
4.1.3	Modification of membrane order using 7-Ketocholesterol (7KC).....	49
4.1.4	Laurdan as a probe of membrane order .....	50
4.2	Materials and Methods.....	52
4.2.1	AFM.....	52
4.2.2	7KC loading.....	52
4.2.3	Osmosis Assay .....	52
4.2.4	Laurdan Microscopy .....	52

4.3	Results.....	54
4.3.1	Lipid bilayer regions containing high levels of sphingomyelin and cholesterol are refractory to perforin binding and pore formation .....	54
4.3.2	Anarchy via 7KC: treatment of CTLs with 7KC results in disordered plasma membrane 57	
4.3.3	A weakened shield: reduced plasma membrane order increases the sensitivity of CTLs to perforin.....	60
4.3.4	A conserved role of membrane order in perforin resistance for both the innate and adaptive immune system .....	62
4.4	Discussion .....	63
<b>Chapter 5</b>	<b>Phosphatidylserine inactivates membrane-bound perforin .....</b>	<b>64</b>
5.1	Introduction .....	64
5.2	Materials and Methods .....	65
5.2.1	Indo-1AM calcium flux measurements conducted by time-lapse flow cytometry .....	65
5.2.2	Ca <sup>2+</sup> dependence of the plasma-membrane bound perforin.....	65
5.2.3	Atomic Force Microscopy .....	65
5.2.4	Generation of stably expressing tubulin-Cherry <i>Prf1</i> <sup>-/-</sup> OTI CTLs .....	65
5.2.5	Fixed cell Confocal Microscopy .....	65
5.2.5.1	Sample preparation.....	65
5.2.5.2	Imaging.....	66
5.2.5.3	Co-localisation analysis .....	66
5.2.6	Live cell Confocal Microscopy .....	67
5.2.6.1	Recombinant perforin addition to a mixture of EL4 and CTLs .....	67
5.2.6.2	Visualizing phosphatidylserine (PS) exposure at the immunological synapse .....	67
5.3	Results.....	68
5.3.1	Perforin association with CTLs: Binding without pore formation .....	68
5.3.2	EGTA resistance of WT-GFP-PRF bound to CTLs; attachment without insertion? .....	70
5.3.3	EGTA resistance of perforin clusters formed on Phosphatidylserine rich lipid bilayers 72	
5.3.4	Phosphatidylserine - a marker of the dead that protects the living. ....	74
5.3.5	Phosphatidylserine is exposed on the CTL membrane during synapse formation .....	77
5.4	Discussion .....	78
<b>Chapter 6</b>	<b>Conclusion and Future Directions .....</b>	<b>80</b>
6.1	“Lipid Order and Charge Protect Killer T cells from Accidental Death” .....	80
6.2	Future Directions .....	83

## List of Figures:

Figure 1.1: Basic overview of immune system components. ....	13
Figure 1.2: Schematic diagram of the granule exocytosis pathway .....	15
Figure 1.3: Overview of Perforin Structure .....	16
Figure 1.4: Comparison of complete vs incomplete pore and frequency of such pores in membranes. ....	17
Figure 1.5: The basis for pathology of FHL.....	18
Figure 2.1: Vector cloning map showing details of TMH1-GFP-PRF cloning.....	21
Figure 2.2: Schematic diagram of planar lipid bilayer creation. ....	25
Figure 2.3: Schematic representation of an Atomic Force Microscope.....	26
Figure 2.4: Atomic Force Microscopy provides a topographical map of the sample surface.....	26
Figure 3.1: Schematic diagram of the LAMP-1 protein highlighting lysosomal targeting motif. .	28
Figure 3.2: Vector map showing details of $\Delta$ c-LAMP-1 MSCV-IRES-GFP cloning. ....	29
Figure 3.3: Analysis of plasmid expression levels of transduced Jurkat, EL4 and OTI CTL.....	30
Figure 3.4: Analysis of surface LAMP-1 levels in cell lines transduced with MSCV-GFP or $\Delta$ c-LAMP-1-MSCV-GFP.....	32
Figure 3.5: High surface levels of LAMP-1 do not protect common target cell lines from perforin lysis.....	33
Figure 3.6: High surface levels of LAMP-1 do not protect common target cell lines from cytotoxic lymphocyte killing .....	34
Figure 3.7: Analysis of surface LAMP-1 levels and killing efficiency of WT OTI CTLs transduced with MSCV-IRES-GFP or $\Delta$ c-LAMP-1 MSCV-IRES-GFP.....	35
Figure 3.8: Analysis of surface LAMP-1 levels in Prf1 <sup>-/-</sup> OTI CTLs transduced with MSCV-IRES-GFP or $\Delta$ c-LAMP-1 MSCV-IRES-GFP.....	36
Figure 3.9: High surface levels of LAMP-1 do not protect Prf1 <sup>-/-</sup> OTI CTLs from recombinant perforin lysis or killing by WT OTI CTLs. ....	37
Figure 3.10: “Cytotoxic lymphocytes are resistant to perforin lysis. ....	38
Figure 3.11: “Functionality of TMH1-GFP-PRF as assessed by <sup>51</sup> Cr release assay. ....	40
Figure 3.12: “Binding of TMH1-GFP-PRF to a 1:1 mixture of CTLs and EL4 cells, as assessed by flow cytometry.” .....	42
Figure 4.1: Basic structure of the phospholipid bilayer.....	45
Figure 4.2: Structural comparison of the three main components of cellular membranes; glycerophospholipids, sterols and sphingolipids.....	47
Figure 4.3: Schematic diagram showing the difference in lipid packing between liquid disordered and liquid ordered membrane phases. ....	48
Figure 4.4: Incorporation of 7KC into plasma membranes increases spacing between lipids.....	49
Figure 4.5: Laurdan excitation/emission spectrum. ....	50
Figure 4.6: Schematic diagram detailing the collection of a lambda stack using laurdan. ....	51
Figure 4.7: “Lipid order protects synthetic membranes from perforin pore formation.....	55
Figure 4.8: “Prepore-locked TMH1-PRF binds to disordered domains on phase separated lipid membranes. ....	56
Figure 4.9: “Determination of a non-cytotoxic concentration of sterol/ M $\beta$ CD. ....	57
Figure 4.10: “7KC treatment of CTLs does not sensitise cells to osmotic stress. ....	58
Figure 4.11: Representative example of object and plasma membrane segmentation using the MATLAB extension ‘Spectral Imaging Toolbox’ (Aron et al., 2017).....	59

Figure 4.12: “Generalised Polarisation (GP) values of CTL decrease following the incorporation of increasing ratios of 7KC:cholesterol.....	59
Figure 4.13: “Reduced membrane order of 7KC-treated CTLs sensitises the cells to TMH1-GFP-PRF binding. ....	60
Figure 4.14: “Reduced membrane order of 7KC-treated CTLs and EL4s sensitises the cells to WT-PRF lysis. ....	61
Figure 4.15: “Reduced membrane order of 7KC-treated murine NK cells sensitizes the cells to WT-PRF lysis. ....	62
Figure 5.1: “Similar levels of perforin bound to EL4 and CTLs. ....	68
Figure 5.2: “A similar response to Ionomycin treatment is observed for both EL4 and CTLs.....	69
Figure 5.3: “Ca <sup>2+</sup> influx into Indo-1 AM labelled CTLs and EL4 cells upon exposure to sublytic amounts of WT-GFP-PRF. ....	70
Figure 5.4: “Flow cytometry on WT-GFP-PRF and TMH1-GFP-PRF binding to EL4 (CD8 <sup>-</sup> ) and CTLs. ....	71
Figure 5.5: “Perforin forms non-porating clusters on phosphatidylserine membranes. ....	73
Figure 5.6: Perforin binding to phosphatidylserine on the CTL plasma membrane.....	74
Figure 5.7: “Time-lapse microscopy highlights different response of CTL’s and EL4 to addition of WT-GFP PRF. (Supplementary Video 1).....	75
Figure 5.8: “Unlike target cells, CTLs maintain healthy morphological appearance and mobility one hour after addition of WT-GFP-PRF. ....	76
Figure 5.9: “Time-lapse confocal microscopy confirms PS exposure on pre-synaptic membrane upon synapse formation. ....	77
Figure 6.1: “Mechanism of cytotoxic lymphocyte protection from secreted perforin. ....	82

## List of Abbreviations:

<sup>51</sup> Cr	Sodium chromate
7KC	7 keto Cholesterol
AFM	Atomic Force Microscopy
APC	allophycocyanin
APC	Antigen Presenting Cell
BSA	Bovine Serum Albumin
CaCl <sub>2</sub>	Calcium Chloride
CAR	Chimeric Antigen Receptor
CD	Cluster of Differentiation
CDC	Cholesterol Dependent Cytolysins
cDNA	Complementary DNA
Chol	Cholesterol
CO <sub>2</sub>	Carbon Dioxide
CRISPR	Clustered Regularly Interspaced Short Palindromic Repeats
CTL	Cytotoxic T Lymphocyte, CD8 <sup>+</sup> T cells, antigen specific killer T cells
CTV	Cell Trace Violet
CTxB	Cholera Toxin Subunit B
DIC	Differential Interference Contrast
DMEM	Dulbecco's Modified Eagle Medium
DNA	Deoxyribonucleic nucleic Acid
DOPC	Dioleoylphosphatidylcholine
DOPS	Dioleoylphosphatidylserine
DTT	Dithiothreitol
EDTA	Ethylenediaminetetraacetic acid
EGF	Epidermal Growth Factor

EGTA	ethylene glycol-bis( $\beta$ -aminoethyl ether)-N,N,N',N'-tetraacetic acid
ER	Endoplasmic Reticulum
FCS	Fetal Calf Serum
FHL	Familial Hemophagocytic Lymphohistiocytosis
FIJI	FIJI Is Just ImageJ
GA	Glutaraldehyde
GFP	Green Fluorescent protein
GM1	Ganglioside Monosialotetrahexosylganglioside 1
GP	Generalized Polarization
HBSS	Hanks Balanced Salt Solution
HEK (293T)	Human Embryonic Kidney 293T cells
HEPES	4-(2-hydroxyethyl)-1-piperazineethanesulfonic acid
HER2	Human Epidermal Growth Factor receptor 2
IL-2	Interleukin-2
IRES	Internal Ribosome Entry site
LAMP-1/CD107a	Lysosomal Associated Membrane Protein-1/Cluster of Differentiation 107a
LLS	Lattice Light Sheet microscopy
MACPF	Membrane Attack Complex and PerForin proteins
MACS	Magnetic-Activated Cell Sorting
MBCD	Methyl $\beta$ -cyclodextran
MFI	Mean Fluorescence Intensity
MgCl <sub>2</sub>	Magnesium Chloride
MHC	Major Histocompatibility Complex
MSCV	Murine Stem Cell Virus
MTOC	Microtubule Organising Centre
NaCl	Sodium Chloride

NK	Natural Killer Cell
PBS	Phosphate Buffered Saline
PC	Phosphatidylcholine
PD-1	Programed cell death-1
PE	Phosphatidylethanolamine
PE	Phycoerythrin
PI	Propidium Iodide
<i>Prf1<sup>-/-</sup></i>	Perforin knock out
PS	Phosphatidylserine
RPMI	Roswell Park Memorial Institute medium
s.e.m.	Standard Error of the Mean
SapC	Sapoin C
SD	Standard Deviation
SM	Sphingomyelin
TEM	Transmission Electron Microscopy
TMH1	Trans Membrane Helix 1
WT	Wild Type



# Chapter 1 Literature review and introduction

## 1.1 Cytotoxic Lymphocytes

### 1.1.1 Immune system overview

Humans and other mammals rely on their immune system to survive exogenous biological threats, such as bacteria and viruses (Dempsey et al., 2003). Without an immune system, we would rapidly succumb to these infections. The complexity of the immune system is enormous, with two main branches (innate and adaptive) immunity working together to provide a comprehensive defence system (Paul, 2011). The innate immune system is made up of cells which are constitutively ready to perform their task, whereas cell types which make up the adaptive immune system require a period of time to generate a response which is specific to the particular threat, and also have the ability to acquire memory of a particular pathogen, reducing the lag time between infection and adaptive immune response for future infections of the same pathogen (Chaplin, 2010; Parkin & Cohen, 2001). The way that various cells in these two arms of the immune system function varies greatly, ranging from epithelial cells, which form the first layer of defence against pathogens by providing a physical barrier, to antigen specific killer T cells (CD8<sup>+</sup> T cells, CTLs), which are able to specifically recognize and destroy cells infected with a particular pathogen. A brief overview of the main cell types that make up both the innate and adaptive arms of the immune system is provided below (Fig. 1.1). Although not an exhaustive list, this provides context to the position that cytotoxic lymphocytes occupy in our body's immune system. This thesis will concentrate on CTLs and Natural Killer (NK) cells, collectively referred to as cytotoxic lymphocytes, which are explained in more detail below.

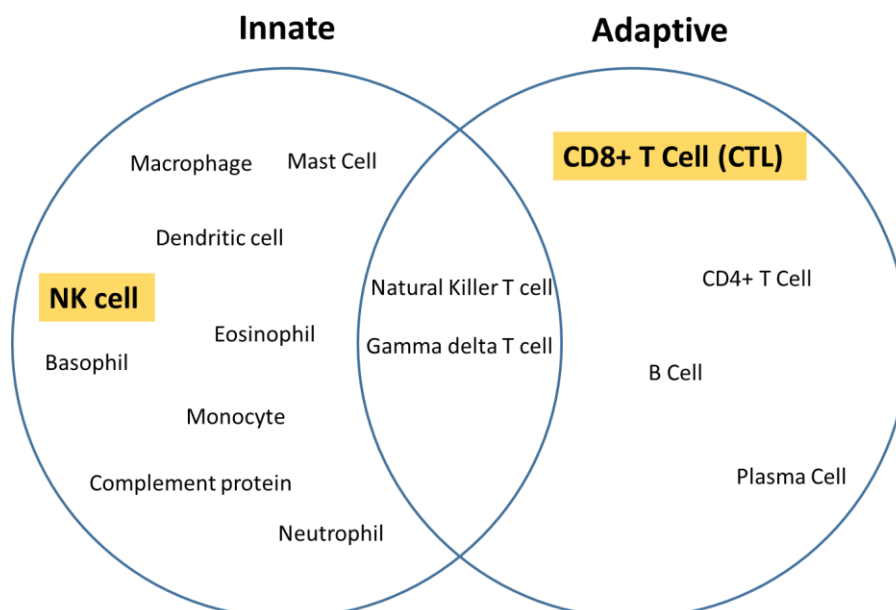


**Figure 1.1: Basic overview of immune system components.**

NK cells are the cytotoxic lymphocytes of the innate immune system, whereas CD8<sup>+</sup> T cells (CTL) form part of the adaptive immune system. Image adapted from (Dranoff, 2004)

### 1.1.2 Cytotoxic lymphocytes role in the immune system

Cytotoxic lymphocytes, represented by CTLs and NK cells, play a key role in defence against intracellular pathogens (viruses and some bacteria) and transformed cells (Voskoboinik et al., 2006). NK cells provide the frontline of defence, attacking infected or transformed cells that are not recognized as self (Ljunggren & Kärre, 1990). More recent studies have shown that NK cells operate within a complex regulation system, maintaining sufficient responsiveness to thwart infections, but a less primed state as well to avoid autoimmunity (Shifrin et al., 2014). As opposed to the inherent killing capacity of NK cells, CTLs acquire their ability to recognize and kill targets only after an initial briefing by Antigen Presenting Cells (APC). APCs present foreign antigens to naïve CTLs via MHC class 1 molecules (Germain, 1994). After this initial interaction within the secondary lymphoid organs, CTLs specific for the presented antigen proliferate (Kaech et al., 2002) and then enter the site of infection (Weninger et al., 2002). This secondary 'wave' of antigen specific CTLs then clears the remaining infection. In this way, both the innate and adaptive arms of the immune system function together to provide a highly effective means of defence against infection.

### 1.1.3 Mechanisms of Killing

On engaging with target cells, both forms of cytotoxic lymphocyte have two primary modes of attack (Lowin et al., 1994). The first mode of attack is the granule exocytosis pathway (*Figure 1.2*), which involves the formation of a synapse with the target and consequent release of a toxic payload of the pore-forming perforin and pro-apoptotic serine proteases granzymes (Lopez et al., 2012; Trapani & Smyth, 2002). This mechanism leads to rapid target cell death through granzyme-induced apoptosis or, in some rare instances, direct lysis by perforin. The second is the Fas ligand pathway, a relatively slow mechanism that leads to target cell apoptosis. This pathway involves the upregulation of Fas ligand on the cytotoxic lymphocyte upon engagement with a target cell (Lynch et al., 1995). Fas ligand on the cytotoxic lymphocyte trimerizes Fas receptors on the target cell, leading to activation of Caspase 8 and subsequent downstream events resulting in apoptosis (Waring & Müllbacher, 1999).

Within the cytotoxic lymphocyte, perforin and granzymes are stored inside secretory granules, which upon synapse formation migrate via microtubules towards the polarized microtubule organising complex (MTOC) at the presynaptic membrane (Geiger et al., 1982; Kupfer & Dennert, 1984). The secretory granules are then delivered to the synapse area via direct centrosome contact (Stinchcombe et al., 2006). Once within the synapse, perforin forms transient pores on the target cell membrane, which allow granzymes to diffuse into the target cell and initiate apoptosis (Lopez, Susanto, et al., 2013). Numerous granzymes are present in the secretory granules (Chowdhury & Lieberman, 2008), however granzyme B is the most cytotoxic. Once within the target cell cytoplasm, both mouse and human granzyme B activate caspases to initiate cell death of the target cell. Whilst mouse granzyme B cleaves caspase-3 directly, human homologue acts primarily by cleaving Bid that activates Bak/Bax leading to disruption of the mitochondria (Cullen et al., 2007).

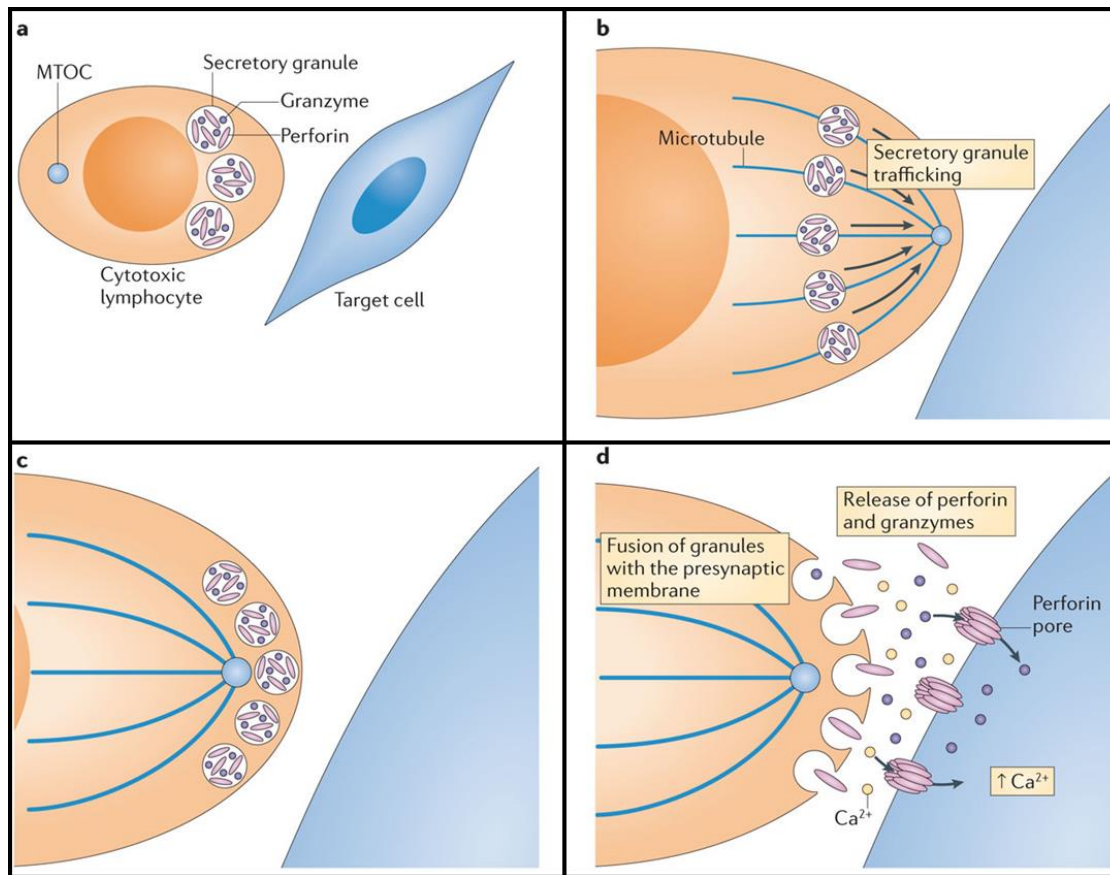


**Figure 1.2: Schematic diagram of the granule exocytosis pathway**

- a.) Cytotoxic lymphocyte approaches target cell
- b) Secretory granules move towards the cytotoxic lymphocyte MTOC which has polarized at synapse
- c) Secretory granules are polarized at the point of synapse formation prior to degranulation
- d) Secretory granules fuse into the immune synapse following cytotoxic lymphocyte calcium flux, allowing the release of perforin to form pores on the target cell membrane. Granzymes are shown entering the cytosol of the target cell to initiate apoptosis. *Image adapted from (Voskoboinik et al., 2015)*

## 1.2 Perforin

### 1.2.1 Structure and function

Perforin is a 67kDa monomeric protein containing 3 main structural domains: a Membrane Attack Complex and PerForin proteins (MACPF) domain which is a “warhead” involved in membrane insertion and pore formation, an Epidermal Growth Factor (EGF) like domain ‘shelf region’ and a C-terminal domain containing a calcium-dependent membrane binding C2 domain (Figure 1.3a). The X-ray crystal structure of monomeric murine perforin (Figure 1.3b) as well as a full reconstruction of a perforin pore obtained via cryo-electron microscopy (Figure 1.3c) were reported in 2010 (Law et al., 2010) and this has allowed for a much better understanding of both the differences and similarities that perforin possesses with Cholesterol Dependent Cytolysins (CDCs) and MACPFs. The MACPF and CDCs are part of a superfamily of immune effector proteins that undergo a conformational change involving a transition from two clusters of  $\alpha$ -helices to transmembrane  $\beta$ -hairpins (Lukoyanova et al., 2016). These transformations do not require any partner/accessory proteins.

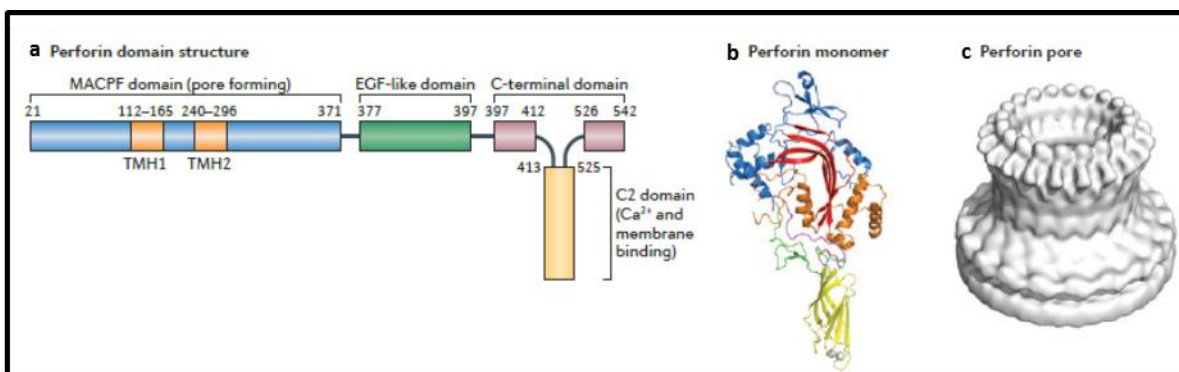


**Figure 1.3: Overview of Perforin Structure**

- a.) Domain structure of perforin highlighting the MACPF domain, EGF like domain and C-terminal domain (including the C2 domain).
- b.) Crystal structure of a perforin monomer
- c.) Cryo-electron microscopy reconstruction of a perforin pore assembly. *Image adapted from (Voskoboinik et al., 2015)*

The first essential step in pore formation is the  $\text{Ca}^{2+}$ -dependent membrane binding of perforin through the C2 domain (Traore et al., 2013; Voskoboinik et al., 2005; Yagi et al., 2015). The C2 domain of perforin requires much higher  $\text{Ca}^{2+}$  concentrations than other known C2 domains to enable its membrane binding (Voskoboinik et al., 2005). As all other known C2 domains act inside cells, this is believed to be one of the critical factors that restrict perforin action to the extracellular milieu, where the neutral pH and high free calcium concentration (1.3mM) are favourable for perforin binding and pore formation. Four or five calcium ions bind to the C2 domain, and it is hypothesized that the weakest affinity binding site is the final trigger to induce an essential conformational change enabling perforin membrane binding. Thus, following  $\text{Ca}^{2+}$  binding to the C2 domain, two loops 'swing' so four hydrophobic residues face the membrane and anchor PRF. Subsequently, perforin oligomerizes forming prepores, followed by unfurling of two transmembrane helix regions within the MACPF domain, tight packing of the prepore leading to insertion and pore formation. It has recently been discovered that when perforin monomers bind to a lipid membrane they form small arcs which then act as "nucleation" sites to create full pores (Leung et al., 2017). Within this same study it was also shown that both arcs and pores have the ability to disrupt membranes (Figure 1.4).

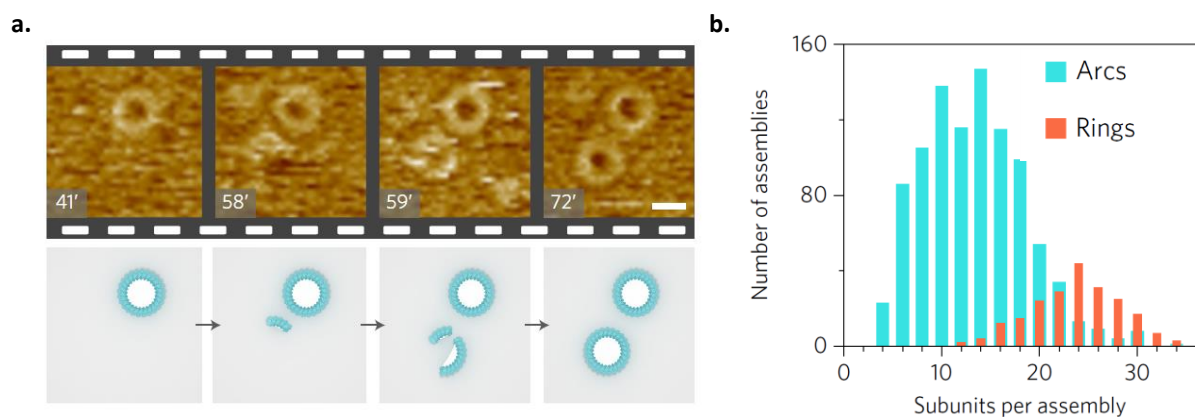


**Figure 1.4: Comparison of complete vs incomplete pore and frequency of such pores in membranes.**

**a.)** Atomic Force Microscopy images (top) and graphical representations (bottom) of a stable pore (seen top right) and arc (bottom centre) which grows into a full pore over time via recruitment of other prepore oligomers. Note the ability of the arc to pierce the membrane before reaching a full pore shape.

**b.)** A comparison of the frequency of arcs being formed compared to full pores, and detail of how many subunits are present per assembly. *Image adapted from (Leung et al., 2017).*

### 1.2.2 Perforinopathy: The role of disrupted perforin function in disease

Given the crucial role of perforin in cytotoxic lymphocytes killing mechanism, it is not surprising that deficiencies in perforin can lead to a breakdown of the immune surveillance. Familial Hemophagocytic Lymphohistiocytosis (FHL) is a syndrome, which occurs when a patient cannot successfully clear antigen-presenting target cells. Although there is only one form of FHL that involves mutations in perforin itself (FHL2) (Stepp et al., 1999), these cases make up ~50% of all cases (Voskoboinik & Trapani, 2013). The other forms of FHL are caused by mutations in genes which are involved in the release of perforin into the immune synapse (MUNC13-4, STX11 and STXBP2 mutations result in FHL3-5, respectively) (Côte et al., 2009; Feldmann et al., 2003; zur Stadt et al., 2005), hence their disruption also leads to a lack of perforin delivery into the synapse and killing target cells. A fifth form, FHL1, has been localized to chromosome 9q21.3-22 (Ohadi et al., 1999) but no specific genetic mutation has been identified.

Failure of cytotoxic lymphocytes to clear antigen-presenting target cells results in excessive activation of CTLs which produce large amounts of interferon gamma (Henter et al., 1991). Excessive release of interferon gamma and other inflammatory cytokines following failed target cell death was recently shown to be a consequence of failed detachment of the killer cell from its target, which in turn results in repetitive calcium signalling in the CTL/NK cell and deviation from secreting cytotoxic molecules to stored cytokines (Jenkins et al., 2015). The excessive interferon gamma in turn activates macrophages which then produce large amounts of inflammatory cytokines, including IL-6, TNF and IL-18, which cause a destructive 'cytokine storm' in the patient (Figure 1.5), leading to many clinical symptoms including fever, pancytopenia, neuroinflammation and multi-organ failure; if left untreated, FHL is almost invariably fatal. Cases of FHL in which both inherited alleles of perforin are 'null' has a median age of onset of less than 12 months, and bone marrow transplantation remains the only curative treatment.

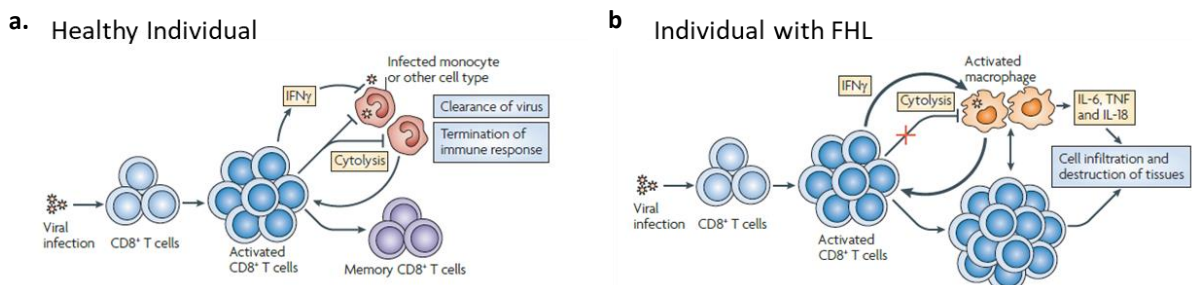


**Figure 1.5: The basis for pathology of FHL.**

- a.) In a healthy individual the immune response is terminated following cytolysis of antigen presenting cells.
- b.) In an individual with FHL, the failure of the Cytotoxic Lymphocytes to remove antigen presenting cells results in continual IFN $\gamma$  release, leading to overproduction of IL-6, TNF and IL-18 by macrophages (termed cytokine storm) which leads to damage of surrounding cells. *Image adapted from (de Saint Basile et al., 2010)*

This complete loss of perforin activity is the most extreme example of a class of perforin related pathologies, recently termed 'perforinopathy' (Voskoboinik & Trapani, 2013). Unlike the early onset of disease (in infants) due to a complete loss of perforin function, partial perforin deficiency leads to disease presentation later in life, in adolescence or even in adulthood. Reports have been presented that link partial defects in perforin function, mostly due to protein misfolding, with a loss of virus or tumour immune surveillance. For example, patients with that kind of mutations may be susceptible to blood (Chia et al., 2009) and other forms (Chaudhry et al., 2016; Trapani et al., 2013) of cancer. Overall, perforinopathy is a wide spectrum of pathological manifestations that have been classified as acute, sub-acute and chronic, depending on the age of patients and severity of the disease. Acute disease presentation is caused by a complete loss of perforin and an inability to remove antigen presenting cells resulting in severe cytokine storm at a very young age. Sub-acute and chronic FHL (which occur later in life) are caused increasingly by the failure of partially functional cytotoxic lymphocytes to eradicate transformed and malignant cells, which allows these cells to proliferate and cause pathology (Voskoboinik & Trapani, 2013).

### **1.2.3 Self-Protection of cytotoxic lymphocytes from perforin**

#### **1.2.3.1 Inside the cell**

Numerous factors have been shown to protect cytotoxic lymphocytes from their own perforin whilst it is stored within the cell. After its synthesis in the endoplasmic reticulum (ER), perforin is transported to the trans-Golgi network. A rapid transport out of the ER that keeps the steady state concentration of perforin extremely low is crucial as conditions within the ER are optimal for perforin function, with high calcium concentrations and neutral pH. Specifically-designed perforin mutants which dwell for too long in the ER are toxic to the host cell, as it most likely oligomerises and forms pores. The rapid export of perforin from the ER has been shown to be crucially dependent on the invariantly conserved hydrophobic residues of the carboxy-terminal region, specifically Trp555 (Brennan et al., 2011).

More recently, a second mechanism of protection has been identified, involving N-linked glycosylation at the carboxy-terminus of perforin. N-glycosylation at Asn549 was found to create steric hindrance of perforin monomers, thus inhibiting oligomerisation and preventing premature perforin pore formation within the host cell (House et al., 2017). Once perforin has been transported to the safe environment of the cytotoxic granules, its cytotoxic function is completely inhibited by low pH, and this glycan is then removed by proteolytic cleavage of the last twelve C-terminal residues. This cleaved fully-functional form of perforin is then released into the immune synapse, where neutral pH and high calcium levels are permissible for pore formation on the target cell.

### **1.2.3.2 Following secretion by exocytosis**

What makes cytotoxic lymphocytes such an effective defence system is their ability to kill numerous targets sequentially without being negatively affected by their own toxins. After initially being identified via bulk cell assays (Berke et al., 1972), this 'serial killing' phenomenon has been observed visually both in early studies (Rothstein et al., 1978) and also in more recent studies with advanced forms of time-lapse microscopy (Halle et al., 2016; Lopez, Jenkins, et al., 2013). The ability of one CTL/NK to kill many successive targets necessitates cytotoxic lymphocyte self-protection, so that a cytotoxic lymphocyte that forms a synapse with a target cell/s is not killed by the release of their own toxic cargo of perforin and granzymes. This is despite the fact that with neutral pH and high calcium concentration the conditions within the synapse are favourable for perforin function (Praper et al., 2010; Young et al., 1987) and both the post-synaptic and pre-synaptic membrane are equally exposed to perforin and granzymes. Time lapse microscopy has shown a lack of perforin pore formation on the cytotoxic lymphocyte (Lopez, Jenkins, et al., 2013), bringing back to life an old (Golstein, 1974) and unresolved fascinating question of how cytotoxic lymphocytes are protected from their own perforin. This has remained one of the most intriguing unanswered questions in the field of cytotoxic lymphocyte biology, and the current thesis is aimed at resolving this mystery.



## Chapter 2 General Materials and Methods

### 2.1 Molecular cloning and recombinant protein expression of Perforin constructs

#### 2.1.1 Molecular cloning

The previously described TMH1-PRF mutant (Leung et al., 2017) provides a non-lytic form of perforin. Mutations replacing alanine and tryptophan residues at amino acid position 144 and 373, respectively, with cysteine residues results in the formation of a new, reversible disulphide bridge that tethers TMH1 to the much larger MACPF domain. The mutations do not affect calcium dependent membrane binding, however, as the TMH1 region is locked in this manner, it is unable to unfurl and insert into the membrane. By unlocking the disulphide bond, using the reducing agent DTT, the activity of the perforin can be restored (Leung et al., 2017). For my experiments in this thesis, a GFP fusion protein of TMH1-PRF was created, as describe below.

TMH1-GFP-Perforin fusion protein cDNA was cloned into the multiple cloning site of pFastBac<sup>TM</sup>1 expression vector using the restriction enzymes EcoR1 and Xho1 (Figure 2.1).

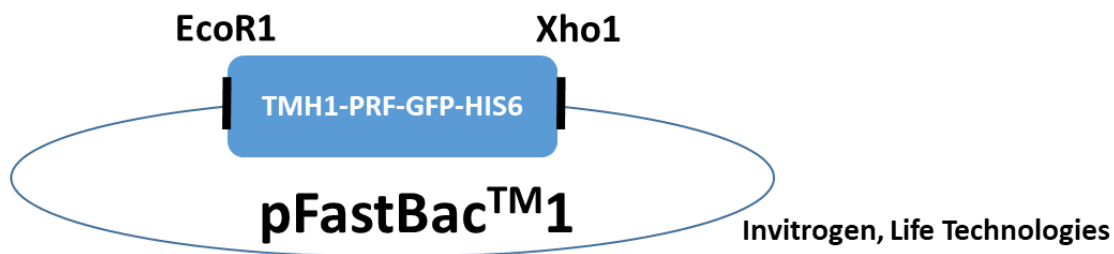


**Figure 2.1: Vector cloning map showing details of TMH1-GFP-PRF cloning.**

TMH1-GFP-PRF was cloned into pFastBac<sup>TM</sup>1 bacula expression vector within the multiple cloning site, using EcoR1 and Xho1.

#### 2.1.2 Recombinant Perforin expression and purification

*All recombinant perforin purification was performed by Ms Annette Ciccone and Ms Sandra Verschoor. WT-PRF and WT-GFP-PRF were both cloned and purified prior to the beginning of my project, and are first published in (Voskoboinik et al., 2004) and (Lopez, Susanto, et al., 2013) respectively. TMH1-PRF, which provides the basis for our TMH1-GFP-PRF construct, was cloned and purified previously and is published in (Leung et al., 2017).*

Wild-type perforin (WT-PRF), perforin-GFP fusion protein (WT-GFP-PRF), and the GFP fusion protein of TMH1-PRF (TMH1-GFP-PRF) were expressed and purified using baculovirus expression system as described previously ((Leung et al., 2017; Lopez, Susanto, et al., 2013).

## **2.2 Cell Preparation and culture**

### **2.2.1 Cell culture**

Murine cell lines EL4, P815 and MC57 were maintained in SAFC DMEM (Sigma-Aldrich, Missouri, USA) media supplemented with 10% FCS (Gibco, Loughborough, UK), 15mM HEPES (Merck, Missouri, USA), 44mM NaHCO<sub>3</sub> (Merck, Missouri, USA) and 2 mM Glutamax (GIBCO, Loughborough, UK) at 37°C in 10% CO<sub>2</sub>.

### **2.2.2 Primary mouse OTI cells**

Primary murine CD8<sup>+</sup> T cells (cytotoxic T lymphocytes, CTL) were generated from BL/6 OTI transgenic mice, and maintained as described previously (Sutton et al., 2016). Briefly, mice were sacrificed using CO<sub>2</sub> euthanasia or cervical dislocation; spleens were harvested and mashed through a 70µm filter to create a single cell suspension before ¼ of these cells were stimulated with 10nM SIINFEKL, 100U/ml recombinant human IL-2 in 100ml CTL media comprised of RPMI 1640 supplemented with 10% Foetal Calf Serum (FCS), 2mM Glutamax (GIBCO, Loughborough, UK), 50 U/ml Penicillin, 50µg/ml Streptomycin, 1mM Sodium Pyruvate and 50µM 2-mercaptoethanol. After 3 days of stimulation, remaining SIINFEKL was washed from the culture (by three washes in PBS (Ca/Mg-free)) and cells resuspended in fresh CTL media containing 100U/ml IL-2 (Media was changed and IL-2 supplemented daily). CTLs were maintained at <10<sup>6</sup> cells/mL, and used on days 4-8.

### **2.2.3 Primary mouse natural killer cells**

BL/6 mice were sacrificed using CO<sub>2</sub> euthanasia or cervical dislocation; spleens were harvested and a single cell suspension created by mashing the spleen through a 70 µm nylon filter and resuspending them in 10ml complete NK media comprised of RPMI 1640 supplemented with 10% FCS, 2mM Glutamax (GIBCO, Loughborough, UK), 50 U/ml Penicillin, 50µg/ml Streptomycin, 100µM nonessential amino acids, 4-(2-hydroxyethyl)-1-piperazineethanesulfonic acid (HEPES) and 50µM 2-mercaptoethanol. This single cell suspension was then pelleted by centrifugation at 460xg for 4 minutes and resuspended in a Magnetic-Activated Cell Sorting (MACS) buffer consisting of 2% FCS, 1mM EDTA in PBS (Ca/Mg-free). NK cells were isolated using Stem Cell EasySep™ Mouse NK Cell Isolation Kit, and isolated NK cells were cultured at 750,000 cells/ml in complete NK media supplemented with 1000 U/ml IL-2. On Day 5, cells were split back to 750,000 cells/ml and supplemented with fresh IL-2. These isolated NK cells were used on Day 6 and Day 7.

## **2.3 Cell transduction**

### **2.3.1 Transduction of murine and human cell lines**

HEK293T cells were plated at a density of  $2 \times 10^5$  cells/ml on Day 0 in tissue culture treated plates and transfected on Day 1 with the DNA constructs of interest and amphotropic packaging vector using the calcium phosphate method (Schenborn & Goiffon, 2000). Although they are murine cells, EL4 were found to transduce with higher efficiency using amphotropic packaging vector instead of the murine specific pCL Eco. On Day 2 media was changed on the HEK293T cells and RetroNectin was plated onto non-tissue culture treated plates in preparation for transduction of cell lines on Day 3. On Day 3, RetroNectin plates were washed twice with PBS (Ca/Mg-free) and viral supernatant was harvested from the HEK293T cells and transferred to the RetroNectin plates. Viral supernatant was then centrifuged at 2000xg for 1 hour to bring the viral supernatant and RetroNectin into close contact. Cells were then added to these wells and centrifuged at 460xg for 4 minutes to bring the cells into close contact with the RetroNectin/viral particles on the bottom of the plate. On Day 4, the transduced cells were removed from the plate, resuspended in fresh media and returned to culture conditions.

### **2.3.2 Transduction of naive OTI CTL**

HEK293T cells were plated at a density of  $2 \times 10^5$  cells/ml on Day -3 (relative to CTL isolation on Day 0) in tissue culture treated plates and transfected on Day -2 with the DNA constructs of interest and pCIEco packaging vectors using the calcium phosphate method (Schenborn & Goiffon, 2000). On Day -1, media was changed on the HEK293T cells, and RetroNectin was plated onto non-tissue culture treated plates in preparation for transduction of naïve CTL on Day 0. On Day 0, RetroNectin plates were washed twice with PBS (Ca/Mg-free) and viral supernatant was harvested from the HEK293T cells and transferred to the RetroNectin plates. Viral supernatant was then centrifuged at 2000xg for 1 hour to bring the viral supernatant and RetroNectin into close contact. BL/6 OTI splenocytes were isolated as described in 1.2.2, however once resuspended in CTL media supplemented with 100U/ml IL-2 and 10nM SIINFEKL, these cells were used to replace the viral supernatant solution in the RetroNectin coated wells. Cells were then centrifuged at 460xg for 4 minutes to bring the cells into close contact with the RetroNectin-bound viral particles on the bottom of the plate. Thus the naive CTLs were activated in the presence of virus and transduced over Days 0-3. On Day 3 cells were washed (by three washes in PBS (Ca/Mg-free)) to ensure removal of any remaining SIINFEKL peptide and cells were placed back in culture at 500,000 cells/ml in fresh CTL media containing 100U/ml IL-2. On Day 4, transduced cells (as determined by the expression of a fluorescent reporter) were FACS sorted, and maintained in culture until use in experiments, on days 4-8.

## **2.4 Cytotoxicity Assays**

### **2.4.1 <sup>51</sup>Cr release assay**

For <sup>51</sup>Cr release assays (Sutton et al., 2008) (Figs 3.5a,b, 3.6a,b, 3.7b, 3.9a,b, 3.10, 3.11),  $2 \times 10^6$  target cells were incubated with 200  $\mu$ Ci of <sup>51</sup>Cr (sodium chromate) in 200  $\mu$ L of complete DMEM media for 1 hour at 37 °C. Where required for antigen-dependent CTL killing assay (Figure 3.6b, 3.7b, 3.9b), 1  $\mu$ M SIINFEKL peptide (GenScript, New Jersey, USA) was included in this incubation step. After 1 hour, the cells were washed three times in media appropriate for the assay: RPMI supplemented with 0.1% BSA for cholesterol loading, DMEM supplemented with 0.1% BSA for perforin titration, and complete DMEM or RPMI for effector lymphocyte cytotoxicity assays. After washing excess <sup>51</sup>Cr, cells were either loaded with cholesterol (Figure 4.10), incubated with effector cells at the desired effector/target ratio for 4 hours (Figure 3.6a,b, 3.7b, 3.9b), or mixed with various amounts of recombinant perforin and incubated for 1 hour (Figure 3.5a,b, 3.9a, 3.10.). These assays were conducted in 96-well plates in either 200  $\mu$ L (OTI T cell assays) or 100  $\mu$ L reactions (recombinant perforin assays). The plates were then centrifuged, supernatant collected, and its radioactivity assessed using a 1470 Wizard Automatic Gamma Counter (Wallac, Turku, Finland). Percentage specific <sup>51</sup>Cr release was calculated as  $[(^{51}\text{Cr}_{\text{assay}} - ^{51}\text{Cr}_{\text{spontaneous}})/(^{51}\text{Cr}_{\text{total}} - ^{51}\text{Cr}_{\text{spontaneous}}) \times 100]$ ; <sup>51</sup>Cr<sub>total</sub> was the level of radioactivity in target cells lysed with 1% Triton X-100, and <sup>51</sup>Cr<sub>spontaneous</sub> was the level of radioactivity released by target cells incubated in the media in the absence of CTL or recombinant perforin for 4 hours or 1 hour, respectively.

### **2.4.2 Flow cytometry-based cytotoxicity assay**

For flow cytometry-based cytotoxicity assays, propidium iodide (PI) was used as a marker of cell death. Propidium iodide shows a large increase in fluorescence upon binding to DNA or RNA, and because it is impermeable to the cell membrane, it only binds nucleic acids once the cell has lost membrane integrity. For all PI cytotoxicity assays, at the end of the given experiment cells were resuspended in 100ul of 0.1% BSA DMEM containing 1 $\mu$ M PI and analysed by Flow cytometry.

## 2.5 Atomic Force Microscopy (Experiments designed and performed by Dr Adrian Hodel)

### 2.5.1 Lipid vesicle and AFM sample preparation

Mixtures of specific lipid ratios were induced to form vesicles, which contain an aqueous core surrounded entirely by a lipid bilayer (Figure 2.2a). These vesicles were then placed onto atomically flat mica substrates, and induced to burst, resulting in the formation of lipid bilayers on the mica surface (Figure 2.2b). These bilayers were then washed thoroughly in buffers appropriate for the individual experiments (see *Appendix 1- Detailed Atomic Force Microscopy Methods*).

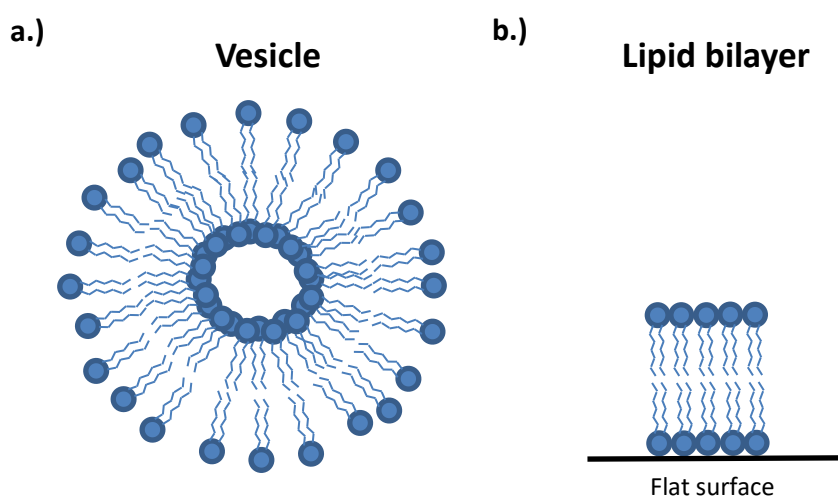
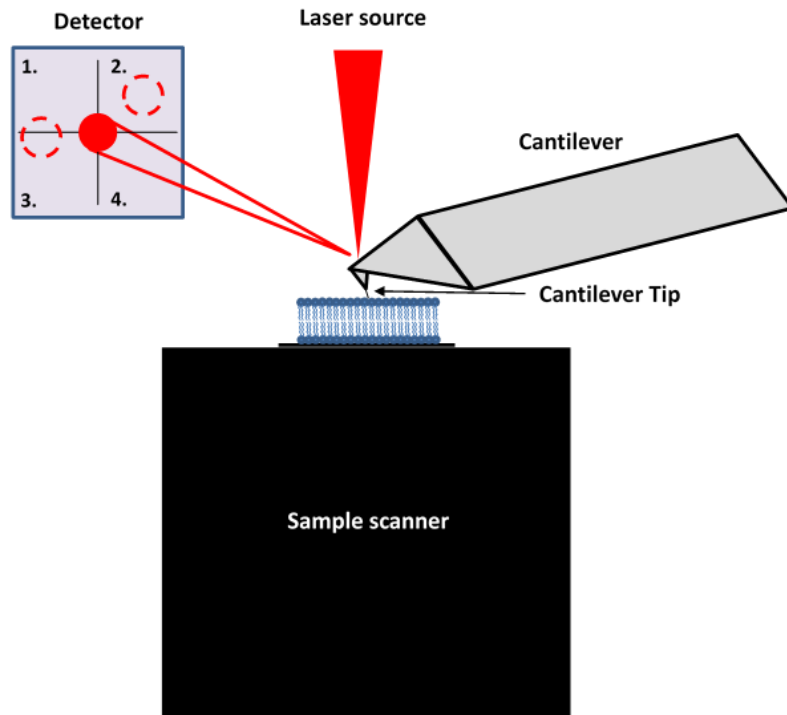


Figure 2.2: Schematic diagram of planar lipid bilayer creation.

- a.) Visual representation of a lipid vesicle
- b.) Visual representation of a lipid bilayer on a flat mica surface

### 2.5.2 AFM imaging and data processing

Atomic Force Microscopy (AFM) utilises the scanning of a fine probe to create a topographical map of the surface. The probe is scanned back and forth across the sample and the amount of deflection the probe experiences is measured by a laser which is directed at the top of the probe (Figure 2.3.) This measurement of deflection is indicative of variations in the height of the sample, allowing a detailed topographical map of the surface to be created (Figure 2.4). For a more detailed Materials and Methods for Atomic Force Microscopy, please refer to *Appendix 1- Detailed Atomic Force Microscopy Methods*.



**Figure 2.3: Schematic representation of an Atomic Force Microscope.**

A sample scanner moves the sample (lipid bilayer on mica substrate) back and forth underneath the cantilever tip. Laser shined onto the rear of the cantilever detects deflections in the cantilever due to interactions with the lipid bilayer surface which it is imaging. The characteristics of the surface determine the amount of deflection and therefore where the reflected laser signal is detected, allowing information about the surface to be obtained. \*These experiments are conducted in liquid, however the liquid surrounding the lipid bilayer is not shown, for clarity.

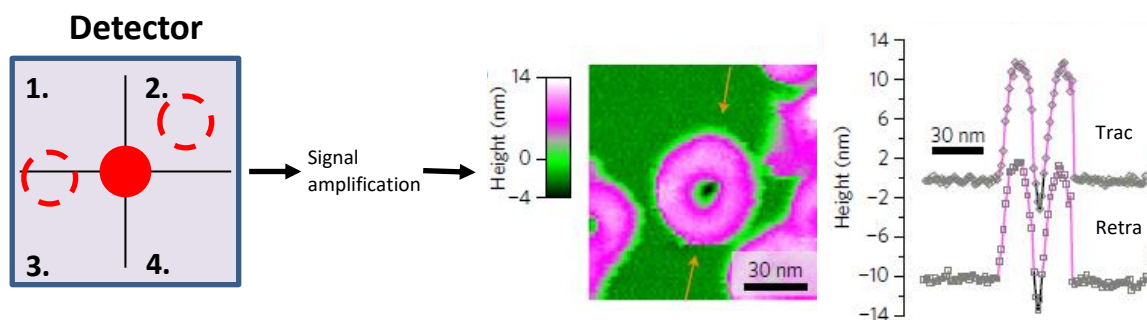


**Figure 2.4: Atomic Force Microscopy provides a topographical map of the sample surface.**

The signal collected from the movement of the cantilever is converted into 3D topography of the sample surface. In this example, adapted from (Leung et al., 2017), a perforin pore is seen sitting within the lipid bilayer. Height trace analysis (far right) shows much of the perforin pore sitting above the lipid bilayer, with a hole punched through the lipid bilayer in the centre.

## Chapter 3 Cytotoxic lymphocytes are resistant to perforin binding and lysis

### 3.1 Introduction

Early studies of perforin activity identified that both primary cytotoxic lymphocytes and cytotoxic lymphocyte cell lines are resistant to perforin relative to their target cells (Blakely et al., 1987; Shinkai et al., 1988; Verret et al., 1987). An initial report suggested Homologous Restriction Factor as a broad means of CTLs protection (Zalman et al., 1987), however this was quickly disputed and disproven (S. B. Jiang et al., 1988). In 1994, Tschopp and Muller provided indirect evidence for a molecule responsible for cell protection specifically against perforin (Müller & Tschopp, 1994). Since then a number of suggestions as to this molecule's identity have been raised without any unequivocal conclusions being drawn. The idea that a molecule expressed on the surface of the cytotoxic lymphocyte specifically during synapse formation provides that cytotoxic lymphocyte with protection against perforin within the synapse has been an appealing one within the field, owing to the logic of such a hypothesis.

The lysosomal protease Cathepsin B was suggested as the basis for one such mechanism of lymphocyte protection from the secreted perforin. This was based on *in vitro* observations of cytotoxic lymphocytes losing self-protection, when they degranulated in the presence of cathepsin B inhibitors (Balaji et al., 2002). This putative protective mechanism was not supported by subsequent *in vivo* studies, where cytotoxic lymphocytes from cathepsin B-deficient mice retained full function and were not adversely affected by the loss of cathepsin B (Baran et al., 2006).

More recently, the externalisation of heavily glycosylated Lysosomal Associated Membrane Protein – 1 (LAMP-1/CD107a) on the cytotoxic lymphocyte cell surface during degranulation was proposed as a mechanism for perforin resistance (Cohnen et al., 2013). LAMP-1, along with LAMP-2, is the most abundant membrane protein in lysosomes (Marsh et al., 1987). LAMP-1 is made up of two N glycosylated peptide regions (amino acid positions 26-189 and amino acid positions 220-371) connected through an O-Glycosylated 'hinge' motif (amino acid positions 190-219), a transmembrane domain and a short cytoplasmic C terminal region (Fukuda, 1991). The hinge region and two main glycosylation regions reside within the lumen of the lysosome, and are only externalised upon the fusion of the secretory granule with the plasma membrane during degranulation. Cohnen et al hypothesised that the LAMP-1 O-linked glycans exposed on the cytotoxic lymphocyte membrane during degranulation were responsible for interfering with perforin function (Cohnen et al., 2013).

The cytoplasmic C-terminal region of LAMP-1 is essential for targeting LAMP-1 to lysosomes (Williams & Fukuda, 1990), and the removal of that C-terminal His-Ala-Gly-Tyr (HAGY) peptide leads to LAMP-1 retention on the plasma membrane (Cohnen et al., 2013) (Figure 3.1).

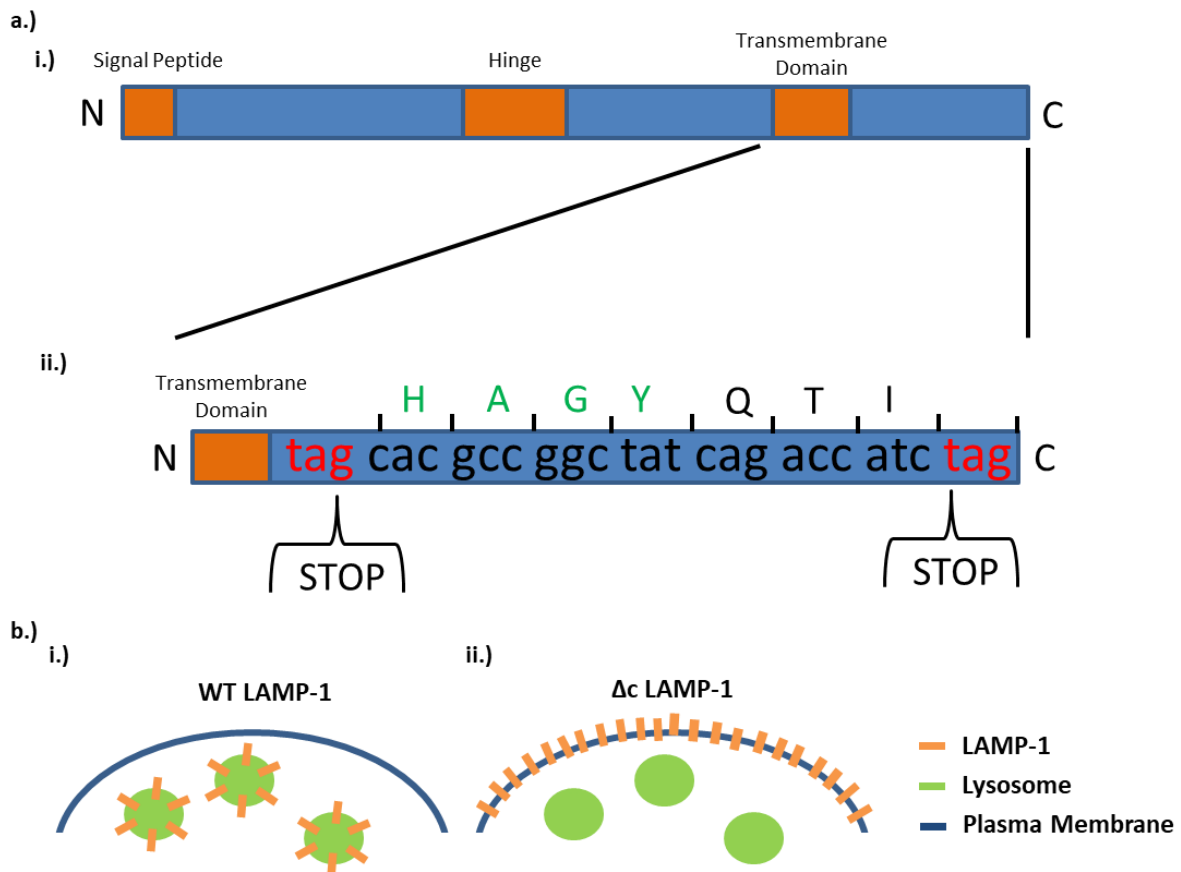


**Figure 3.1: Schematic diagram of the LAMP-1 protein highlighting lysosomal targeting motif.**

a.) Truncation position for  $\Delta c$ -LAMP-1 relative to that of WT LAMP-1. Position of the lysosomal targeting motif HAGY is shown in green, located between the respective STOP codons of WT and  $\Delta c$ -LAMP-1. Image adapted from (Cohnen et al., 2013)

b.) The deletion of the LAMP-1 lysosomal targeting motif HAGY results in  $\Delta c$ -LAMP-1 retention on the plasma membrane: i.) Wild-type (WT) LAMP-1 is localised to the lysosomal membrane, and only exposed on the surface of the plasma membrane after fusion of secretory lysosomes during degranulation. ii.)  $\Delta c$ -LAMP-1 is exposed constitutively on the plasma membrane surface.

After showing moderate levels of resistance against cytotoxic granules and NK cell mediated lysis for target cells expressing the truncated mutant of LAMP-1, Cohnen et al (Cohnen et al., 2013) suggested that cell surface LAMP-1 was crucial for a cytotoxic lymphocyte protection against secreted perforin and, therefore, ability to survive an immune synapse interaction. However, in the same study, NK cells from LAMP-1 deficient mice showed only moderately higher levels of annexin V positivity (used to indicate cell death in this study) after incubation with target cells, and also no decrease in their killing capacity. These apparent inconsistencies cast some doubts over the importance of LAMP-1 for cytotoxic lymphocyte resistance to perforin. It was also of note that approximately 15% of WT cytotoxic lymphocytes were shown to die during synapse formation in this study, which was inconsistent with our previously published single cell analyses where only a tiny proportion of effector cells was permeabilised by perforin within an immunological synapse (<1%) (Lopez, Jenkins, et al., 2013). These considerations led us to revisit the role of LAMP-1 in cytotoxic lymphocyte protection against perforin.



## 3.2 Materials and Methods

### 3.2.1 Cloning of LAMP-1 constructs

For experiments performed with LAMP-1, the same premature stop codon as used in (Cohnen et al., 2013) was introduced to truncate the C terminal region and create cell surface LAMP-1 retention. This plasmid was cloned into the multiple cloning site of Murine Stem Cell Virus (MSCV) containing IRES-GFP using the restriction enzymes EcoR1 and BamH1 (Figure 3.2), and is denoted  $\Delta$ c-LAMP-1 in the remainder of this thesis.

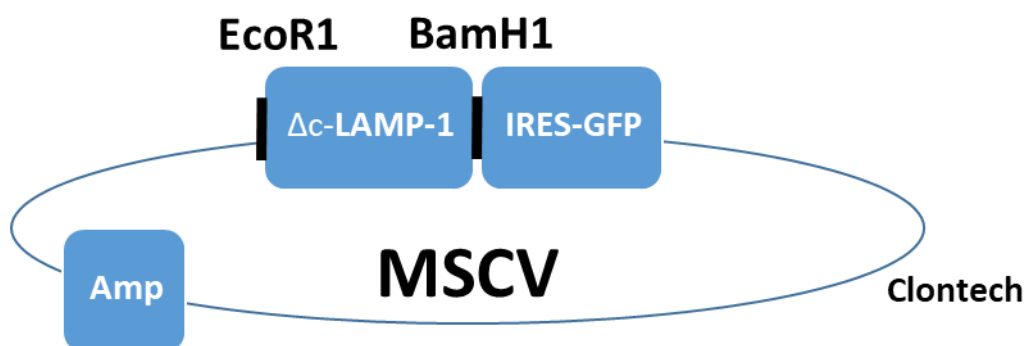


**Figure 3.2: Vector map showing details of  $\Delta$ c-LAMP-1 MSCV-IRES-GFP cloning.**

$\Delta$ c-LAMP-1 was cloned into the multiple cloning site of MSCV-IRES-GFP using EcoR1 and BamH1. Amp: ampicillin resistance cassette,  $\Delta$ c-LAMP-1: Truncated LAMP-1 sequence, IRES: Internal Ribosome Entry Site, GFP: Green Fluorescent Protein.

### 3.2.2 Transduction of LAMP-1 constructs

Lamp-1 constructs were transduced following the methods described in 2.3.1 and 2.3.2.

### 3.2.3 Flow Cytometry

#### 3.2.3.1 Fluorescence activated cell sorting for equal protein expression

To obtain consistent levels of reporter GFP expression on transduced cells isolated in different experiments, GFP Fluorescent beads were used to calibrate the ARIAII flow cytometer prior to each cell sort. Cells from the control group (MSCV-IRES-GFP) and the  $\Delta$ c-LAMP-1 group were then sorted for equivalent reporter GFP expression (Figure 3.3). All sorting was performed at room temperature under sterile conditions.

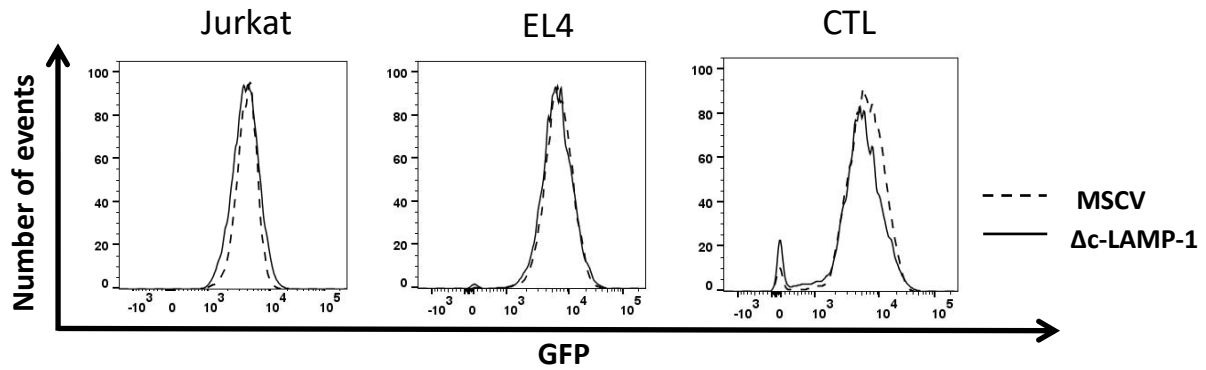


**Figure 3.3: Analysis of plasmid expression levels of transduced Jurkat, EL4 and OTI CTL.**

After sorting for equal GFP reporter expression by flow cytometry, each of Jurkat, EL4 and OTI CTL cells transduced with either  $\Delta c$ -LAMP-1 MSCV-IRES-GFP or empty MSCV-IRES-GFP control showed equal GFP plasmid reporter levels on the day of experiments.

### 3.2.3.2 Surface staining

For detection of cell surface expressed proteins, cells were washed in BSA DMEM, maintained on ice and labelled with the antibody of interest (anti-CD8-allophycocyanin (APC) or anti-CD107a-Phycoerythrin (PE)) for 20 minutes. Cells were then washed and resuspended in 100 $\mu$ l of 0.1% BSA DMEM, to be analysed on a Canto 2 flow cytometer (BD Biosciences, New Jersey, USA) (Figures 3.4a, b, 3.7a, 3.8). Cells were maintained on ice until analysis.

### 3.2.4 Recombinant perforin cytotoxicity assays

As per section 2.4.1 in general Materials and Methods.

### 3.2.5 CTL cytotoxicity assay

$^{51}\text{Cr}$  release cytotoxicity assay was conducted as per section 2.4.1.

### 3.2.6 Validation of TMH1-GFP-PRF

$^{51}\text{Cr}$  labelled EL4 cells were incubated with increasing amounts of TMH1-GFP-PRF, washed, and then resuspended in serum free media where the cell bound mutant perforin (with an artificial disulphide bridge – see (Leung et al., 2017)) was unlocked by addition of 0.75mM DTT (dithiothreitol). After a 5 minute incubation, BSA was added to the media to quench DTT, and cells were incubated for a further 60 minutes at 37°C (allowing unlocked perforin to lyse the cells). Cell supernatants were then harvested and specific  $^{51}\text{Cr}$  release calculated (Figure 3.11) using the formula detailed in 2.4.1.

### **3.2.7 TMH1-GFP-PRF binding assay**

“Cells were washed three times in DMEM containing 0.1% BSA (Roche Diagnostics, Mannheim, Germany) and resuspended at  $10^6$  cells/mL. EL4 (not pulsed with the SIINFEKL antigen) and CTLs were then mixed 1:1 to remain at a final concentration of  $10^6$  cells/mL. TMH1-GFP-PRF was added to the mixture, and cells were incubated at 37 °C for 30 min. Unbound perforin was removed by washing the cells in 0.1% BSA DMEM, cells were stained with anti-CD8 APC (eBioscience, California, USA) and analysed using a Fortessa X20 flow cytometer (BD Biosciences, New Jersey, USA) (Figure 3.12).”

### 3.3 Results

#### 3.3.1 Does cell surface LAMP-1 protect cells against perforin?

*This section (3.3.1) was completed prior to the commencement of my degree, and is included to provide context to the study. All experiments within this section were performed by me.*

The first step in testing LAMP-1 externalisation as a protective mechanism was to create stable cell lines that overexpress LAMP-1 on their surface. To do this, the mutant form of LAMP-1 ( $\Delta$ c-LAMP-1) was cloned into an MSCV-IRES-GFP vector, and human (Jurkat) and murine (EL4) cell lines were transduced and sorted for the same GFP reporter expression as an empty MSCV transduced cells, as described in Materials and Methods. A >1000-fold difference of surface LAMP-1 geometric Mean Fluorescence Intensity (MFI) was observed between the MSCV only control and the  $\Delta$ c-LAMP-1 transduced Jurkat cells (Figure 3.4a), and a 37-fold difference observed for EL4 (Figure 3.4b). The 2013 publication by Cohnen et al does not specify the fold difference in LAMP-1 MFI between control cells and those expressing cell surface LAMP-1 therefore a direct comparison of the surface level of LAMP-1 between this study and theirs is not possible. However, the histograms provided in their publication (See Figure 3.4c below) show a similar increase in surface LAMP-1 as that shown in Figure 3.4 a, b below.

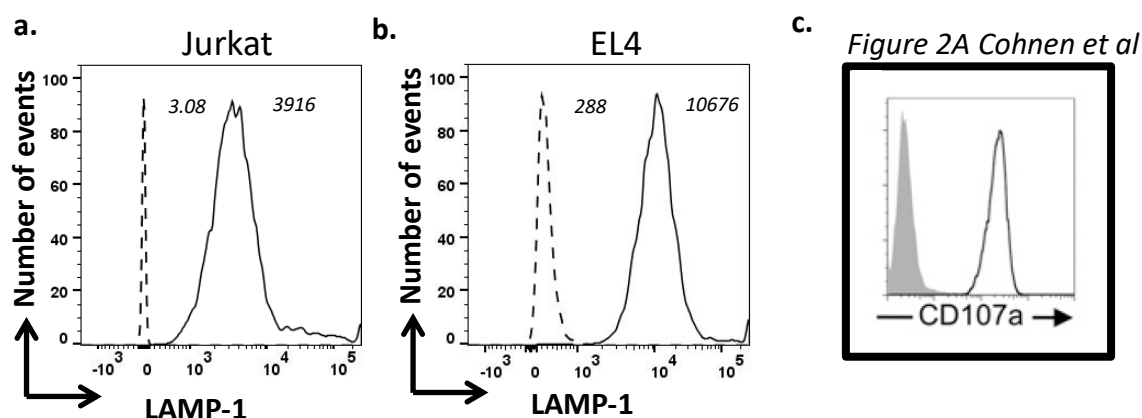


**Figure 3.4: Analysis of surface LAMP-1 levels in cell lines transduced with MSCV-GFP or  $\Delta$ c-LAMP-1-MSCV-GFP.**

**a.)** Jurkat cells transduced with  $\Delta$ c-LAMP-1 (shown by solid line) have >1000 fold higher MFI of LAMP-1 than Jurkat cells transduced with an empty vector (shown by dashed line), as detected by surface staining with anti-CD107a-Phycoerythrin (PE) antibody.

**b.)** EL4 cells transduced with  $\Delta$ c-LAMP-1 (shown by solid line) have a 37 fold higher MFI of LAMP-1 than EL4 cells transduced with an empty vector (shown by dashed line), as detected by surface staining with anti-CD107a-Phycoerythrin (PE) antibody. Both histograms are representative examples of flow cytometry analysis performed on the day of every experiment, the number of events has been standardized to the mode to allow clear comparison of both histograms and geometric mean fluorescence intensity (MFI) values from which fold difference values were calculated are shown next to each peak.

**c.)** Histogram demonstrating LAMP-1 surface expression, detected by CD107a antibody (solid black line) or isotype control (shaded), of HeLa cells used by (Cohnen et al., 2013).

To investigate a putative role for LAMP-1 in perforin resistance, the transduced cell lines were exposed to increasing amounts of recombinant WT perforin. The results showed that  $\Delta c$  LAMP-1 transduced cells were as sensitive to perforin lysis as cells with basal levels of LAMP-1 expression (empty vector) (Figure 3.5 a,b). This was in contrast to previously published data (Cohnen et al., 2013) showing reduced granule extract lysis of cell lines stably expressing surface LAMP-1 (See Figure 3.5 c below)

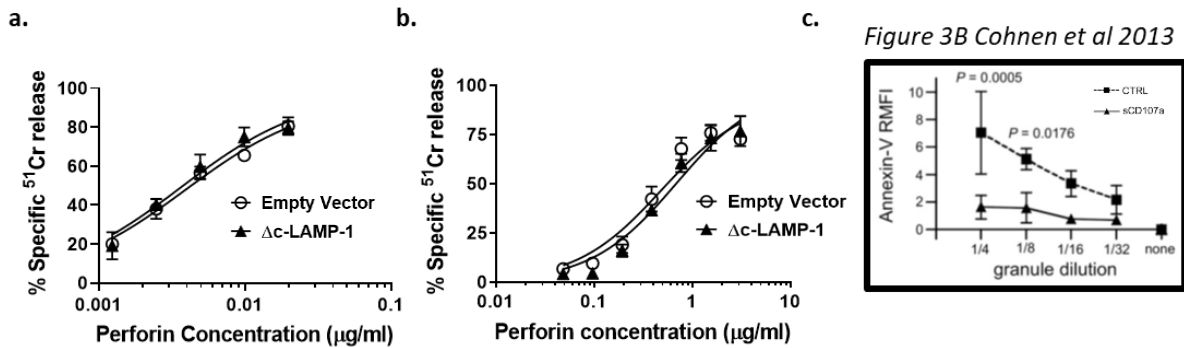


**Figure 3.5: High surface levels of LAMP-1 do not protect common target cell lines from perforin lysis.**

- a.) Jurkat cells expressing high surface levels of LAMP-1 ( $\Delta c$ -LAMP-1) are not protected from recombinant perforin lysis relative to cells expressing constitutive surface levels of LAMP-1 (Empty Vector)
- b.) EL4 cells expressing high surface levels of LAMP-1 ( $\Delta c$ -LAMP-1) are not protected from recombinant perforin lysis compared to cells expressing constitutive surface levels of LAMP-1 (Empty Vector).
- c.) Relative Median Fluorescence Intensity levels of Annexin V (used as an indicator of cell death) on HeLa cells expressing high surface levels of LAMP-1 (sCD107a) or constitutive surface levels of LAMP-1 (CTRL) after incubation with cytotoxic granules. Image taken from Figure 3B in (Cohnen et al., 2013).

Transduced cell lines were then used as targets for cytotoxic lymphocytes. If LAMP-1 exposure protected cells from perforin, reduced killing would be expected in the  $\Delta c$ -LAMP-1 expressing cells, as perforin activity is crucial for the delivery of granzymes into the target cell cytosol to initiate apoptosis (Voskoboinik et al., 2015). Jurkat cells expressing high ( $\Delta c$ -LAMP-1) and constitutive (MSCV vector alone) levels of surface LAMP-1 were incubated with isolated primary human NK cells, and no difference in killing levels was observed (Figure 3.6a). To further investigate any potential protection surface LAMP-1 may provide against cytotoxic lymphocytes, EL4 cells expressing high ( $\Delta c$ -LAMP-1) and constitutive (MSCV) levels of surface LAMP-1 were labelled with the SIINFEKL peptide antigen and used as targets for syngeneic BL/6.OTI CTLs. Similar to the results with NK cells, no difference in killing levels between the two types of target cells was observed (Figure 3.6b). This is in contrast to Figure 2a from Cohnen et al (Cohnen et al., 2013), which demonstrated protection of HeLa cells expressing surface LAMP-1 from NK cell killing using  $^{51}\text{Cr}$  release assays (See Figure 3.6c below). We have, therefore, shown with recombinant perforin as well as in two different cellular systems (representing innate and adaptive immunity) that high surface levels of LAMP-1 do not protect cells from perforin or cytotoxic lymphocyte killing.

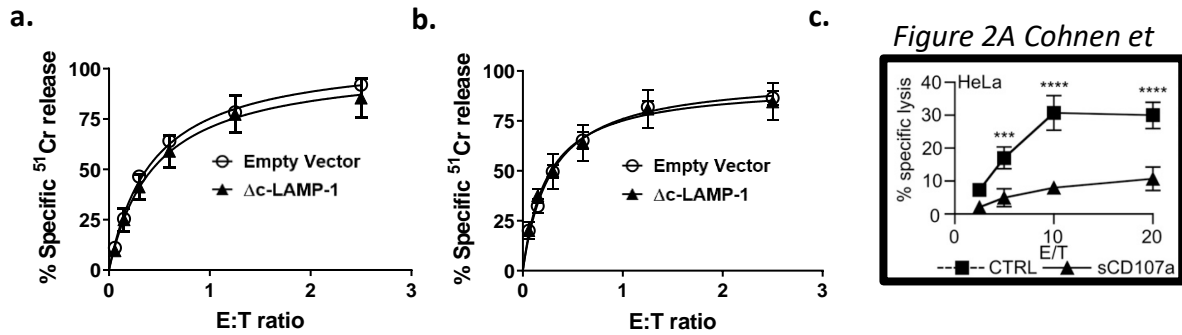


**Figure 3.6: High surface levels of LAMP-1 do not protect common target cell lines from cytotoxic lymphocyte killing**

**a.)** Specific <sup>51</sup>Cr release of Jurkat cells upon incubation with IL-2 activated primary human NK cells, graphed as a function of the effector to target cell ratio (E:T ratio). There is no significant difference in killing levels between Jurkat cells transduced with an empty vector and with Δc-LAMP-1. Each data point represents a mean ( $\pm$  s.e.m.) of 3 independent experiments; curves represent Michaelis-Menten fits to the data.

**b.)** Specific <sup>51</sup>Cr release of SIINFEKL labelled EL4 cells upon incubation with activated WT OTI cells, graphed as a function of the effector to target cell ratio (E:T ratio). There is no significant difference in killing levels between EL4 cells transduced with an empty vector and with Δc-LAMP-1. Each data point represents a mean ( $\pm$  s.e.m.) of 3 independent experiments; curves represent Michaelis-Menten fits to the data.

**c.)** Percentage specific lysis incurred by control (CTRL) and high LAMP-1 surface expressing (Scd107A) HeLa cells incubated with IL-2 activated human NK cells, image taken from Figure 2A, (Cohnen et al., 2013).

With no significant protection observed in this model system, it was decided to transduce Δc-LAMP-1 into primary murine WT CTLs in order to examine the effect of LAMP-1 surface exposure on the cytotoxic activity of these cells, i.e. whether surface expression of LAMP-1 makes these cells more efficient killers. Figure 3.7a shows a representative histogram of surface LAMP-1 expression for both the Δc-LAMP-1 transduced cells and MSCV only control. A 46-fold difference in LAMP-1 MFI was observed. Figure 3.7b shows that WT OTI CTL's that possess high levels of surface LAMP-1 do not become more efficient killers.

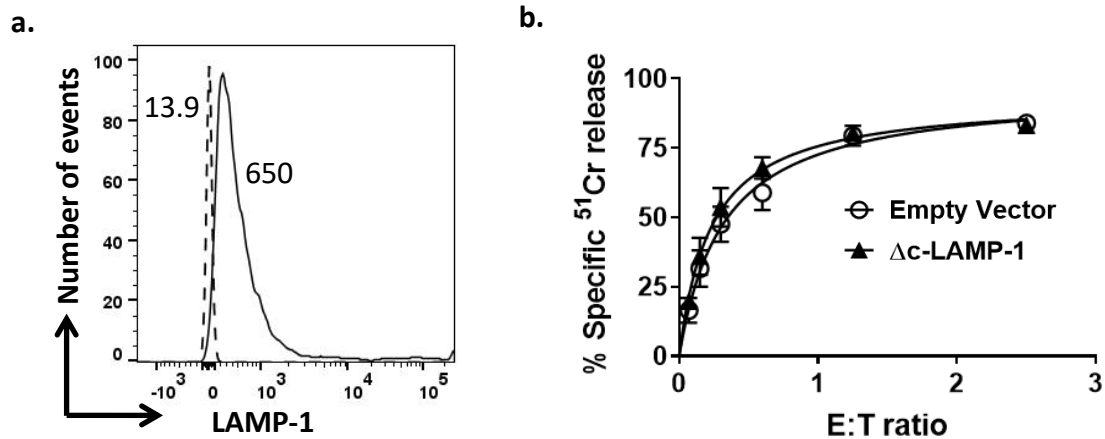


**Figure 3.7: Analysis of surface LAMP-1 levels and killing efficiency of WT OTI CTLs transduced with MSCV-IRES-GFP or  $\Delta$ c-LAMP-1 MSCV-IRES-GFP.**

**a.)** WT OTI CTLs transduced with  $\Delta$ c-LAMP-1 (shown by solid line) have a 46 fold higher MFI of LAMP-1 than WT OTI CTLs transduced with an empty vector (shown by dashed line), as detected by surface staining with anti-CD107a-Phycoerythrin (PE) antibody. Histogram is a representative example of flow cytometry analysis performed on the day of every experiment, the number of events has been standardized to the mode to allow clear comparison of both histograms and geometric mean fluorescence intensity (MFI) values from which fold difference values were calculated are shown next to each peak.

**b.)** Specific <sup>51</sup>Cr release of SIINFEKL labelled EL4 cells upon incubation with activated WT OTI CTLs, graphed as a function of the ratio of the effector to target cell ratio (E:T ratio). There is no significant difference in killing efficiency between WT OTI CTLs transduced with an empty vector and those transduced with  $\Delta$ c-LAMP-1. Each data point represents a mean ( $\pm$  s.e.m.) of 3 independent experiments; curves represent Michaelis-Menten fits to the data

After observing no increase in the killing efficiency of WT OTI CTLs transduced with  $\Delta$ c-LAMP-1, it was decided to transduce  $\Delta$ c-LAMP-1 into primary murine *Prf1*<sup>-/-</sup> OTI CTLs, to determine if the overall CTL membrane of  $\Delta$ c-LAMP-1 expressing cells was more resistant to recombinant perforin than cells transduced with the empty vector control. Figure 3.8 shows a representative histogram of surface LAMP-1 expression for both the  $\Delta$ c-LAMP-1 transduced *Prf1*<sup>-/-</sup> OTI CTLs and MSCV only control. A 135 fold difference in surface LAMP-1 MFI was observed.

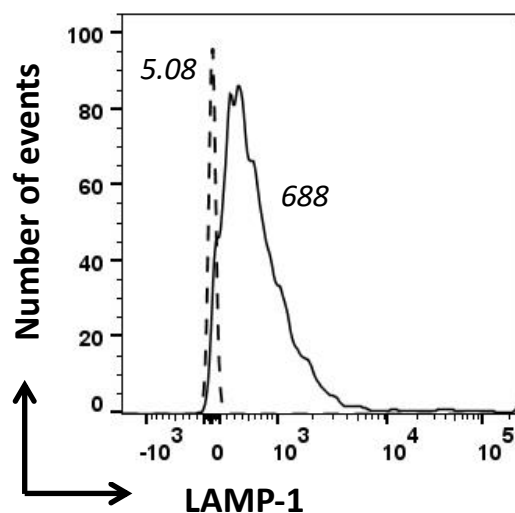


**Figure 3.8: Analysis of surface LAMP-1 levels in *Prf1*<sup>-/-</sup> OTI CTLs transduced with MSCV-IRES-GFP or  $\Delta$ c-LAMP-1 MSCV-IRES-GFP.**

*Prf1*<sup>-/-</sup> OTI CTLs transduced with  $\Delta$ c-LAMP-1 (shown by solid line) have a 135 fold higher MFI of LAMP-1 than *Prf1*<sup>-/-</sup> OTI CTLs transduced with an empty vector (shown by dashed line), as detected by surface staining with anti-CD107a-Phycoerythrin (PE) antibody. Histogram is a representative example of flow cytometry analysis performed on the day of every experiment, the number of events has been standardized to the mode to allow clear comparison of both histograms and geometric mean fluorescence intensity (MFI) values from which fold difference values were calculated are shown next to each peak.

The transduced CTLs expressing high levels of LAMP-1 on their cell surface and those which had constitutive surface exposure of LAMP-1 (empty vector) showed equal sensitivity to recombinant perforin (Figure 3.9a), similar to the earlier observations using target cells (Figure 3.5). Transduced *Prf1*<sup>-/-</sup> OTI CTLs still expressed MHC1 (required for SIINFEKL antigen presentation), therefore it was possible to use them as targets for WT OTI CTL killing. Once again, consistent with our experiments using cell lines overexpressing  $\Delta$ c-LAMP-1, *Prf1*<sup>-/-</sup> OTI CTLs with high surface LAMP-1 expression were not protected from WT OTI CTL killing (Figure 3.9b).



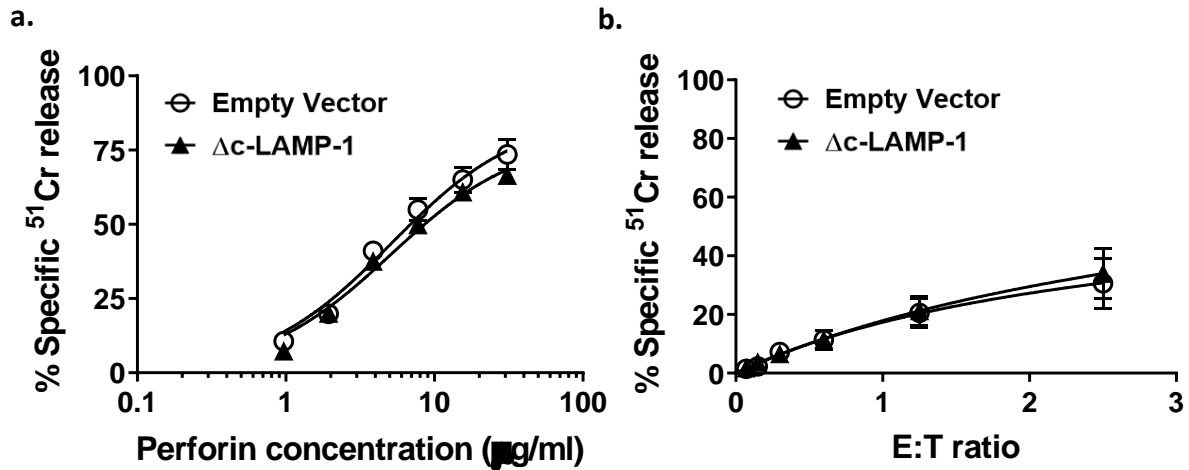


**Figure 3.9: High surface levels of LAMP-1 do not protect *Prf1*<sup>-/-</sup> OTI CTLs from recombinant perforin lysis or killing by WT OTI CTLs.**

**a.)** <sup>51</sup>Cr release of *Prf1*<sup>-/-</sup> OTI CTLs upon exposure to recombinant WT-PRF. There is no significant difference in sensitivity between cells transduced with an empty vector and with Δc-LAMP-1.

**b.)** Specific <sup>51</sup>Cr release of SIINFEKL labelled *Prf1*<sup>-/-</sup> OTI CTLs upon incubation with activated WT OTI CTLs, graphed as a function of the ratio of the effector to target cell ratio (E:T ratio). There is no significant difference in killing levels between *Prf1*<sup>-/-</sup> OTI CTLs transduced with an empty vector and those transduced with Δc-LAMP-1. Each data point represents a mean (± s.e.m.) of 3 independent experiments; curves represent Michaelis-Menten fits to the data.

Taken together, these results contradict findings by (Cohnen et al. 2013) and strongly suggest that LAMP-1 externalisation is not important for cytotoxic lymphocyte resistance to perforin. What was interesting to note from these experiments however, was the vast difference in sensitivity of CTL and EL4 target cells to perforin: compare perforin concentration required for 50% lysis in figure 3.9a and figure 3.5b. Even though these experiments were not conducted simultaneously, the difference in perforin sensitivity was so prominent that we went on to investigate it further.

### 3.3.2 Primary protection; primary cytotoxic lymphocytes are less sensitive to recombinant perforin lysis when compared to common cell lines

Sections (3.3.2 and 3.3.3) were completed with the technical assistance of Ms. Tahereh Noori. After I designed and optimised the experiments, she performed independent replicates and collated the data. I finalised all data presentation and calculated the fold difference values detailed in Fig 3.10.

Having observed that higher levels of perforin may be required to achieve lysis of CTLs compared to the EL4 target cells, it was decided to directly compare CTL and their commonly used *in vitro* targets. This type of experiment has been performed previously using granule extract (Blakely et al., 1987; Verret et al., 1987), however without the availability of purified recombinant perforin there is a potential for contamination with granzymes/proteases which could potentiate cell death through synergy with perforin. Here we compared cytotoxic lymphocyte resistance to recombinant purified perforin using the  $^{51}\text{Cr}$  release assay. In agreement with our preliminary observations (Figure 3.5b and 3.9a) CTL and NK cells were 155 and 331 fold more resistant to Perforin than their respective targets, EL4 and P815 (Figure 3.10).

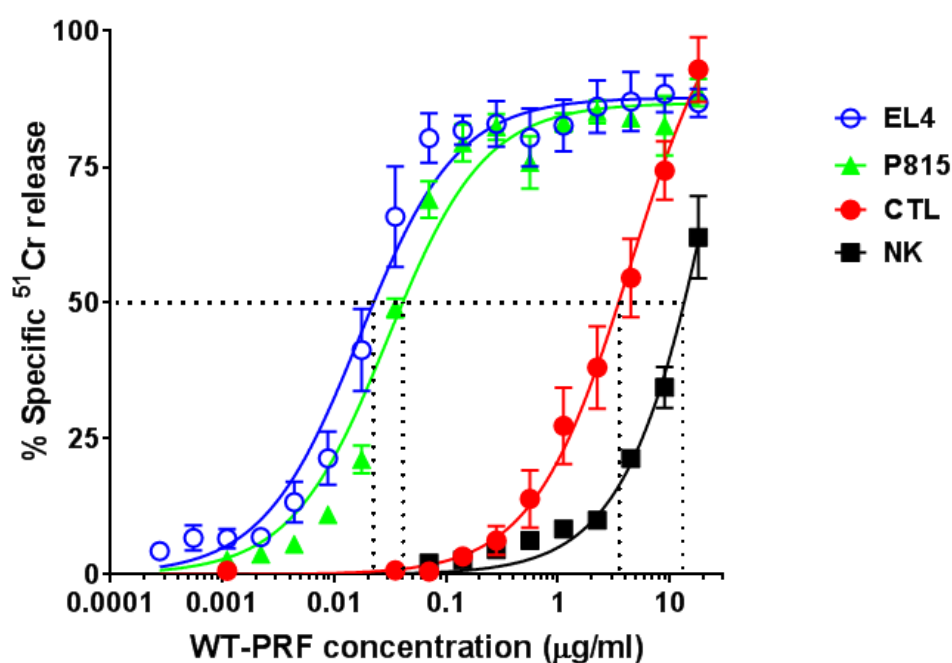


**Figure 3.10: “Cytotoxic lymphocytes are resistant to perforin lysis.**

Sensitivity of CTLs, natural killer (NK) cells, EL4 and P815 target cells to recombinant WT-PRF was assessed using  $^{51}\text{Cr}$  release cytotoxicity assay. Cytotoxic lymphocytes are 155 (CTL) and 331 (NK) fold more resistant than their respective target cells (EL4 and P815), as assessed at 50%  $^{51}\text{Cr}$  release (dotted lines). Each data point represents a mean ( $\pm$  standard error of mean, s.e.m.) of 3 independent experiments. Curves represent Michaelis-Menten fits to the data.”

This striking difference, combined with the recent single cell analysis showing that the cytotoxic lymphocyte membrane almost invariably remains intact within the immune synapse (Lopez, Jenkins, et al., 2013), it became apparent that cytotoxic lymphocyte resistance to perforin lysis is a crucial part of cytotoxic lymphocyte self-protection. The question to be addressed is then: How does the cytotoxic lymphocyte membrane resist perforin lysis?

A method was developed to test if the CTLs were inherently resistant to any of the three stages of perforin pore formation: plasma membrane binding, insertion and lysis. At 37°C, WT-PRF binds, inserts and forms cytolytic pores on the plasma membrane of cells. Therefore, to uncouple perforin binding from insertion and pore formation, a non-lytic mutant was required. The previously described TMH1-PRF mutant (Leung et al., 2017) provides such a non-lytic form of perforin. Mutations replacing alanine and tryptophan residues at amino acid position 144 and 373, respectively, with cysteine residues results in the formation of a new, reversible disulphide bridge that tethers TMH1 to the much larger MACPF domain. The mutations do not affect calcium dependent membrane binding, however, as the TMH1 region is locked in this manner, it is unable to unfurl and insert into the membrane. By unlocking the disulphide bond, using the reducing agent DTT, the activity of the perforin can be restored (Leung et al., 2017).

To visualise perforin on the cell, we previously generated PRF-GFP fusion protein, which maintained recombinant WT activity (Lopez, Susanto, et al., 2013). We, therefore, decided to generate TMH1-GFP fusion protein. To maintain consistency with our perforin binding assay experimental conditions, where whole cells were exposed to TMH1-GFP PRF and GFP fluorescence detected, the ability of DTT to reduce the disulphide bond and unlock TMH1 was tested in a whole cell setting. Without DTT addition, none of the perforin concentrations tested affected cell viability. However, following addition of 0.75mM DTT, cell viability decreased with increasing perforin concentration (Figure 3.11), similar to the earlier report using TMH1-PRF (Leung et al., 2017). Importantly, DTT alone showed no effect on cell viability based on a control group included within these chromium assays in which cells were treated with DTT but not perforin (data not shown). This experiment confirms that TMH1-GFP-PRF mimics the ability of TMH1-PRF to be 'unlocked' by reducing the disulphide bridge. We, therefore, validated an experimental system that enabled us to uncouple and visualise PRF binding to the plasma membrane, and monitor this separately from target cell lysis using flow cytometry and microscopy.

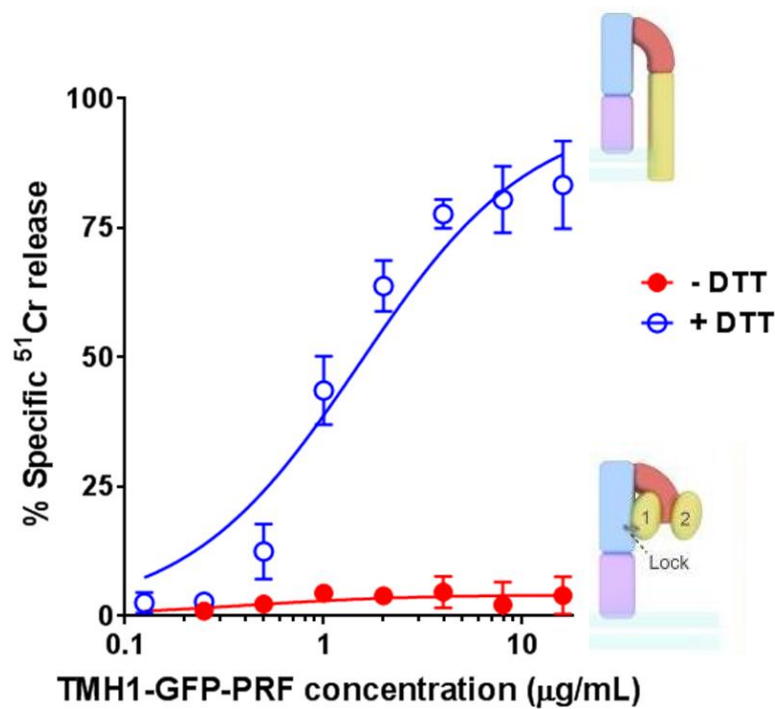


**Figure 3.11: “Functionality of TMH1-GFP-PRF as assessed by <sup>51</sup>Cr release assay.**

Recombinant TMH1-GFP-PRF is not cytotoxic to EL4 cells over a wide range of perforin concentrations (-DTT). However, when 0.75 mM DTT is added to this cell-bound perforin, the engineered disulphide-bond of TMH1-GFP-PRF is unlocked. As a consequence, non-toxic TMH1-GFP-PRF becomes cytolytic, as demonstrated by EL4 cell lysis (TMH1-GFP-PRF concentration-dependent <sup>51</sup>Cr release in the presence of DTT). Each data point represents a mean ( $\pm$  standard deviation, SD) of 3 independent experiments; curves represent Michaelis-Menten fits to the data. Perforin schematics show the locked and unlocked TMH regions and are adapted from (Leung et al. 2017).”

### 3.3.3 Differential perforin binding to CTLs and target cells

Having confirmed that TMH1-GFP-PRF and WT-PRF have similar membrane binding properties, an assay was designed to assess TMH1-GFP-PRF (as a surrogate WT-PRF) binding to whole cells. The fluorescence of cells which have been incubated with TMH1-GFP-PRF can be easily assessed by flow cytometry as a read-out of perforin binding. To compare perforin binding to two different cell types, the cells were first combined in a 1:1 mixture to ensure perforin binding conditions were the same for both cell types. After perforin incubation and subsequent washing, cells were stained with anti-CD8-allophycocyanin (APC) to allow differentiation of the two cell types during analysis. In this way, once the cells had been analysed by flow cytometry, the Geometric mean fluorescence of the GFP channel could be calculated separately for both the CD8 positive and negative cells. However, when comparing two different cell types in this way, disparities in cell size need to be addressed. Any difference in cell surface area may affect the available membrane surface for perforin to bind to, and therefore affect the measured fluorescence geometric mean intensity. Therefore, during analysis the viable cell morphology gates were set based on individual cell controls, first including all viable EL4s, then modified from that gate to include only the overlapping morphology region existing with CTLs (Figure 3.12a). The two cell types were then differentiated by their anti-CD8-allophycocyanin (APC) signal (as CD8 is only expressed on the CTLs), and their GFP binding levels analysed (Figure 3.12b).

Using these optimised experimental conditions, it was found that the amount of TMH1-GFP-PRF bound to the CTLs is only one-third to one-half the amount bound to CD8<sup>-</sup> cells (EL4) (Figure 3.12c). However, the difference in perforin bound was not large enough to solely account for the difference in perforin lysis levels found between EL4 and OTI CTLs (Figure 3.10). This suggested that reduced perforin binding on the CTL membrane is at best only partly responsible for perforin resistance, prompting us to investigate further – as described in the following chapters.

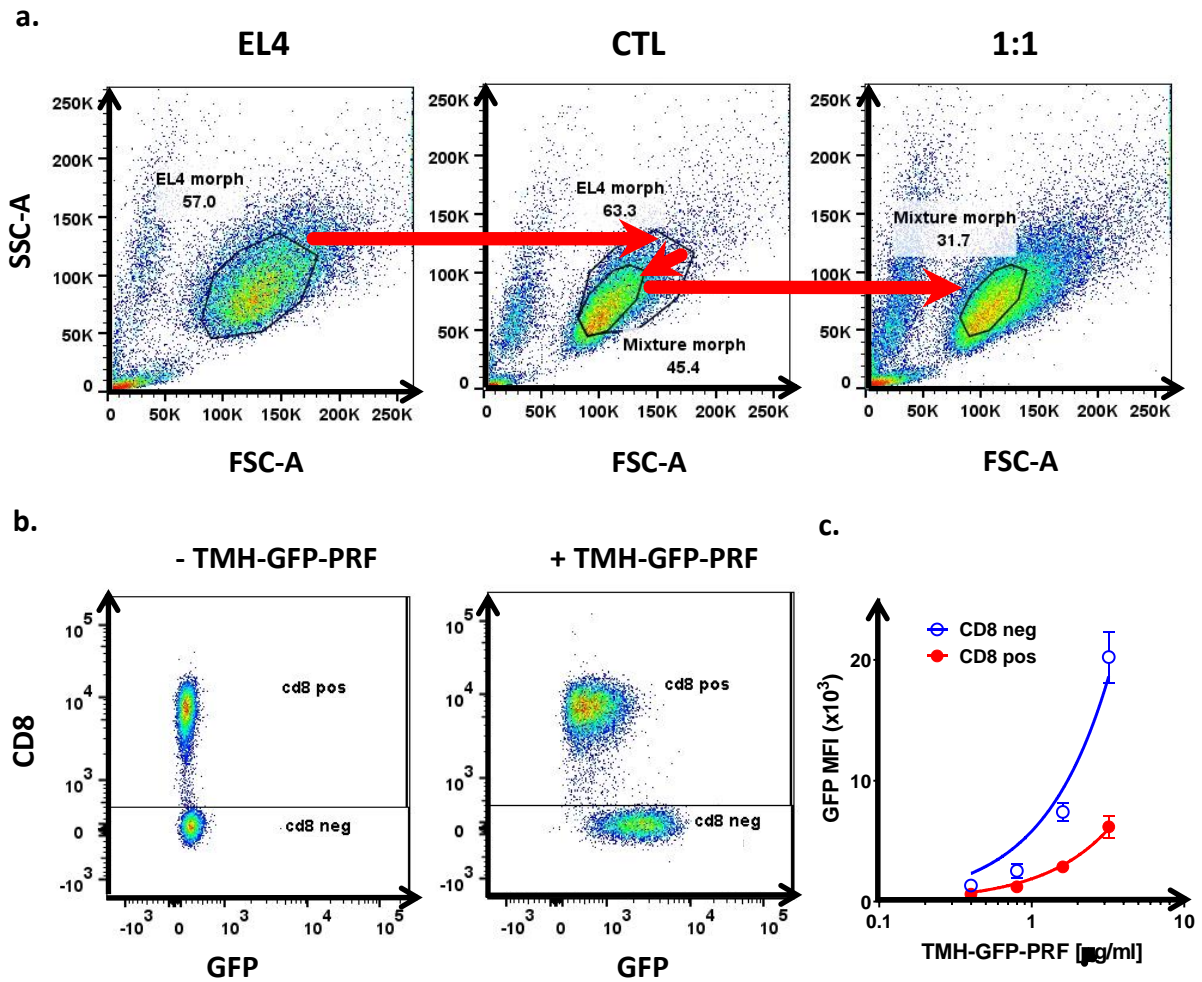


**Figure 3.12: “Binding of TMH1-GFP-PRF to a 1:1 mixture of CTLs and EL4 cells, as assessed by flow cytometry.”**

- a.)** Gating strategy to assess cells of the same size: During analysis, the viable cell morphology gate is first set using an EL4 control, before being transferred to the CTL control and trimmed to include only viable CTLs. This optimised gate that includes only viable cells that are present in both EL4 and CTL populations is then applied to the experimental samples that contain a 1:1 mixture of EL4s and CTLs
- b.)** From this morphology gate, the clearly distinct CD8<sup>-</sup> and CD8<sup>+</sup> populations (stained with anti-CD8-allophycocyanin (APC)) within the 1:1 mixture are gated for (using single cell type controls) and their Geometric Mean Fluorescence values calculated.
- c.)** “Average GFP geometric mean fluorescence intensity (MFI) of CD8<sup>-</sup> and CD8<sup>+</sup> gates plotted as a function of TMH-GFP-PRF concentration. Each data point represents a mean ( $\pm$  s.e.m.) of 3 independent experiments. Curves represent Michaelis-Menten fits to the data.”

### 3.4 Discussion

A comprehensive series of experiments that investigated the putative role of LAMP-1 in cytotoxic lymphocyte self-protection showed unequivocally that cells expressing over two-orders of magnitude higher level of LAMP-1 than control cells had gained no protection from purified recombinant perforin lysis or cytotoxic lymphocyte mediated killing. This finding disputes the previously proposed role of LAMP-1 in cytotoxic lymphocyte self-protection (Cohnen et al., 2013), leaving the question of what protects a cytotoxic lymphocyte during immune synapse formation unanswered. However, it became apparent during the investigation of LAMP-1, that cytotoxic lymphocytes (both, CTL and NK cells) are far more resistant to perforin (over two orders of magnitude) than their targets. This was subsequently confirmed by a direct comparison of these cell types, and the observed difference found to hold true for both murine CTLs and murine NK cells, relative to two common murine target cell lines, EL4 and P815.

After confirming the extraordinary resistance of primary cytotoxic lymphocytes to purified perforin, a novel GFP tagged TMH1-locked version of recombinant perforin allowed the comparative analysis of perforin binding levels between effector and target cells. Previous attempts to analyse perforin binding levels of cells have relied on in-direct competition assays (S. Jiang et al., 1990) or have been affected by experimental artefacts owing to the difficulty of distinguishing perforin binding and lysis when using perforin antibodies with flow cytometry (Lehmann et al., 2000; Sunil S. Metkar et al., 2001). In our system however, the non-lytic GFP fusion of TMH locked perforin allows a direct measurement of perforin binding without any compounding effects of cell lysis. Crucially, perforin binding levels are compared only between cells gated for the same morphology, ensuring no artefacts are encountered due to the available cell surface area for perforin binding. The ability to treat both cell types with perforin simultaneously ensured their exposure to identical perforin-binding conditions.

The observed difference in perforin binding to CD8<sup>-</sup> (EL4) and CD8<sup>+</sup> (CTL) cells suggests that reduced perforin binding is a substantial, but clearly not an exclusive factor in a cytotoxic lymphocyte's ability to resist perforin lysis. That the cytotoxic lymphocyte membrane can interfere with perforin binding is intriguing, as "perforin does not require partner proteins for its membrane binding and pore formation" and it also has no known inhibitors in the CTL membrane (Baran et al., 2006). One explanation however could lie within the hypothesis that CTL plasma membranes are more resistant to perforin binding and pore formation due to their lipid spacing (Antia et al., 1992). Although a direct correlation between plasma membrane lipid spacing and perforin resistance was shown to not hold for all cell lines at the time (Ojcius et al., 1990), these studies were both performed using what are now somewhat outdated techniques. Interestingly, studies using artificial membranes and measuring pore formation indirectly by detecting changes in conductance across the membrane found that small incomplete pores were able to form more readily on a disordered membrane whilst full pores were less readily formed but appeared to be more stable on an ordered membrane (Praper et al., 2011). The obvious limitation of this study was the use of artificial membranes systems in place of living cell membranes and the indirect measurement of pore formation by conductance. The overall concept of membrane order affecting

perforin function is further supported by observations made with other pore-forming toxins (Rojko & Anderluh, 2015). With the availability of recombinant perforin, newly designed probes for membrane order, as well as biochemical agents for specifically disrupting membrane order, we next decided to examine the role of lipid composition, specifically lipid spacing (order), on cytotoxic lymphocyte resistance to perforin.



## Chapter 4 High lipid order protects the plasma membrane from perforin binding

### 4.1 Introduction

#### 4.1.1 Lipids in Cellular Membranes

Lipids are molecules which are soluble in organic solvents but insoluble in water. They provide a crucial unit of energy storage for cells, as well as functioning in the structure of the cell by contribution to plasma and internal organelle membranes. Lipids are amphipathic, containing both a polar hydrophilic head group and a non-polar hydrophobic tail. It is this special property that allows lipid bilayers to form, where the hydrophobic tails interact to shield themselves from water, exposing the hydrophilic head groups on either side of the bilayer (Figure 4.1). Hydrophobic forces encourage lipid bilayer formation and this enables cells to use them as barriers between themselves and their environment. Many proteins reside in the membranes of cells, creating a complex interplay.

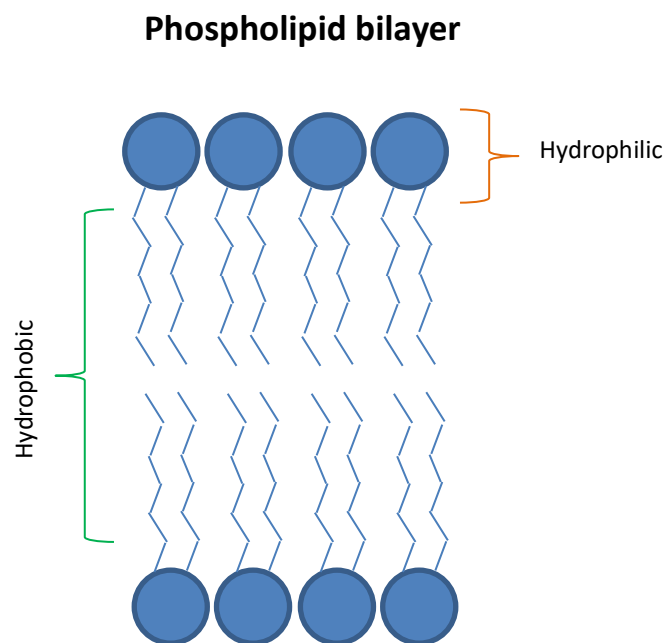


**Figure 4.1: Basic structure of the phospholipid bilayer.**

Hydrophobic forces result in phospholipid bilayer formation, where the hydrophobic tails of separate phospholipids interact together, shielded from water by their hydrophilic heads that orientate to the outside of the layer.

There are three main classes of lipid which contribute to plasma membranes in mammalian cells. Glycerophospholipids are the most common, generally consisting of a glycerol backbone with two long carbon chain tails and one phosphate group. One of the OH- groups on the phosphate is generally esterified to another component, and the identity of this component distinguishes the glycerophospholipid. For example, if the component is choline, the glycerophospholipid becomes phosphatidylcholine (PC) (Figure 4.2a). When the component is serine, the glycerophospholipid becomes phosphatidylserine (PS) (Figure 4.2b) (Blanco & Blanco, 2017). Phosphatidylethanolamine (PE) is another common glycerophospholipid found in cellular membranes, however in this study we focus on PC and PS, and PE will not be further discussed in the scope of this thesis.

As a second group, sphingolipids consist of a sphingosine backbone, a fatty acid tail and a phosphate group with choline attached. One of the most predominant forms of sphingolipid found in mammalian cells is sphingomyelin (SM) (Figure 4.2c) (van Meer et al., 2008). Numerous forms of SM exist with variations in length and saturation of the fatty acid tail.

The third main group of lipids relevant to the study of mammalian plasma membranes are the sterols, which consist of a hydrophobic tail, a rigid sterol backbone consisting of four carbon rings, and a hydrophilic OH- headgroup. The most relevant sterol to this study is cholesterol (Figure 4.2d).

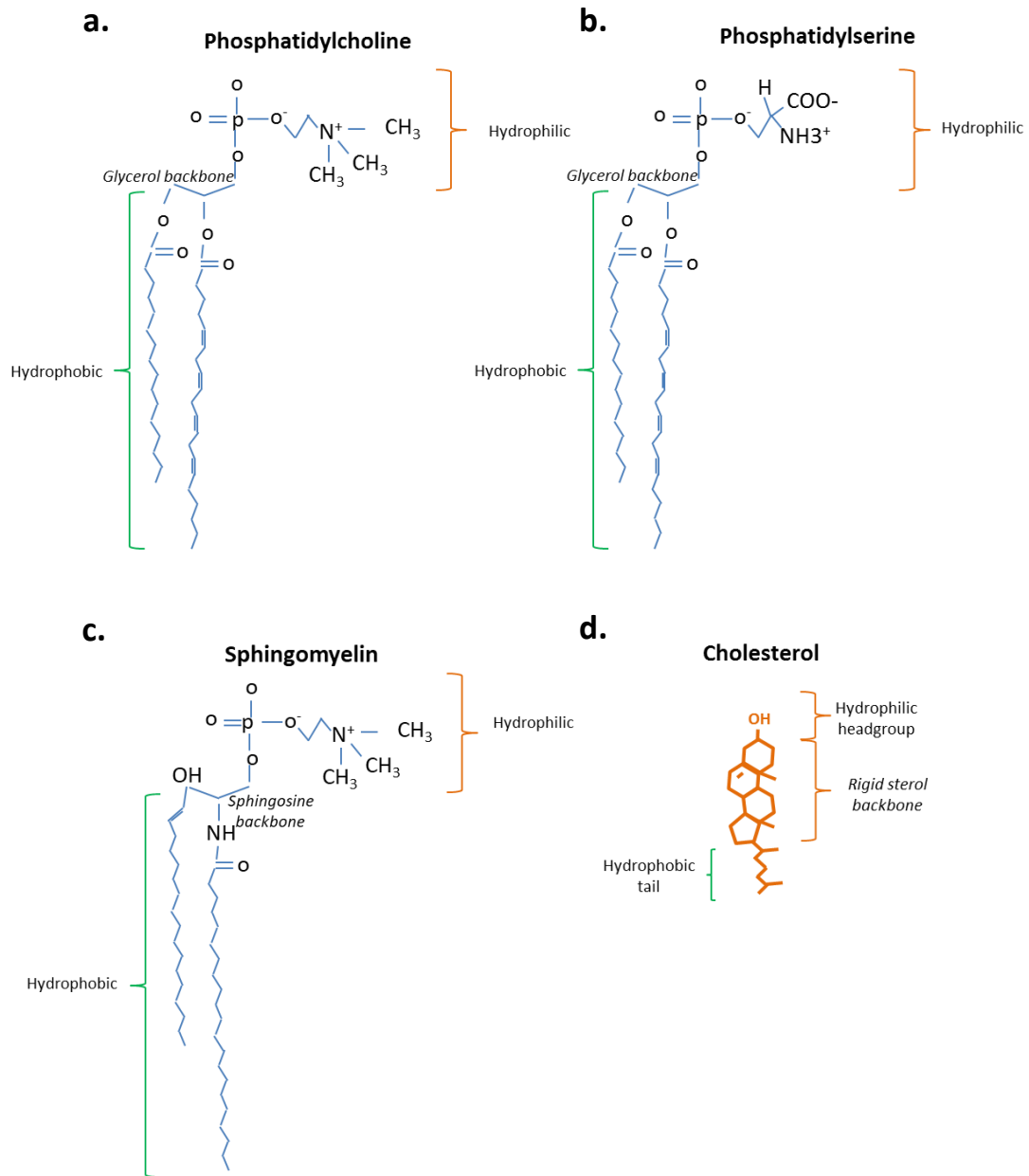


**Figure 4.2: Structural comparison of the three main components of cellular membranes; glycerophospholipids, sterols and sphingolipids.**

Shown are the most common forms found in cellular membranes that are utilised in this study: phosphatidylcholine, phosphatidylserine, cholesterol and sphingomyelin.

#### 4.1.2 Cholesterol and membrane order

Since cholesterol is smaller than both glycerophospholipids and sphingolipids, it can occupy the space between them and thus impose membrane order. In this way, regions of membrane which are initially in a liquid disordered phase can be transformed into liquid ordered phase by increasing the cholesterol content (Figure 4.3). It is of note that cholesterol can also transform a solid ordered lipid phase back towards the liquid ordered phase (van Meer et al., 2008). Variation in the lateral packing of lipids between liquid disordered and liquid ordered membranes results in a height difference of approximately 1nm (Das et al., 2010).

The melting temperature of lipid types is another crucial determinate of membrane order at a given temperature. In this study, to represent liquid ordered and disordered systems, we use ternary lipid mixtures of PC, SM and cholesterol. The type of PC used (DOPC) has a melting point of -17 °C and therefore constitutes the liquid disordered phase at 37 °C, while egg SM sequesters with cholesterol to form liquid ordered domains.

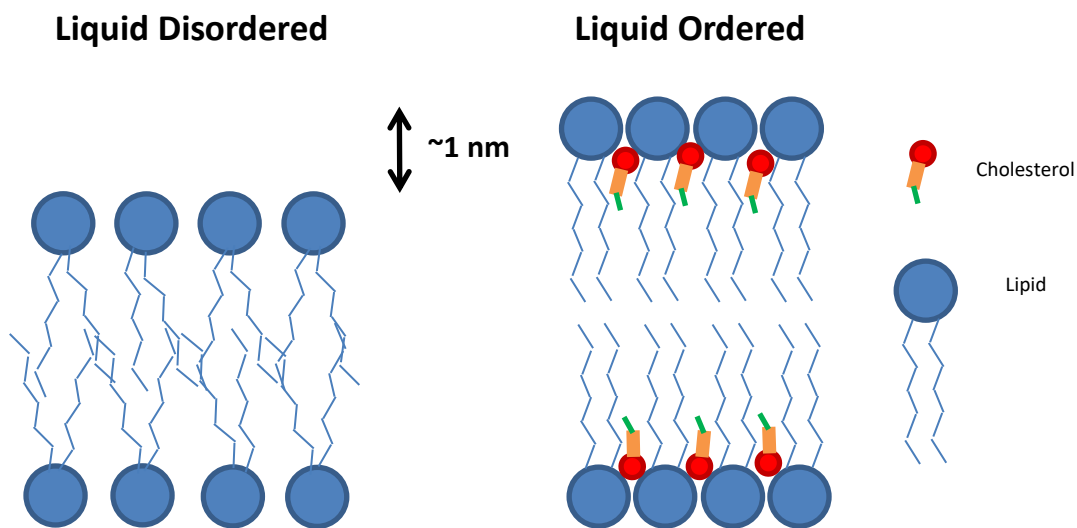


**Figure 4.3: Schematic diagram showing the difference in lipid packing between liquid disordered and liquid ordered membrane phases.**

The close packing of lipids in regions of ordered membrane results in their hydrophobic tails adopting a more elongated arrangement, compared to that of a disordered membrane. The incorporation of cholesterol into a disordered membrane can increase membrane order, with cholesterol occupying the space between lipids as shown above. *Image adapted from (Metzler et al., 2016).*

#### 4.1.3 Modification of membrane order using 7-Ketocholesterol (7KC)

Cholesterol plays a crucial role in determining membrane order (van Meer et al., 2008). However, by incorporating a form of cholesterol (7KC) that contains a ketone group sidechain, plasma membranes can be made more disordered, due to the steric hindrance of the ketone group maintaining space between phospholipids (Massey & Pownall, 2005) (Figure 4.4). This technique of incorporating 7KC into plasma membranes to alter membrane order has been used widely in the field of membrane biology (Owen et al., 2010; Rentero et al., 2008) and involves the incorporation of Methyl  $\beta$ -cyclodextran (M $\beta$ CD)/7KC complexes into the plasma membrane, increasing the overall level of sterol in the membrane (Rentero et al., 2008), but reducing the membrane order. The experiments can be controlled by incorporating unmodified cholesterol under the same conditions, to specifically study the impact of membrane disorder due to the incorporation of 7KC.

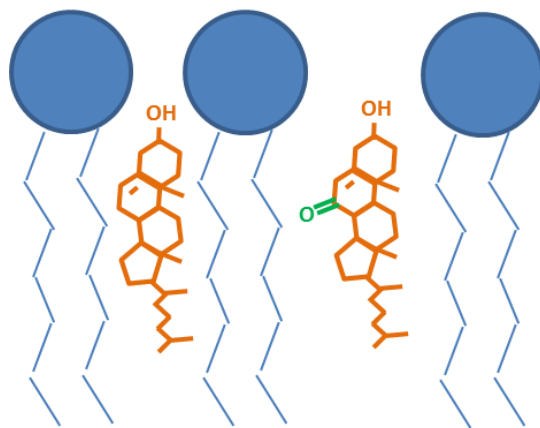


**Figure 4.4: Incorporation of 7KC into plasma membranes increases spacing between lipids.**

Schematic diagram showing the extra ketone group (green) extending from the cholesterol body (orange) creating spacing between phospholipids (blue) in the plasma membrane. *Image adapted from (Massey & Pownall, 2005)*

#### 4.1.4 Laurdan as a probe of membrane order

Development of the membrane dye 6-Dodecanoyl-2-dimethylaminonaphthalene (Laurdan), has allowed the visualisation and quantitation of lipid order in whole cells (Owen et al., 2012). Laurdan incorporates into membranes and aligns with the hydrophobic tails of the phospholipids (Gaus et al., 2006) (Figure 4.5a). Laurdan reports on the amount of water which is able to penetrate the membrane, which is increased in loosely packed disordered membranes (Bagatoll et al., 1999; Bagatolli et al., 1998). Water penetration results in close proximity of polar water molecules to Laurdan, whose emission spectrum is solvent polarity dependent (Gaus et al., 2006), therefore a longer wavelength emission is observed when Laurdan is located in disordered membranes (Figure 4.5b). In this way a ratio of the fluorescence from the ordered and disordered regions of emission can be used to determine the lipid order.

Visualising lipid rafts has previously relied heavily on the staining of cells for proteins which are known to generally localise in lipid raft fractions, such as fluorescently labelled cholera toxin B subunit (CTxB) which binds to the raft associated ganglioside monosialotetrahexosylganglioside (GM1). In such a system, it is assumed that the presence of GM1 indicates a lipid raft phase and, therefore, high lipid order. In contrast, Laurdan provides a direct measurement of lipid order, and also avoids the potential cross linking of rafts which is associated with use of CTxB (Hammond et al., 2005). Using both Laurdan (Gaus et al., 2005), and other similar solvent polarity sensitive dyes (Owen et al., 2010), an increase of order at the pre synaptic membrane during synapse formation of CD4<sup>+</sup> T cells has been demonstrated. This correlates with the previously observed accumulation of lipid raft markers at the pre synaptic membrane (Tavano et al., 2004; Viola et al., 1999).

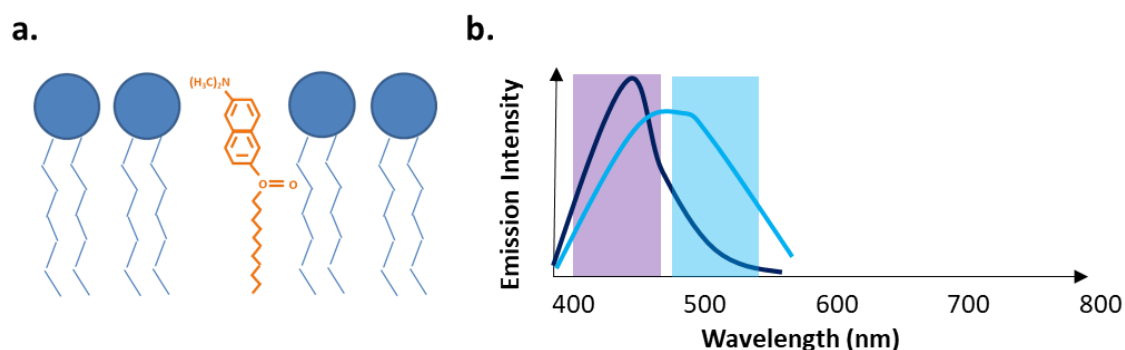


**Figure 4.5: Laurdan excitation/emission spectrum.**

**a.)** Laurdan (orange) aligns with the hydrophobic tails of phospholipids (blue), regardless of their headgroup. *Diagram adapted from (Gaus et al., 2006)*

**b.)** Laurdan is excited by 400nm wavelength and emits predominantly in the range of 440nm (Purple shading) when located in ordered membrane or 490nm (blue shading) when located in disordered membrane. *Diagram adapted from (Owen et al., 2012)*

Laurdan Fluorescence has two major peaks,  $\lambda_{em} \sim 440\text{nm}$  (ordered) and  $\lambda_{em} \sim 490\text{nm}$  (disordered) (Figure 4.8); the ratio of fluorescence intensity from these two regions is used to assess membrane order. To obtain this ratio, emission intensity (following excitation at 405nm) is collected every 8.9nm, from 410nm to 695nm; then the two regions of interest, those centred on 450nm and 490nm, are used to calculate the ratio. A schematic diagram of lambda stack collection using Laurdan is shown in Figure 4.6.

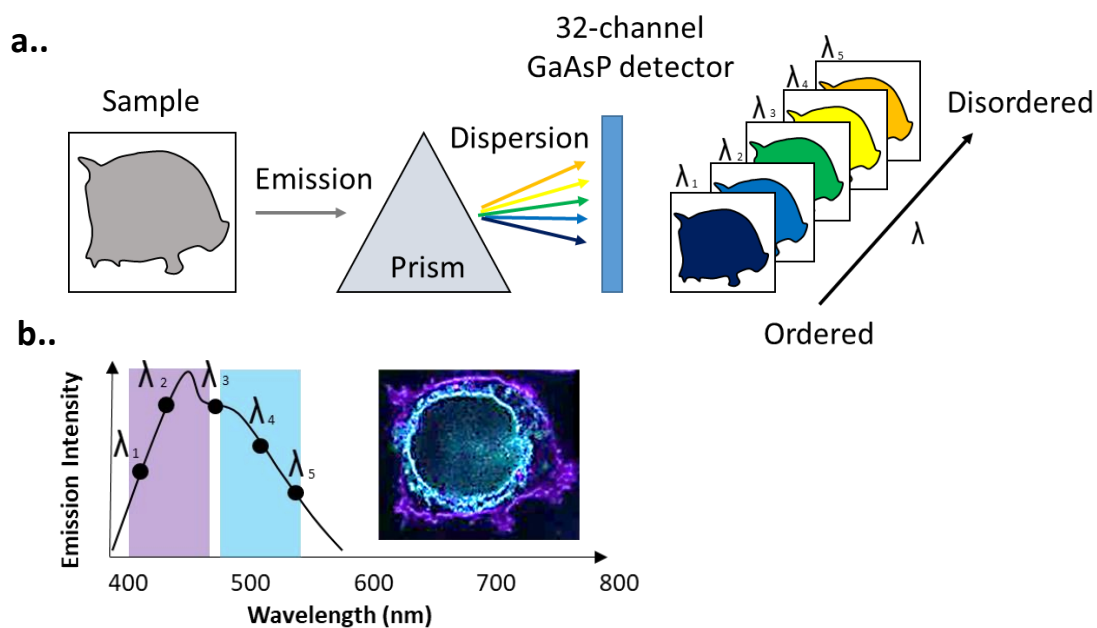


**Figure 4.6: Schematic diagram detailing the collection of a lambda stack using laurdan.**

**a.)** Sample emission (following excitation at 400nm) is passed through a prism which disperses the light into 8.9nm wavelength increments (apparent size of wavelength sections in figure is increased for visualisation purposes).

**b.)** The level of fluorescence in each of these channels informs the level of membrane order. A representative image of a lambda image of a CTL is provided as an inset. For analysis using the MATLAB 'spectral imaging toolbox) the peaks centred in the ordered and disordered regions (in this example,  $\lambda_2$  and  $\lambda_4$ ) are used to calculate the GP ratio.

\*Image in Figure 4.6b has had brightness/contrast/sharpness adjusted for display purposes\* *Image adapted from (Sezgin et al., 2015)*

## **4.2 Materials and Methods**

### **4.2.1 AFM**

For details of AFM imaging, please refer to the concise summary provided in *2.5 Atomic Force Microscopy*, and the detailed AFM methods provided in Appendix 1.

### **4.2.2 7KC loading**

“Cholesterol or 7-ketocholesterol (7KC) (both Sigma Aldrich, Missouri, USA) were dissolved in 100% ethanol at 15 mg/mL and mixed at different ratios. Cholesterol/7KC mixtures (as well as 100% cholesterol or 100% 7KC) were added drop-wise over a period of 30 min, to a solution of 50 mg/mL methyl- $\beta$ -cyclodextran (MBCD, Sigma Aldrich, Missouri, USA) in PBS, which was heated to 80 °C, to achieve the final sterol stock concentration of 1.5 mg/mL (Rentero et al., 2008). Cells were washed 3 times in 0.1% BSA RPMI-1640 (GIBCO, Paisley, UK) before being resuspended at  $0.5 \times 10^6$ /mL. Up to 2.25  $\mu$ l of cholesterol/7KC stock solutions in MBCD were then added to 1 mL of cells; the cells were incubated at 37 °C for 30 min, the washed 3 times in 0.1% BSA DMEM, resuspended at  $10^6$ /mL and immediately used for the desired experiment.”

### **4.2.3 Osmosis Assay**

To test for non-specific sensitisation of 7KC treated cells, an experiment was designed to assess the osmotic sensitivity of treated and untreated cells. Cells were first labelled with  $^{51}\text{Cr}$  (see *2.4.1  $^{51}\text{Cr}$  release assay*), washed and loaded with 7KC/Chol mixture. These cells were then serially diluted in solutions containing various ratios of RPMI (containing 110mM NaCl) and H<sub>2</sub>O, from 100:0 to 0:100. In this way the salt concentration was serially diluted, progressively decreasing the osmolality of the solution. These cells were incubated for 4 hours at 37 degrees, 5% CO<sub>2</sub>. Supernatant was harvested and cell lysis measured as % specific  $^{51}\text{Cr}$  release.

### **4.2.4 Laurdan Microscopy**

“Cells were incubated in 0.1% BSA DMEM supplemented with 5 $\mu$ M Laurdan (Molecular Probes, Oregon, USA) in DMSO for one hour. Cells were then pelleted and resuspended in 250 $\mu$ l serum-free DMEM before being plated out in 8-well Nunc Lab-Tek II #1.5H glass bottom chamber wells (ThermoFisher Scientific, Massachusetts, USA). After allowing the cells to adhere for 20 min at 37°C, 50  $\mu$ l of 0.5% BSA solution was added to maintain cell viability during imaging. Lambda stacks were recorded using a Zeiss Elyra PS.1 microscope with a Tokai Hit stage/objective heater attached, and 5% CO<sub>2</sub>/humidity maintained (Zeiss, Oberkochen, Germany). An optical zoom of 2 was applied to a Plan-Aporchromat 63X / 1.4 Oil DIC lens (Zeiss, Oberkochen, Germany) and images were obtained every 8.9 nm from 410 nm – 695 nm using a line average of 16.”



“Recorded lambda stacks were exported to the Spectral Imaging Toolbox in Matlab (Aron et al., 2017), where the data was segmented to isolate the Laurdan signal from the plasma membranes of individual cells and the generalized polarization (GP) of the plasma membrane calculated. Images of a reference solution (Laurdan in DMSO) were obtained with the same microscope settings as used for the imaging of cells, and a reference value ( $GP_{ref}$ ) of 0.207 was used for Laurdan, as obtained per (Owen et al., 2012). For detailed description of GP calculation using the Spectral Imaging Toolbox, see Ref. (Aron et al., 2017), however the basic principle for membrane order GP calculation is described in equation 1.”

$$GP = \frac{I_{order} - GI_{disorder}}{I_{order} + GI_{disorder}}$$

**Equation 1: Calculation of GP value.** Equation adapted from (Owen et al., 2012), where  $I_{order}$  = intensity of signal within the ordered region,  $I_{disorder}$  = intensity of signal within the disordered region,  $G$  = calibration factor, determined by relative background fluorescence of the solution in each emission region in the absence of cells.

## 4.3 Results

### 4.3.1 Lipid bilayer regions containing high levels of sphingomyelin and cholesterol are refractory to perforin binding and pore formation

*The experiments described in this section (4.3.1) were designed and performed by Dr Adrian Hodel and are included to provide context to the study.*

To determine the role of plasma membrane lipid order on perforin binding and cytotoxicity, experiments were designed to compare perforin binding and pore formation on membranes in which lipid order was systematically varied. A ternary mixture of cholesterol, sphingomyelin (SM) and (liquid-phase) phosphatidylcholine (PC) is a commonly used biophysical model of the plasma membrane. By modifying the ratio of its components, it has been successfully applied for assessing the behaviour of membranes with different lipid order (Connell et al., 2013; Simons & Vaz, 2004; Veatch & Keller, 2005). In phase-separated membranes, atomic force microscopy provided sufficient resolution to distinguish regions of high and low membrane order due to their 0.5-1nm differences in height (as demonstrated schematically in Figure 4.3). Perforin was then added to these membranes, allowing perforin binding and pore formation to be assessed by AFM imaging (*see Appendix 1*).

A surprisingly explicit result was observed, with WT-PRF showing a clear preference for pore formation on disordered membranes with high concentrations of DOPC. At the same time, no WT-PRF pores were formed on highly ordered membranes that contained high concentrations of SM and Chol (Figure 4.7).

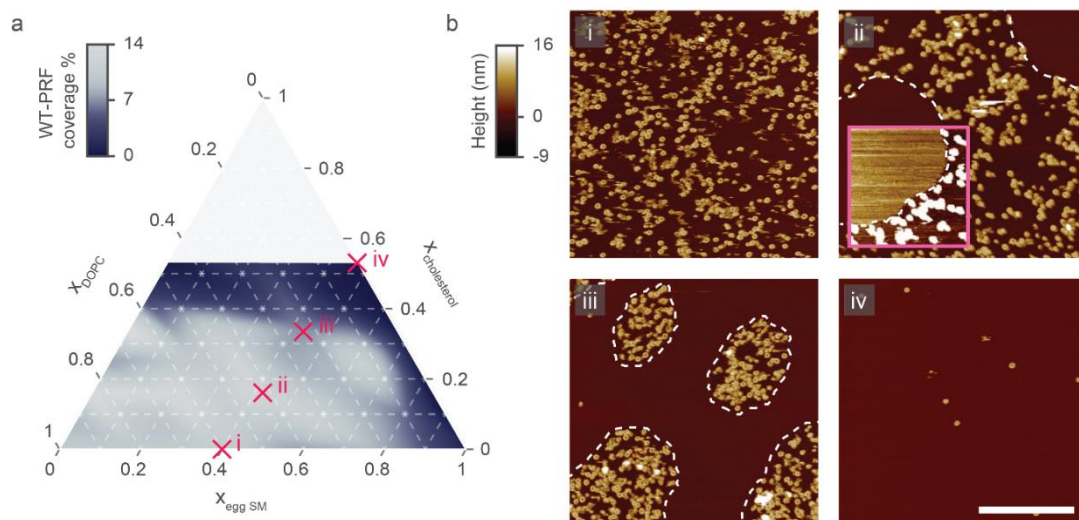


**Figure 4.7: “Lipid order protects synthetic membranes from perforin pore formation.**

**a.)** Perforin coverage (as % of membrane surface) after incubation of supported DOPC/egg SM/cholesterol bilayers with 150 nM WT-PRF, as a function of the molar fractions ( $x$ ) for the constituents of the bilayer (total = 1).

**b.)** AFM images of perforin pores on supported lipid bilayers of the compositions labelled in a. AFM samples were incubated and imaged at 37 °C. Dashed lines highlight phase boundaries in the lipid membrane. For the area marked by a pink square in the top right image, the colour scale has been saturated (4 nm instead of 25 nm full range) to more clearly identify the enhanced thickness (height) of a liquid-ordered domain and the absence of perforin pores (white at this scale) on such domains.”

Having determined a preference of WT-PRF pore formation on disordered membranes, it was necessary to determine if this was a consequence of increased perforin binding (the first step of perforin pore formation), or more efficient pore formation. To test this, a non-lytic mutant of perforin (TMH1-PRF) was utilised as it allows the analysis of perforin binding independently from insertion and pore formation. As before (Figure 3.8), DTT was used to unlock the lipid bilayer bound TMH1-PRF.

Lipid bilayers of varying membrane order were generated by altering the proportion of PC, SM and cholesterol in the ternary mixture, as shown by the 0.5-1nm difference in height between ordered and disordered domains (Figure 4.8a.i.). Upon addition of the locked TMH1-PRF, the height trace increased by around 11nm (height of perforin prepores) within the disordered region, but remained the same in the ordered region (Figure 4.8a.ii). This showed that perforin was able to bind only to the disordered region of the membrane. Upon the addition of DTT, the TMH1-PRF mutant was unlocked and the bound perforin completed the transition from pre-pore to pore (Figure 4.8 a.iii., b.). As expected, pores were seen only on the disordered region, confirming that perforin bound to the disordered membrane domains remained fully functional and did not translocate into ordered regions.

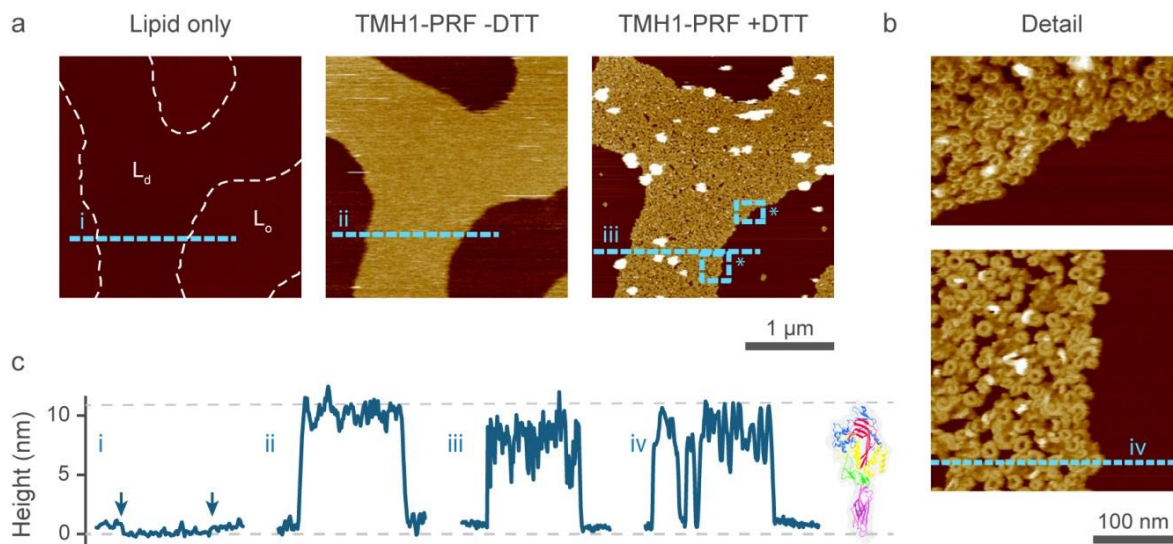


**Figure 4.8: “Prepore-locked TMH1-PRF binds to disordered domains on phase separated lipid membranes.**

**a.)** AFM images of an approximately equimolar DOPC/egg SM/cholesterol supported lipid bilayer, showing phase separation between liquid-disordered ( $L_d$ ) and liquid ordered ( $L_o$ ) domains, with the  $L_o$  phase appearing higher (thicker) than the  $L_d$  phase in the “lipid only” image. The phase boundaries are highlighted by dashed white lines. Prepore-locked perforin (TMH1-PRF -DTT) appears as diffuse plateaus due to its mobile nature (Leung et al., 2017), exclusively bound to the  $L_d$  domains. Upon exposure to DTT, these mobile prepores transform into static pores (TMH1-PRF +DTT).

**b.)** Higher-magnification images of the areas indicated by the dashed blue rectangles in **a**. The  $L_d$  domain shows a dense coverage of arc- and ring-shaped pores, whereas the  $L_o$  domains remains empty.

**c.)** Height profiles as recorded along the blue, dashed lines in the AFM images in **a** and **b**. The phase separation on the empty membrane (i) is visible as a 0.5-1 nm height difference, and the phase boundaries are indicated by vertical arrows. Addition of TMH1-PRF (-DTT/+DTT, ii-iv) leads to the formation of ca. 11 nm high features, corresponding to the height of perforin prepores and pores (Law et al., 2010; Leung et al., 2017; S. S. Metkar et al., 2015). Grey, dashed lines indicate the height of the membrane (0 nm) and of a perforin monomer (11 nm (Law et al., 2010)). The differences in measured perforin height between traces ii, iii and iv are attributed to variations in the applied forces in the AFM experiments. The sample was incubated and imaged at 37°C. Colour (height) scale as in Figure 4.7b.”

Having demonstrated the phospholipid specificity of perforin binding in synthetic lipid bilayers, the next step was to investigate the effect of membrane order in intact cells. To achieve this, different experimental techniques were required. The plasma membrane of cells is a complex mixture of proteins and lipids, arranged in a far less uniform 3-dimensional orientation than the planar bilayers required for high resolution AFM. In the following experiments performed on live cells, Laurdan provided a useful tool for assessing membrane order in live cells, whilst the introduction of an oxidised form of cholesterol (7KC) into plasma membranes of live cells allowed us to vary membrane order.

#### 4.3.2 Anarchy via 7KC: treatment of CTLs with 7KC results in disordered plasma membrane

To determine the maximum concentration of sterol/M $\beta$ CD which could be used without affecting cell viability, CTLs were loaded with increasing concentrations of sterol/M $\beta$ CD and their viability was analysed using cell-impermeable nucleic acid dye Propidium Iodide. It was found that 2.25 $\mu$ l/ml of sterol/M $\beta$ CD was the maximum tolerated concentration of sterol/M $\beta$ CD, as there was no increase in CTL death compared to untreated control at this concentration (Figure 4.9).

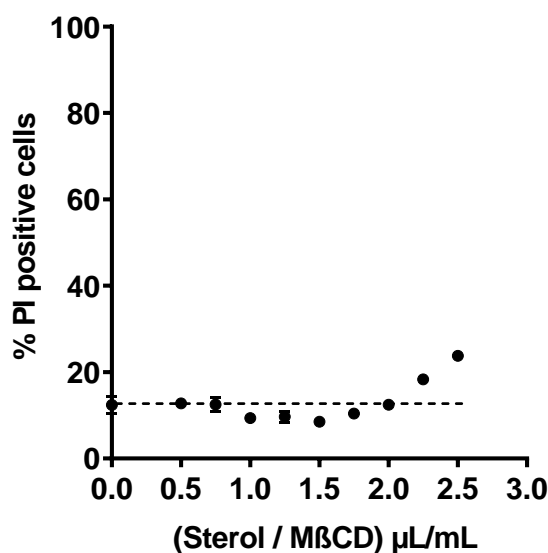


**Figure 4.9:** “Determination of a non-cytotoxic concentration of sterol/ M $\beta$ CD.

CTLs were treated with increasing amounts of a sterol mix of 75% 7KC and 25% cholesterol in methyl- $\beta$ -cyclodextrin (M $\beta$ CD). As assessed by propidium iodide (PI) staining, cell death only rises above background levels at close to the maximum concentration of 2.5  $\mu$ L (sterol/ M $\beta$ CD) per mL for a cell suspension containing  $5 \times 10^5$  cells in 1ml. 2.25  $\mu$ L (sterol/ M $\beta$ CD) per mL cells was selected as the optimal concentration and used for all cholesterol loading experiments. Each data point represents a mean ( $\pm$  s.e.m.) of 3 independent experiments and dotted line shows level of background cell death without addition of Sterol/ M $\beta$ CD.”

Perforin pore formation leads to osmotic stress; therefore, prior to assessing the effect of 7KC on perforin sensitivity, the effect of 7KC treatment on osmotic sensitivity of cells needed to be determined. By incubating 7KC treated and untreated cells in buffers with varying osmolarity, we found no difference in the levels of cell lysis of untreated, M $\beta$ CD only control and the 7KC/M $\beta$ CD treated cells (Figure 4.10). This observation ruled out a role for 7KC/M $\beta$ CD in direct lysis of the treated cells.

The experiment shown in Figure 4.10 was completed by Ms. Tahereh Noori and is included for completeness of the study.

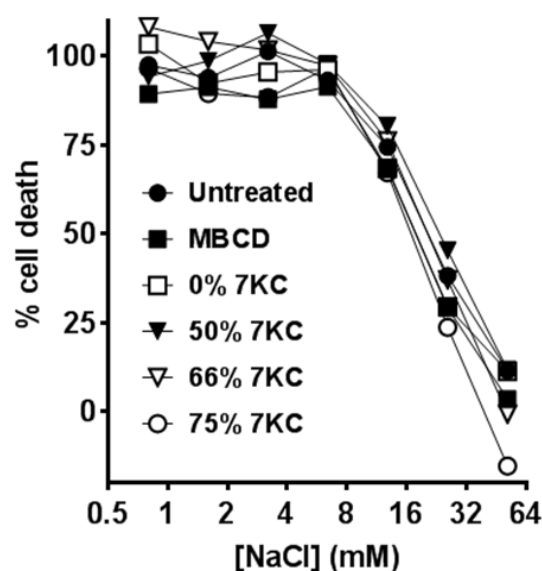


Figure 4.10: “7KC treatment of CTLs does not sensitise cells to osmotic stress.

<sup>51</sup>Cr loaded CTLs were treated with varying ratios of 7KC/cholesterol and then incubated in solutions containing different concentrations of NaCl. 7KC and cholesterol loading did not change the susceptibility of cells to osmotic stress compared to untreated cells. Each data point represents a mean of 2 independent experiments, both of which contained 3 technical replicates. For clarity, data points are shown connected by lines.”

Previous studies have used 7KC loading to decrease membrane order in primary human CD4<sup>+</sup> T cells (Miguel et al., 2011), primary murine CD4<sup>+</sup> T cells (Rentero et al., 2008) and Jurkat cells (Owen et al., 2010). However, this has not been performed on activated murine CTLs. Therefore, the ability of 7KC to decrease membrane order of activated murine CTL's, needed to be confirmed. In order to do this, MβCD and 7KC/MβCD treated CTLs were labelled with Laurdan for 1 hour prior to imaging, allowing the dye to equilibrate between the plasma membrane and internal membranes. As Laurdan does stain both the plasma membrane and the internal cellular membranes (which are known to have substantially lower order (Owen et al., 2012)), it was necessary to perform a segmentation analysis that would assure specific measurement at the plasma membrane when analysing the collected lambda images. This was performed using the MATLAB extension ‘Spectral Imaging Toolbox’ (Aron et al., 2017). Objects were first segmented, before plasma membrane segmentation and subsequent GP calculation was performed (Figure 4.11).

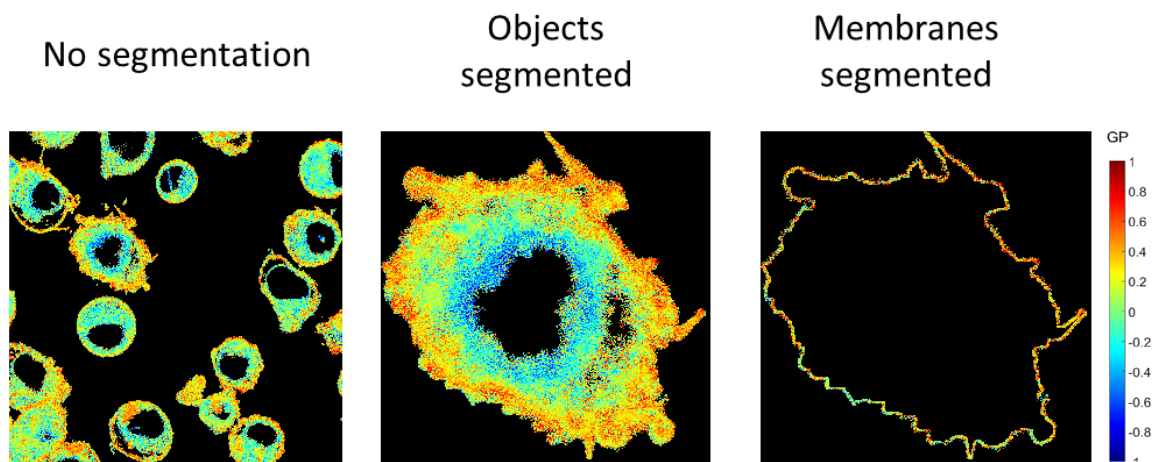


Figure 4.11: Representative example of object and plasma membrane segmentation using the MATLAB extension ‘Spectral Imaging Toolbox’ (Aron et al., 2017).

- a.) Field of view containing multiple cells prior to segmentation.
- b.) Individual object obtained after object segmentation.
- c.) Plasma membrane obtained after membrane segmentation. Colour scale indicates GP value, note the presence of lower order of internal membrane structures prior to membrane segmentation.

To ensure that any reduction in membrane order was due to the 7KC added to the cells, intact and M $\beta$ CD-treated cells, as well as cells treated with 100% Cholesterol (0% 7KC), were assessed for their GP value (Equation 1, Materials and Methods 4.2.4). The GP value did not vary significantly in cells treated with either M $\beta$ CD or 100% Cholesterol; However, A significant decrease ( $p < 0.01$ ) in GP value was observed between untreated cells and those treated with 25%-100% 7KC (Figure 4.12), with the difference being more pronounced with higher concentrations of 7KC.

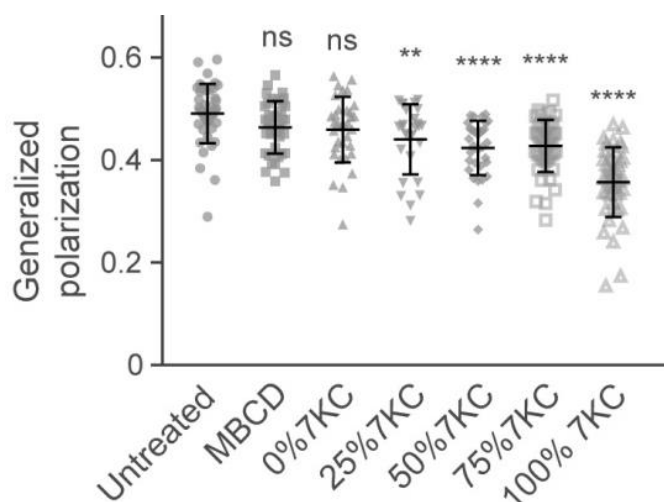


Figure 4.12: “Generalised Polarisation (GP) values of CTL decrease following the incorporation of increasing ratios of 7KC:cholesterol.

As the ratio of 7KC:cholesterol is increased, the measured GP value of CTL decreases, indicating reduced lipid order. Data points represent individual cells, as measured in three independent experiments; statistical significance with respect to the “untreated” control was assessed using ANOVA with Dunnett’s post-hoc analysis, where ‘ns’ - not significant, \*\* $p < 0.01$ , \*\*\*\* $p < 0.0001$ .”

### 4.3.3 A weakened shield: reduced plasma membrane order increases the sensitivity of CTLs to perforin.

Sections (4.3.3 and 4.3.4) were completed with the technical assistance of Ms. Tahereh Noori. After I designed and optimised the experiments, she performed independent replicates and collated the data. I finalised all data presentation and calculated the fold difference values detailed in Fig 4.14b.

With the effect of 7KC on murine CTLs known, it was now possible to assess the perforin sensitivity of 7KC treated CTLs. Cells were treated with 7KC/Chol mixtures exactly as in the experiments performed to assess membrane order (Figure 4.12), and were then exposed to either TMH1-GFP-PRF (to assess plasma membrane binding of perforin) or WT-PRF (to assess perforin sensitivity of the cells). We found a positive dose-dependent relationship between increasing concentrations of 7KC (reduced membrane order) and TMH1-PRF-GFP binding to the cells (Figure 4.13).

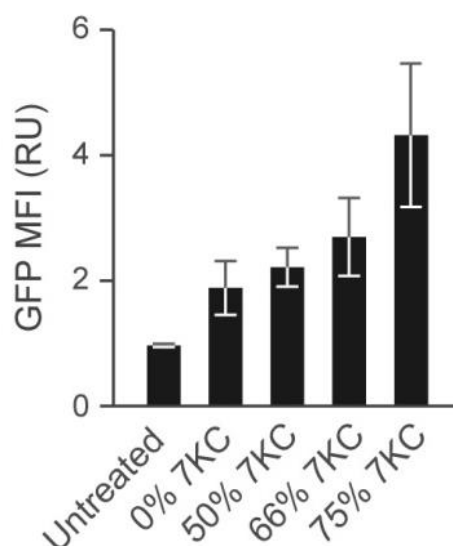


**Figure 4.13: “Reduced membrane order of 7KC-treated CTLs sensitises the cells to TMH1-GFP-PRF binding.**

The GFP MFI of cells which had been exposed to TMH1-GFP-PRF at 37 °C was measured by flow cytometry and normalized to the MFI of untreated cells. The data represent mean ( $\pm$  s.e.m.) of 3 independent experiments.”



To test the functional consequence of increased perforin binding due to reduced membrane order, a flow cytometry experiment was designed in which WT-PRF was used instead of the non-lytic TMH1-GFP-PRF. Control and 7KC-treated EL4 cells or CTLs were incubated with various concentrations of WT-PRF for 1.5 hours at 37 degrees, and cell death was measured by propidium iodide fluorescence. We found that conditions that resulted in reduced membrane order sensitised CTLs to perforin lysis (Figure 4.14a). In accord with previous experiments (Figure 3.10), lysis of untreated CTLs required much higher concentrations of WT-PRF compared to the concentration required to lyse untreated EL4 cells. Interestingly, EL4 target cells were also slightly sensitised to perforin by 7KC treatment, but to a far lesser extent to CTLs. Furthermore, at the highest concentration of 7KC, CTL perforin sensitivity approached that of untreated EL4 target cells. By plotting the concentration of perforin required to lyse 50% of cells against 7KC concentration, we found the magnitude of sensitisation of CTLs was 2.4-fold higher than that of EL4 cells (Figure 4.14b). This value was calculated by dividing the concentration of perforin required for 50% lysis at 0:100 7KC:cholesterol ratio by the concentration of perforin required for 50% lysis at 75:25 7KC:cholesterol ratio.

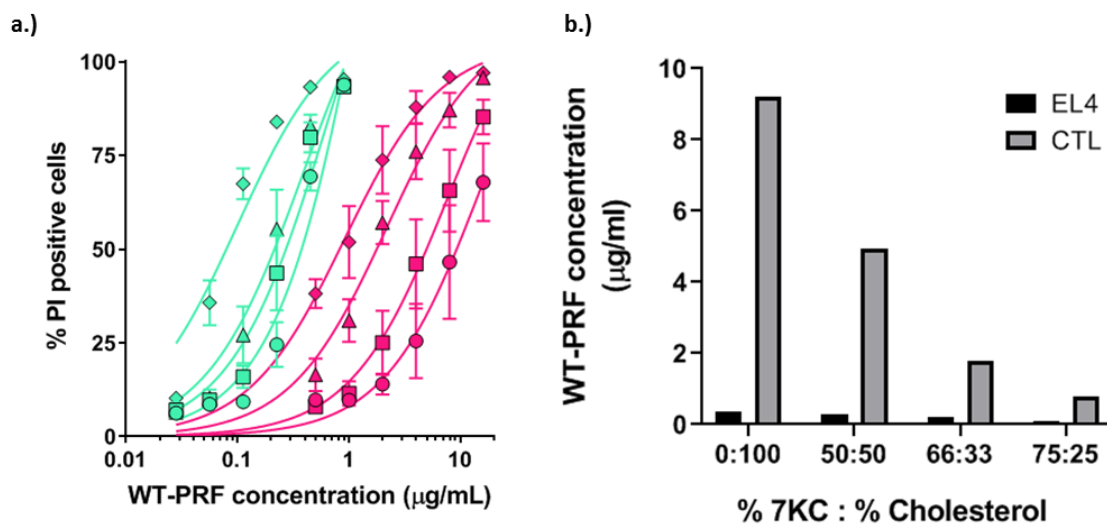


**Figure 4.14: “Reduced membrane order of 7KC-treated CTLs and EL4s sensitises the cells to WT-PRF lysis.**

**a.)** The reduced membrane order of 7KC-treated CTLs (red) and EL4 cells (green) sensitizes the cells to WT-PRF lysis, as determined by propidium iodide (PI) staining of untreated cells (○) and cells loaded with 50% (□), 66% (△), and 75% (◇) 7KC/cholesterol. Each data point represents a mean ( $\pm$  s.e.m.) of 3 independent experiments. Curves represent Michaelis-Menten fits to the data.

**b.)** The concentration of perforin required to lyse 50% of cells (As deduced from graph in a.), plotted as a bar graph against % 7KC/cholesterol.”

#### 4.3.4 A conserved role of membrane order in perforin resistance for both the innate and adaptive immune system

Having comprehensively demonstrated the importance of high membrane order in the perforin resistance of CTLs, we investigated whether a similar association would be observed for NK cells that are equally protected from perforin within the immune synapse (Lopez, Jenkins, et al., 2013) and also to recombinant perforin (Figure 3.8). Isolated murine NK cells were loaded with 7KC and exposed to WT-PRF using similar experimental system to that in Figure 4.12. We observed a distinct sensitisation of NK cells treated with 7KC, to perforin (Figure 4.15). Seeing such agreement between experiments performed on the effector cells of both the innate (NK) and adaptive (CTL) immune system, highlights the critical importance of high membrane order of effector cells in perforin resistance.

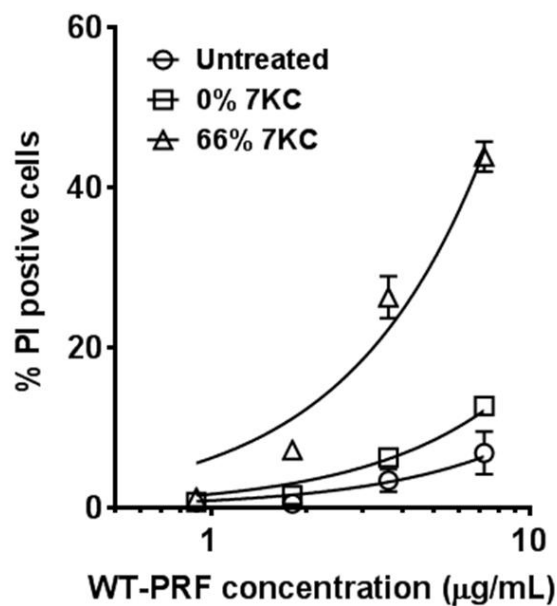


Figure 4.15: “Reduced membrane order of 7KC-treated murine NK cells sensitizes the cells to WT-PRF lysis.

Data show propidium iodide (PI) staining of untreated cells (○) and cells loaded with 0% (□), 66% (△) 7KC. Error bars represent s.e.m. ( $n = 3$  for all points except highest perforin concentration where  $n = 2$ ).”

#### **4.4 Discussion**

Using a combination of experimental approaches to investigate both artificial lipid bilayers and whole cells, we have shown a distinct preference of perforin binding to and pore formation on membranes which are in the liquid disordered state. The use of artificial lipid bilayers allowed precise control of the membrane order properties by inclusion of specific ratios of cholesterol and sphingomyelin into DOPC mixtures. Perforin was found to bind solely to liquid disordered domains, avoiding binding to high membrane order regions, as clearly visualised in phase-separated membranes. As the composition of a cellular membrane is far more complex than these model ternary mixtures of lipids, it was necessary to also test the effect of membrane order on whole cells. The reduction of membrane order in the plasma membrane of CTLs via incorporation of a disorder prone variant of cholesterol (7-ketocholesterol) as confirmed by Laurdan GP measurements, allowed these experiments to be performed. It was found that by artificially reducing membrane order of CTLs we concomitantly increased the level of TMH1-GFP-PRF binding and sensitised the cells (or membranes) to WT-PRF, suggesting a crucial function of membrane order in the overall resistance of CTLs to perforin lysis (Figures 3.7, 4.14).

“To consider this in the context of the immune synapse, we note that SM- and cholesterol-rich lipid domains (rafts) dynamically re-arrange and merge at the CTL membrane during immune synapse formation, as extensively demonstrated by others (Burack et al., 2002; Gaus et al., 2005; Owen et al., 2010). Hence, the presynaptic membrane will have a further increased lipid order compared with the overall CTL membranes tested here, thus enhancing its protection against perforin binding.”

The discovery of a role for high membrane order in cytotoxic lymphocyte self-protection has interesting implications for cancer treatment. It has recently been shown that multiple cancer types have increased plasma membrane lipid order (Guo et al., 2014; Rysman et al., 2010), and proposed explanations for this have so far speculated on a role in optimizing signalling (Erazo-Oliveras et al., 2018). Having shown the extraordinary resistance of high lipid order membranes to perforin lysis, it is tempting to speculate that this higher membrane order of cancer cells may also contribute to their immune evasion. If a target cell can become as resistant to perforin as a CTL then it could potentially be protected from cytotoxic lymphocyte attack, effectively hijacking the very mechanism used by cytotoxic lymphocyte for self-protection against perforin.

Another potential role that increased plasma membrane order may play in protecting cancer cells from cytotoxic lymphocyte attack, is a reduction in the cell membrane area that contains MHC class I molecules. MHC class I molecules are essential for presentation of antigen to CTLs and have been found to reside in non-raft regions of the membrane (Goebel et al., 2002). An increase in membrane order may reduce the number of functional MHC class I sites on the cell surface, hence contributing to immune evasion and disease progression (Garrido et al., 2016; Morrison et al., 2018).

## Chapter 5 Phosphatidylserine inactivates membrane-bound perforin

### 5.1 Introduction

Having observed an extreme CTL resistance to perforin lysis and, at the same time, mildly reduced binding to CTLs compared to target cells, an obvious question arising is how to explain this unexpected dichotomy? Does perforin form pores on CTL membrane and, if so, what makes these cells resistant to lysis?

Previous studies have provided indirect evidence for the expression of an inhibitor of perforin function on the cytotoxic lymphocyte membrane. They suggested that the levels of perforin binding to cytotoxic lymphocytes and target cells were similar, yet perforin was still unable to lyse the effector cell (Müller & Tschopp, 1994). Although we have now demonstrated that perforin binds to CTLs at lower levels than to their targets (Figure 3.12), the difference is insufficient to totally explain the hundreds of fold difference in sensitivity to perforin lysis (Figure 3.10). Therefore, it is still possible that an additional protective mechanism is also at play.

More than thirty years ago, Allbritton *et al.* (Allbritton *et al.*, 1988) showed that the addition of granule extract to the CTL cell lines 2C and G4 does not result in calcium flux as was observed for the target cell lines P815 and S49, suggesting that perforin bound to the CTLs remains inactive. However, the findings of this study were limited as it is not known how much perforin was present in the extract and if the granule extract had actually bound to the CTLs, meaning that reduced binding could be responsible for the lack of calcium flux. Therefore, we applied our recently developed fluorescent WT perforin (*WT-GFP-PRF*, (Lopez, Susanto, *et al.*, 2013)), to explore an association between perforin binding to various cells and pore formation.

## **5.2 Materials and Methods**

### **5.2.1 Indo-1AM calcium flux measurements conducted by time-lapse flow cytometry**

“CTLs and EL4 cells were labelled separately with a ratiometric (emission  $\lambda=400\text{nm}/475\text{nm}$ ) calcium fluorophore Indo-1AM (Invitrogen, California, USA) and treated with varying amounts of WT-GFP-PRF to determine amounts for which both cell types stained with a similar level of GFP (Figure 5.1). Cells treated with 1  $\mu\text{g}/\text{mL}$  ionomycin (Sigma- Aldrich, Missouri, USA) were used as controls (Figure 5.2) and time-course flow cytometry was conducted as described previously (Lopez, Susanto, et al., 2013) following WT-GFP-PRF addition (Figure 5.3).”

### **5.2.2 $\text{Ca}^{2+}$ dependence of the plasma-membrane bound perforin.**

The method for Figure 5.4 is as per that detailed in 3.2.7 *TMH1-GFP PRF binding assay*, with the following additions: both, TMH1-GFP-PRF and WT-GFP-PRF, were analysed and experiments were performed at both 4°C and 37°C. To demonstrate  $\text{Ca}^{2+}$ -specific perforin binding to CTL and target cells, a mixture of the two cell types was treated with perforin in the presence of  $\text{Ca}^{2+}$  at 4°C or 37°C for 1 hour, followed by the addition of 2 mM EGTA. The mixture of cells was then stained with anti-CD8-PE antibodies to distinguish perforin binding to CD8<sup>+</sup> CTLs and CD8<sup>-</sup> target cells, and analysed by flow cytometry.

### **5.2.3 Atomic Force Microscopy**

For details of AFM imaging, please refer to the concise summary provided in 2.5 *Atomic Force Microscopy*, and the detailed AFM methods provided in Appendix 1.

### **5.2.4 Generation of stably expressing tubulin-Cherry *Prf1*<sup>-/-</sup> OTI CTLs**

Cherry-tubulin fusion protein cDNA (Pham et al., 2015) was cloned into an MSCV vector, naive CTLs transduced as described in 2.3.2 *Transduction of naive OTI CTL* and Cherry-positive cells were sorted 3 days later and used in experiments shown in Figures 5.7-5.9, and Supplementary Videos 1-3. A tight population of Cherry fluorescence was selected, to ensure similar intensity levels of Cherry fluorescence when imaging. The cells were sorted without running calibration beads, as the cells were not being compared between different construct groups. All sorting was performed at room temperature under sterile conditions.

### **5.2.5 Fixed cell Confocal Microscopy**

#### **5.2.5.1 Sample preparation**

“Hydrophobic barriers were drawn on #1.5H coverslips (Menzel Glaser, Leicestershire, UK) using a mini-PAP PEN (Life Technologies, California, USA) and the resulting wells coated with 0.1 mg/mL Poly-L-Lysine (Sigma Aldrich, Missouri, USA) and dried for at least 2 hours. OTI T cells were pre-labelled

with annexin V-Alexa Fluor 568 (Invitrogen, California, USA) for 10 minutes at room temperature in 0.1% BSA DMEM. After washing 3 times in 0.1% BSA DMEM, cells were then treated with WT-GFP-PRF for 30 minutes at 37°C, washed 3 times and added to the wells. The cells were allowed to adhere for 10 minutes at 37°C, and the wells washed gently with Hanks Balanced Salt Solution (HBSS, Sigma Aldrich, Missouri, USA) containing 2.5 mM CaCl<sub>2</sub> and 1 mM MgCl<sub>2</sub> (both from Sigma–Aldrich, Missouri, USA) to remove any unbound cells. Cells were fixed with 4% EM Grade paraformaldehyde (Electron Microscopy Sciences, Pennsylvania, USA) (in HBSS, with 2.5mM CaCl<sub>2</sub>) for 30 minutes at room temperature, and washed with 0.1 M lysine (Sigma-Aldrich, Missouri, USA) in HBSS with 2.5 mM CaCl<sub>2</sub>. After 30 minutes, lysine was removed and samples washed 4 times with HBSS with 2.5 mM CaCl<sub>2</sub>. HBSS containing 2.5 mM CaCl<sub>2</sub> and 2% BSA was then added to the wells and incubated for 1 hour at room temperature (with gentle shaking) to block non-specific antibody binding. A 1:100 stock dilution of GFP-tag polyclonal antibody-Alexa Fluor 488 (Invitrogen, California, USA) and 2 µg/mL cholera toxin subunit B (CTxB; to label GM1)-Alexa Fluor 647 (Molecular Probes, Oregon, USA) in HBSS buffer supplemented with 2.5 mM CaCl<sub>2</sub> and 2% BSA was then added to wells and incubated overnight at 4 °C. The cells were washed 4 times, and incubated with 5 µg/mL Hoechst 34580 (Life Technologies, California, USA) for 30 minutes at room temperature. Cells were subsequently washed 4 times and allowed to dry before being mounted onto slides using Vectashield mounting medium (H1000, Vector Laboratories, California, USA) and sealed.”

#### **5.2.5.2 Imaging**

“Fixed samples (Figure 5.6 a,b) were imaged using a Zeiss Elyra PS.1 microscope, using sequential imaging in line-scan mode. A Plan-Aporchromat 63X / 1.4 Oil DIC lens (Zeiss, Oberkochen, Germany) was used with optical zoom set to 2 and a pixel size of 0.07 µm. Frame size was set to 1024 x 1024 and samples were imaged using a line average of 8 and a z stack interval of 200 nm. Background fluorescence levels for each channel were obtained using negative control images (primary omission) of the same acquisition setting and used to set thresholds for co-localisation analysis. A channel alignment slide containing 200 nm multispec beads (Zeiss, Oberkochen, Germany) was imaged and used as a reference to correct for chromatic aberration.”

#### **5.2.5.3 Co-localisation analysis**

*The Image J macro described in this section (5.2.5.3) was designed by Dr Hyung-Jung Cho.*

“An ImageJ macro was written to segment individual cells from a field of view and to create mask channels in FIJI (Schindelin et al., 2012). Colocalization analysis was performed on individual cells using Imaris 8.4.2 (Bitplane, Belfast, UK). Measurements were performed only on the region of interest set by the mask channel created from the previous process. The threshold of each channel was set as the maximum intensity value of the negative control. The degree of colocalization of channel A (Figure 5.6b) was calculated as the percentage of total colocalized A intensity above the threshold / total A intensity above the threshold.”

$$\text{colocalization} = \frac{\sum \text{colocalized A intensity above the threshold}}{\sum \text{A intensity above the threshold}} \times 100$$

Equation 2: Calculation of percentage colocalization values.

## 5.2.6 Live cell Confocal Microscopy

### 5.2.6.1 Recombinant perforin addition to a mixture of EL4 and CTLs

For Figure 5.7, Figure 5.8 and Supplementary Videos 1 and 2, “a 1:1 mixture of EL4 and Cherry tubulin expressing OTI T cells was washed 3 times in 0.1% BSA DMEM, labelled with 5  $\mu\text{M}$  Hoechst 33342 (Life Technologies, California, USA), washed 3 times and then resuspended in a 1:50 stock dilution of annexin V-Alexa Fluor 647 (Invitrogen, California, USA) in 0.1% BSA DMEM. These cells were then plated into 8-well Nunc Lab-Tek II #1.5H glass bottom chamber wells. WT-GFP-PRF was added during imaging. Cells were imaged using a Zeiss Elyra PS.1 microscope with a Tokai Hit stage/objective heater attached, and 5%  $\text{CO}_2$ /humidity maintained (Zeiss, Oberkochen, Germany). Imaging was performed using a Plan-Apochromat 63X / 1.4 Oil DIC lens (Zeiss, Oberkochen, Germany) using an optical zoom of 1 and a line average of 4.”

### 5.2.6.2 Visualizing phosphatidylserine (PS) exposure at the immunological synapse

"For live cell imaging of phosphatidylserine exposure at the immunological synapse (as detected by annexin V labelling) (Figure 5.9, Supplementary Video 3), MC57 target cells were trypsinised and washed.  $10^6$  cells were then resuspended in 500  $\mu\text{L}$  of 5  $\mu\text{M}$  Cell Trace Violet (CTV) solution (Invitrogen, California, United States) in PBS for 20 minutes at 37°C. 10 mL of complete media was then added to these cells to quench any unbound dye. Cells were pelleted, resuspended in complete DMEM media, counted and plated at 30,000 cells per well ( $10^6$  cells/mL) of an 8-well Ibidi-treat imaging chamber (Ibidi, Martinsried, Germany), one day before imaging. Approximately 4 hrs before imaging, cells were labelled with 1  $\mu\text{M}$  SIINFEKL octapeptide (GenScript, New Jersey, USA) at 37°C for 1 hr, before being washed 3 times in complete DMEM, and allowed to rest. Cherry-tubulin-transduced *Prf1*<sup>-/-</sup> OTI T cells were then resuspended in 300  $\mu\text{L}$  of a 1:50 stock dilution of annexin V-Alexa Fluor 488 (Invitrogen, California, USA) in complete DMEM before being added to the microscopy chamber. All media was removed from the MC57 cells, such that both the MC57 and OTI T cells were imaged in the presence of a 1:50 stock dilution of annexin V-Alexa Fluor 488. Cells were imaged using a Zeiss Elyra PS.1 microscope with a Tokai Hit stage/objective heater attached, and 5%  $\text{CO}_2$ /humidity maintained (Zeiss, Oberkochen, Germany). Imaging was performed using using a C-Aporchromat 63X / 1.2 W Korr UV-VIS-IR lens (Zeiss, Oberkochen, Germany) using an optical zoom of 1 and a line average of 8.”

## 5.3 Results

### 5.3.1 Perforin association with CTLs: Binding without pore formation

Sections (5.3.1 and 5.3.2) were completed with the technical assistance of Ms. Tahereh Noori. After I designed and optimised the experiments, she performed independent replicates and collated the data. I finalised all data presentation and performed statistical analysis of Figure 5.1.

To investigate perforin binding to live cells, the fully-functional fluorescent fusion protein WT-GFP-PRF (Lopez, Susanto, et al., 2013) was utilised. This enabled simultaneous analysis of perforin membrane binding and calcium flux (indicating membrane disruption by perforin). Since perforin binding to CTLs is less efficient than to target cells, the availability of fluorescently-labelled perforin enabled perforin to be adjusted to achieve similar levels of perforin binding to EL4 and CTL. To this end, firstly a sub-lytic concentration of WT-GFP-PRF was determined for the EL4 cells (independently, on the day of each experiment), and then increasing amounts of WT-GFP-PRF were added to the CTLs until a similar MFI was achieved. By gating the cells of the same size during analysis, it was possible to examine the calcium influx into CTLs or EL4 cells exposed to sub-lytic levels of perforin bound to them. Figure 5.1 shows the geometric mean fluorescence intensity levels of both CTLs and EL4 with and without addition of WT-GFP-PRF. Only the first timepoint showed a significant difference in GFP MFI between EL4 and CTLs treated with WT-GFP-PRF. After 30 seconds, no significant difference was observed between these groups, confirming that the calcium flux analysis was performed on cells that had bound similar levels of perforin.

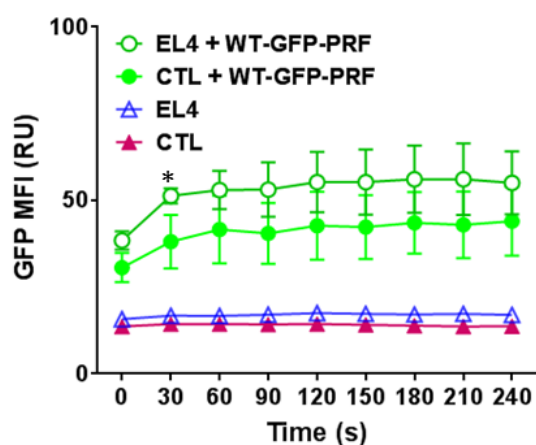


**Figure 5.1:** “Similar levels of perforin bound to EL4 and CTLs.

By adding approximately twice the amount of WT-GFP-PRF to CTLs as was added to EL4 cells, similar levels of perforin binding (represented by GFP MFI) were obtained. Each data point represents a mean ( $\pm$  S.D.) of 3 independent experiments. An unpaired t-test performed on EL4 + WT-GFP-PRF and CTL + WT-GFP-PRF shows  $P < 0.05$  for  $t = 30$  s, but no significant difference for all other time points.”



To assess the efficiency of CTLs and EL4 labelling with Indo-1 AM – which is used to compare calcium flux across different cell types - the cells were treated with a calcium ionophore ionomycin. Similar calcium flux profiles were observed with both cell types (Figure 5.2) confirming similar intracellular levels of indo-1 and no significant difference in the indo-1 response to Ca influx.

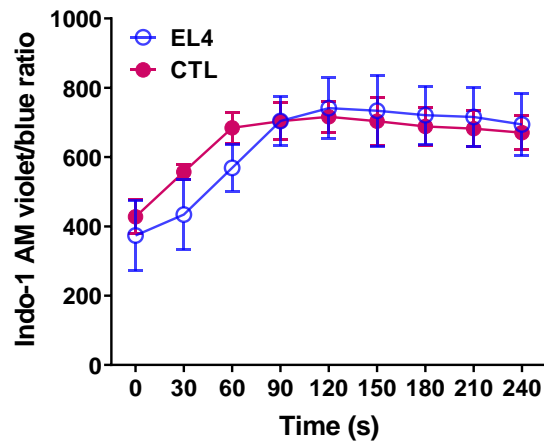


**Figure 5.2:** “A similar response to Ionomycin treatment is observed for both EL4 and CTLs.

The addition of Ionomycin to the indo-1-am labelled cells increases calcium levels in the cell leading to a shift in fluorescence from blue to violet, resulting in a distinctive peak on the violet/blue fluorescence ratio over time. Each data point represents a mean ( $\pm$  S.D.) of 3 independent experiments.”

Having now confirmed that both cell types could be labelled successfully with Indo-1 AM and that WT-GFP-PRF binding to both cell types could be titrated to achieve similar levels of PRF bound on the cell surface, a direct comparison of membrane disruption due to perforin was possible. EL4 cells showed a distinct  $\text{Ca}^{2+}$  influx (detected by the increase in violet/blue ratio) after WT-GFP-PRF addition, whereas CTLs showed no detectable calcium flux (Figure 5.3). This striking difference agrees with previous studies (Allbritton et al., 1988) but provides the additional information that absence of membrane damage on the CTL is not due to lack of perforin binding. We hypothesized that this unexpected additional “layer” of CTL resistance to perforin could play an important role in cytotoxic lymphocyte self-protection.

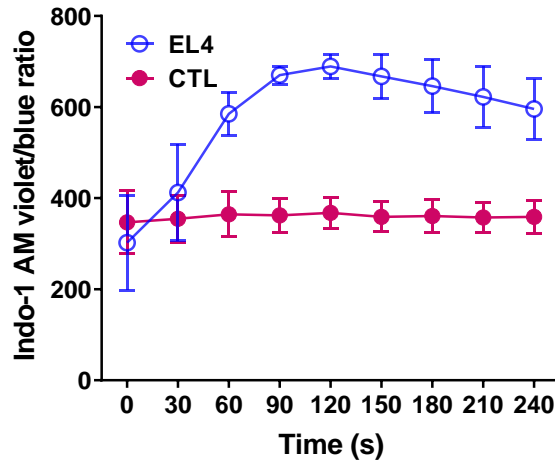


**Figure 5.3: “Ca<sup>2+</sup> influx into Indo-1 AM labelled CTLs and EL4 cells upon exposure to sublytic amounts of WT-GFP-PRF.**

Membrane perforation by perforin was measured via the Ca<sup>2+</sup> influx over time, detected as an increase in the ratio of violet (400nm) to blue (475nm) fluorescence emission; WT-GFP-PRF was added at  $t = 0$ . Curves provide a visual guide connecting data points. Each data point represents a mean ( $\pm$  S.D.) of 3 independent experiments.”

### 5.3.2 EGTA resistance of WT-GFP-PRF bound to CTLs; attachment without insertion?

It has been shown that perforin binding is calcium dependent (sensitive to EGTA), but only up until the point that perforin inserts into the membrane (Müller & Tschopp, 1994). Membrane-inserted perforin remains attached to the membrane even after the removal of calcium (resistant to EGTA). Since perforin insertion does not occur at 4 degrees (or is dramatically delayed by hours), we reasoned that by comparing EGTA sensitivity of WT-GFP-PRF bound to a mixture of CTLs and EL4 cells at 4°C and 37°C it should be possible to determine whether perforin bound to CTLs at 37 degrees has inserted into the membrane. A further control is provided by the EGTA sensitivity of TMH1-GFP-PRF at 37°C, as this mutant is unable to insert into the membrane (Leung et al., 2017) and, therefore, it should remain EGTA sensitive even at 37°C.

Intriguingly, it was found that unlike TMH1-GFP-PRF, the WT-GFP-PRF bound to CTLs at 37°C was EGTA resistant (Figure 5.4) even though there was no apparent lytic pore formed (Figure 5.3). Thus perforin attachment to CTL plasma membrane had become Ca<sup>2+</sup>-independent, a finding previously considered possible only for perforin that formed stable pores.

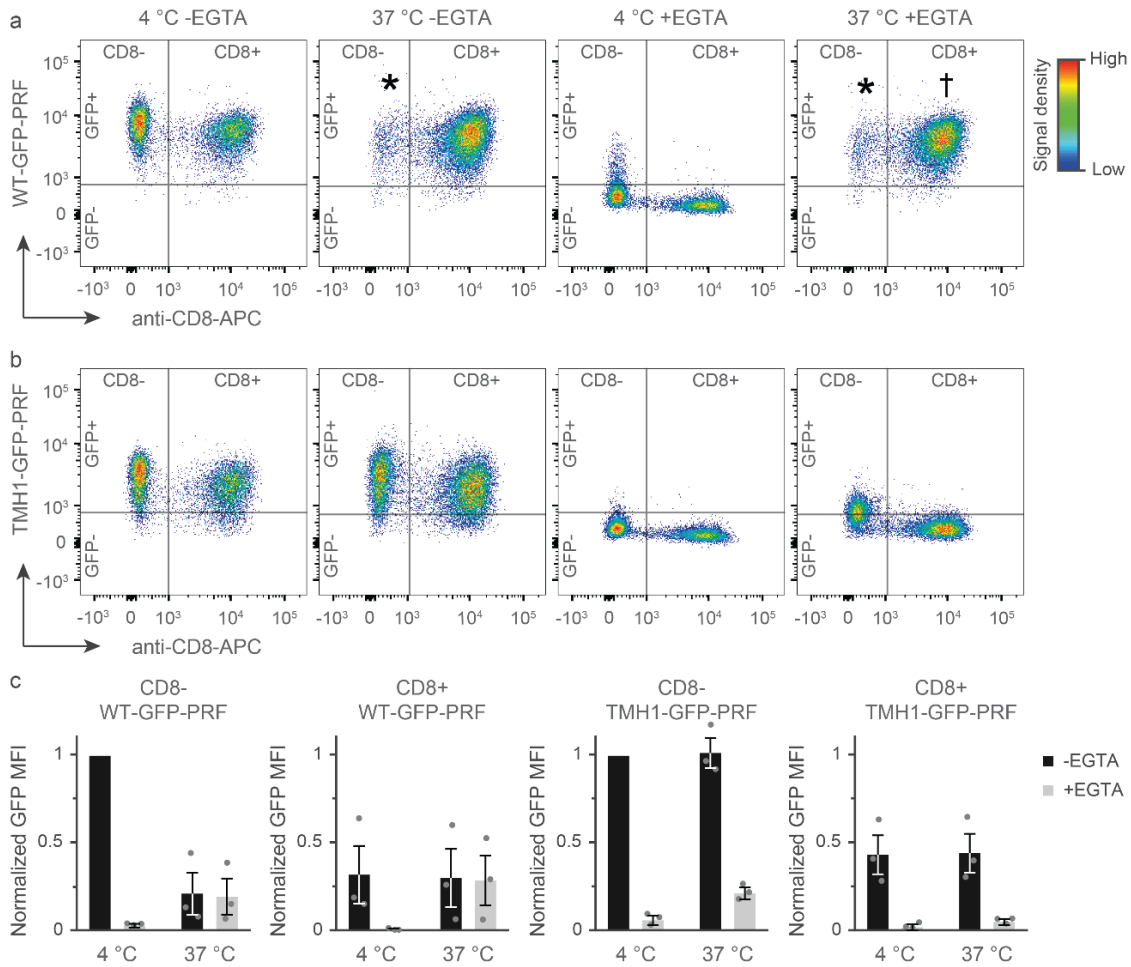


**Figure 5.4: “Flow cytometry on WT-GFP-PRF and TMH1-GFP-PRF binding to EL4 (CD8<sup>-</sup>) and CTLs.**

**a.)** Binding of WT-GFP-PRF to EL4 (CD8<sup>-</sup>) and CTL (CD8<sup>+</sup>), at concentrations that are sub-lytic to CTLs, as assessed by flow cytometry. At 4°C and in the presence of Ca<sup>2+</sup> (-EGTA), both cell types bind perforin (GFP<sup>+</sup>), but the CTLs at a lower level than EL4 cells. At 37°C and in the presence of Ca<sup>2+</sup> (-EGTA), WT-GFP-PRF is lytic to the EL4 cells, so no significant CD8<sup>-</sup> population remains under those conditions (asterisks). Upon subsequent Ca<sup>2+</sup> chelation by 2 mM EGTA, non-porating perforin assemblies (WT-GFP-PRF at 4°C) are removed from the cell membranes (GFP<sup>-</sup>). However, Ca<sup>2+</sup> chelation does not affect WT-GFP-PRF bound to CTLs at 37°C (GFP<sup>+</sup>, dagger), despite WT-GFP-PRF being apparently non-porating (see Figure 5.3).

**b.)** Binding of non-lytic TMH1-GFP-PRF to EL4 (CD8<sup>-</sup>) and CTL (CD8<sup>+</sup>), as assessed by flow cytometry. In the presence of Ca<sup>2+</sup> (-EGTA), TMH1-GFP-PRF binds to both cell types, but less to CTLs, as observed for WT-GFP-PRF. Upon subsequent Ca<sup>2+</sup> chelation by 2 mM EGTA (+EGTA), TMH1-GFP-PRF is invariably removed from the cell membranes, leaving only GFP<sup>-</sup> populations (both at 4°C and 37°C).

**c.)** Quantification of flow cytometry results, with MFI of WT-GFP-PRF and TMH1-GFP-PRF signals, normalized to the respective MFIs for the CD8<sup>-</sup> population at 4°C. EGTA exposure drastically reduces the GFP MFI for all cases at 4°C, as well as for the (non-lytic) TMH1-GFP-PRF at 37°C. By contrast, WT-GFP-PRF is EGTA resistant once bound to CD8<sup>+</sup> cells at 37°C. Note that the low GFP MFI at 37°C in the first panel (CD8<sup>-</sup>; WT-GFP-PRF) is due to the majority of the CD8<sup>-</sup> cells being killed and thus not yielding a GFP signal in the flow cytometer anymore. The TMH1-GFP-PRF data (-EGTA) allow for a quantitative comparison between binding to CD8<sup>+</sup> and CD8<sup>-</sup> cells, showing that the CTLs (CD8<sup>+</sup>) bind less than half as much perforin as the target cells (CD8<sup>-</sup>). Each column represents a mean (± s.e.m.) of 3 independent flow cytometry experiments.”

### **5.3.3 EGTA resistance of perforin clusters formed on Phosphatidylserine rich lipid bilayers**

*The experiments described in this section (5.3.3) were designed and performed by Dr Adrian Hodel and are included to provide context to the study.*

“To determine if other lipid types could be responsible for EGTA resistance of membrane-attached perforin, the AFM analysis was expanded to phospholipids that are typically located in the inner leaflet of the plasma membrane (Leventis & Grinstein, 2010). Surprisingly, it was found that perforin efficiently bound to membranes composed of phosphatidylserine (PS), but did not form the well-defined, static arc or ring-shaped assemblies that are characteristic of transmembrane pores (Figure 5.5a) (Law et al., 2010; Leung et al., 2017; S. S. Metkar et al., 2015). Instead, WT-PRF and DTT-unlocked TMH1-PRF formed static protein clusters on PS, which sat up to ~5 nm higher above the membrane surface than locked (-DTT) TMH1-PRF prepores on both PC and PS. These static clusters were also higher (by the same amount) than functional perforin (WT-PRF and TMH1-PRF +DTT) on PC membranes. Fully consistent with the observations on CTL-bound perforin (Figure 5.4), the perforin clusters on PS membranes were resistant to Ca<sup>2+</sup> depletion by EGTA (Figure 5.5b). In binary PC/PS mixtures, cluster formation was increased and functional pore formation reduced upon increasing PS content (Figure 5.5c).”

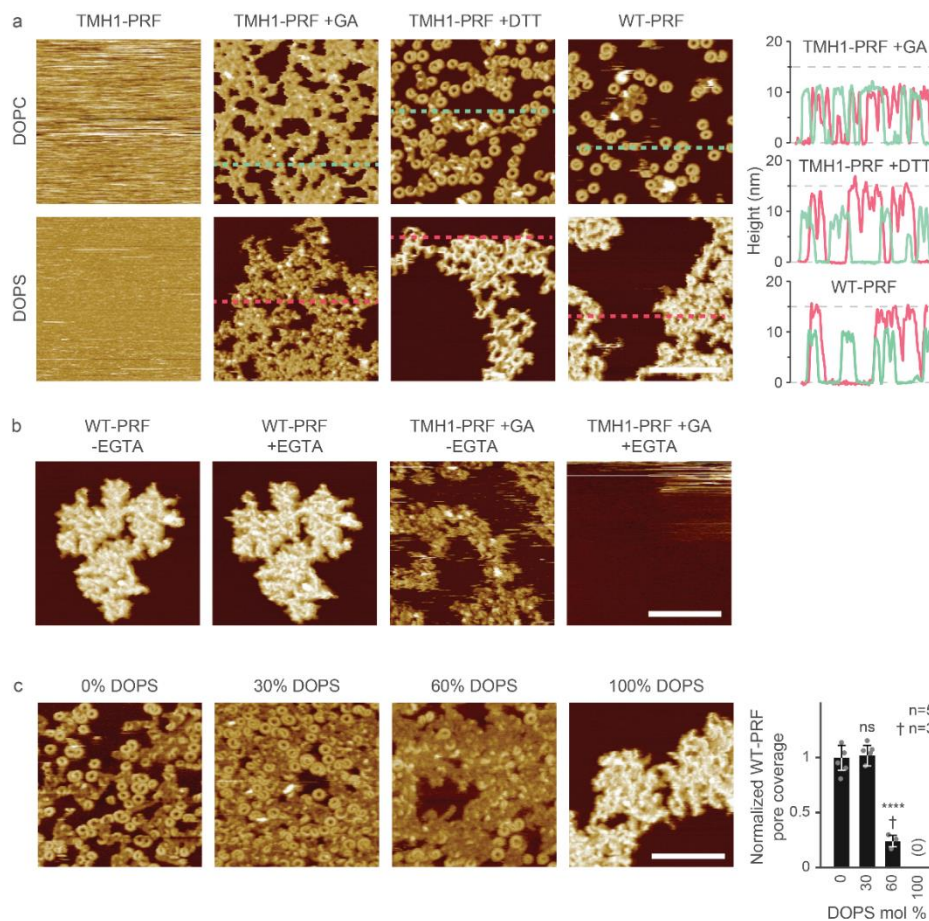


**Figure 5.5: “Perforin forms non-porating clusters on phosphatidylserine membranes.**

**a.)** AFM images of DOPC and DOPS supported lipid bilayers after incubation with TMH1-PRF without or with glutaraldehyde (+GA) fixation, with unlocked (+DTT) TMH1-PRF, or with WT-PRF. Height profiles were plotted as acquired along the dashed lines in the AFM image. On DOPC, prepore locked TMH1-PRF, and TMH1-PRF +DTT and WT-PRF assemblies all extend 10-11 nm above the membrane surface, in agreement with previous observations (Law et al., 2010; Leung et al., 2017; S. S. Metkar et al., 2015). On DOPS, fixed (and locked) TMH1-PRF assemblies have the same height, but the clusters of unlocked TMH1-PRF (+DTT) and WT-PRF are distinctly taller, about 15 nm above the membrane.

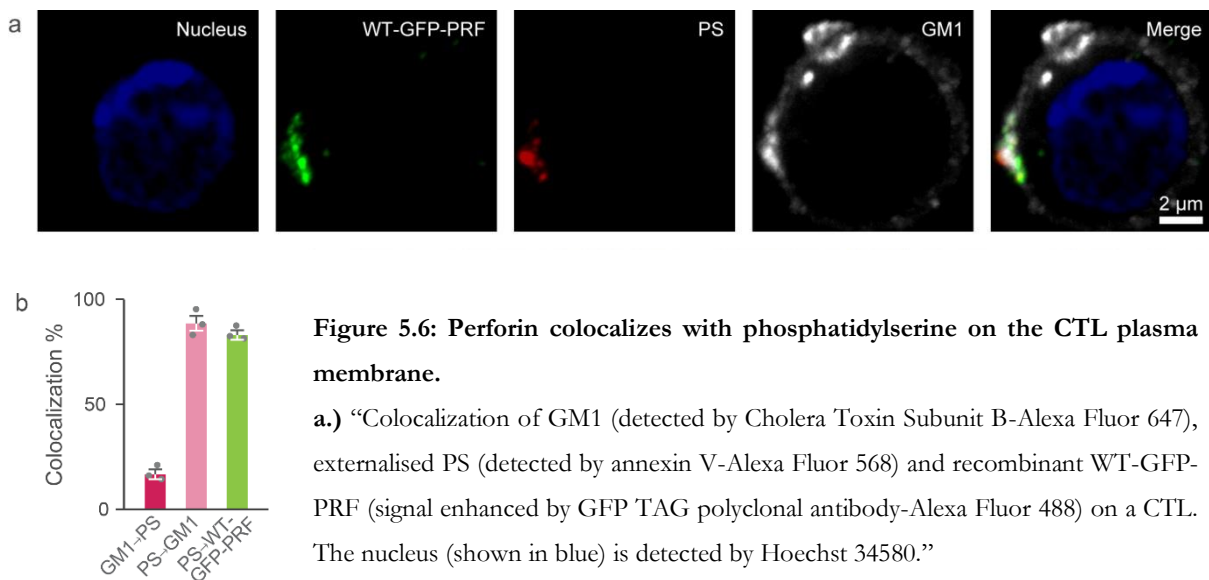
**b.)** AFM images of supported DOPC bilayers mixed with 0-100% DOPS, after incubation with 150 nM WT-PRF. The images show decreased formation of arc- and ring-shaped perforin pores upon increased DOPS content, and an increased amount of clustering. Samples were incubated at 37°C and imaged at room temperature. Colour (height) scale as in Figure 4.7b. Bar graph on the right shows quantification (see Methods; mean  $\pm$  SD) of pore formation on DOPS containing membranes: For 60% DOPS, there is a significant decrease in the number of pores, and at 100% DOPS there are no unambiguous pore features found. Statistical significance was assessed using ANOVA with Dunnett’s post-hoc analysis, where ‘ns’ - not significant, \*\*\*\*  $p < 0.001$ .

**c.)** AFM images of DOPS supported lipid bilayers incubated with WT-PRF or TMH1-PRF +GA, before and after  $\text{Ca}^{2+}$  chelation by washing the membrane with 5 mM EGTA ( $\pm$  EGTA). Clusters formed by WT-PRF are not removed or visibly affected by washing the membrane with EGTA. In contrast, cross-linked plaques of TMH1-PRF +GA are removed after the EGTA wash. This is consistent with failure of TMH1-PRF to insert into the membrane (Leung et al., 2017) and suggests that WT-PRF partially inserts into the DOPS membrane. All AFM samples in **a** and **b** were incubated at 37 °C and imaged at room temperature.”

Having observed the inactivation of perforin by PS in model lipid membranes, we hypothesized that any regions of PS exposed on the CTL plasma membrane outer leaflet may be responsible for irreversible perforin binding that is not associated with pore formation (Figures 5.3, 5.4).

### 5.3.4 Phosphatidylserine - a marker of the dead that protects the living.

“If the hypothesis was correct, we would expect perforin to co-localize with exposed PS (Elliott et al., 2005) on the CTL plasma membrane. To test this, we performed confocal microscopy on activated CTLs that were pre-treated with annexin V-Alexa Fluor 568, as a marker for PS exposed on the cell surface (Koopman et al., 1994). Importantly, this pre-labelling with annexin V ensured detection only of PS already exposed on the CTL membrane before perforin addition, thus avoiding any contribution of PS flip/flop upon perforin association with the plasma membrane (S. S. Metkar et al., 2011). WT-GFP-PRF colocalized with punctate regions corresponding to (non-apoptotic) externalized PS (Figure 5.6 a,b). These punctate regions were also enriched for the lipid-raft marker cholera toxin B (labelled GM1 in Figure 5.6 a,b), as was previously reported for both CTLs (Fischer et al., 2006) and B cells (Dillon et al., 2000).”



**b.)** “Quantitative analysis (as described in the Methods) of **a** shows low colocalization levels of GM1 with PS (17%) but high colocalization of PS with GM1 (88%) and PS with WT-GFP PRF (83%). This indicates that the vast majority of PS is contained within lipid raft areas (whereas there are many lipid raft areas which do not contain PS) and more than 80% of this PS binds WT-GFP-PRF. A total of 62 cells were analysed, and the mean of 3 independent experiments is shown for each condition ( $\pm$  s.e.m.).”



“To directly investigate the efficacy of this protective mechanism, WT-GFP-PRF was added to a 1:1 mixture of EL4 cells and CTLs in the presence of annexin V-Alexa Fluor 647 to identify exposed PS. EL4 cells bound perforin uniformly around their periphery and were lysed within minutes, whereas on CTLs perforin signal was strongly associated with distinct regions where PS was exposed (Figure 5.7; Supplementary Video 1).” When the cells were imaged again 1 hour after perforin addition (having been maintained at 37°C and 5% CO<sub>2</sub>), it was observed that the CTLs were still viable and had maintained a healthy morphological appearance and mobility (Figure 5.8, Supplementary Video 2).

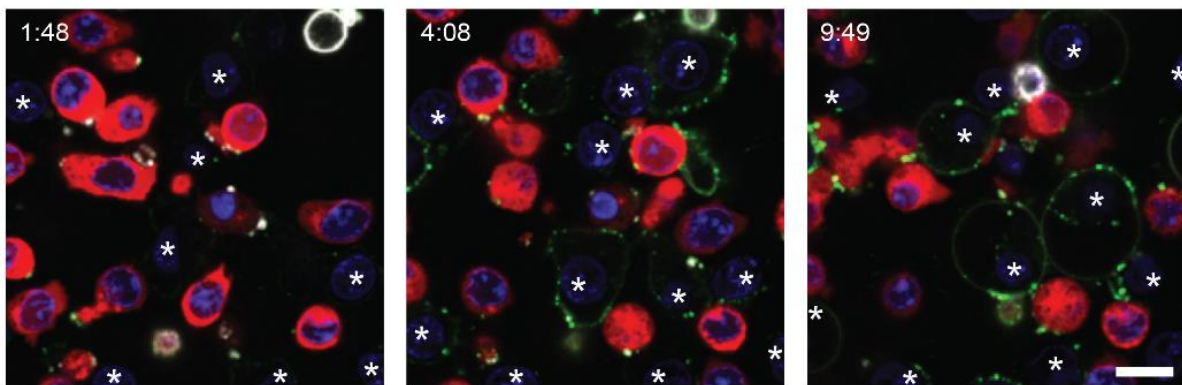


**Figure 5.7: “Time-lapse microscopy highlights different response of CTL’s and EL4 to addition of WT-GFP PRF. (Supplementary Video 1).**

WT-GFP-PRF (shown in green, added at time 1:17 min) was added to a mixture of CTLs transduced with cherry-tubulin (shown in red) and EL4 cells (highlighted by white asterisks in panel 1). Hoechst 33342 (shown in blue) staining shows the nucleus of both cell types. Annexin V-Alexa Fluor 647 (shown in white) was maintained in the culture medium throughout the assay; it binds to PS exposed on the CTLs and to PS on and within EL4 cells that are exposed to cytotoxic levels of perforin and lose membrane integrity. EL4 cells are seen to bind WT-GFP-PRF uniformly before gradually becoming annexin V positive, whilst perforin on the CTLs membrane localizes precisely (and almost immediately) to regions of exposed PS, without lysing the cells (Supplementary Video 2).”

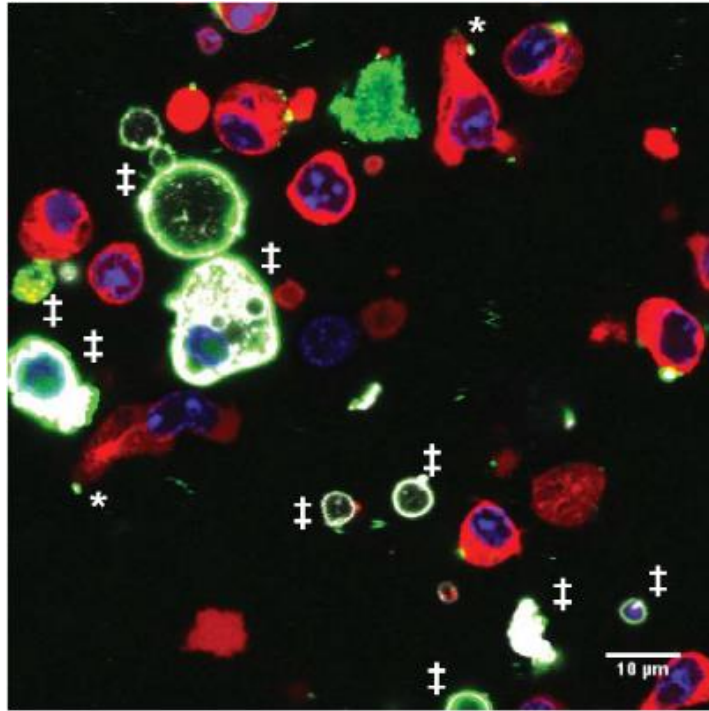


**Figure 5.8: “Unlike target cells, CTLs maintain healthy morphological appearance and mobility one hour after addition of WT-GFP-PRF.**

CTLs (red) with clear WT-GFP-PRF signal (green) localized to punctate regions of non-apoptotic PS (white) 1 hour after addition of perforin. Dead target cells and their debris are stained bright green and white (highlighted by white daggers), because of, respectively, their overall WT-GFP-PRF binding and staining for apoptotic PS. Note that on polarised CTLs, non-apoptotic PS is always located within the uropod (white asterisks). Staining is as in Figure 5.7; the data shown here represent a snapshot from Supplementary Video 2.”



### 5.3.5 Phosphatidylserine is exposed on the CTL membrane during synapse formation

Previous studies have noted the exposure of PS on the human CTL membrane following antigen recognition and synapse formation (Fischer et al., 2006) as detected by the multivalent phosphatidylserine binding protein, annexin V. Further evidence of PS accumulation within the immune synapse has been provided by mass spectrometry of membrane regions isolated using anti-CD3 beads (Zech et al., 2009). The observation that PS is present within the synapse suggests that it can potentially scavenge and inactivate perforin as seen on PS rich membrane (Figure 5.5), thus providing the 2<sup>nd</sup> line of defence for cytotoxic lymphocyte self-protection against secreted perforin. To investigate the phenomenon of PS exposure within the CTL-target immune synapse, we visualised PS exposure using time-lapse live cell microscopy.

*Prf1*<sup>-/-</sup> OTI CTLs were transduced with a tubulin-cherry fusion construct (Pham et al., 2015) to allow visualisation of centrosome docking at the immune synapse (to confirm synapse formation). Cell Trace Violet labelled MC57 targets were pulsed with SIINFEKL peptide, before being exposed to the CTLs in the presence of annexin V-Alexa Fluor 488, to detect any exposed PS. Consistent with the previously published observations by Fischer et al, a bright punctate region of annexin V fluorescence was observed within the synapse, indicating the presence of PS (Figure 5.9, Supplementary Video 3).

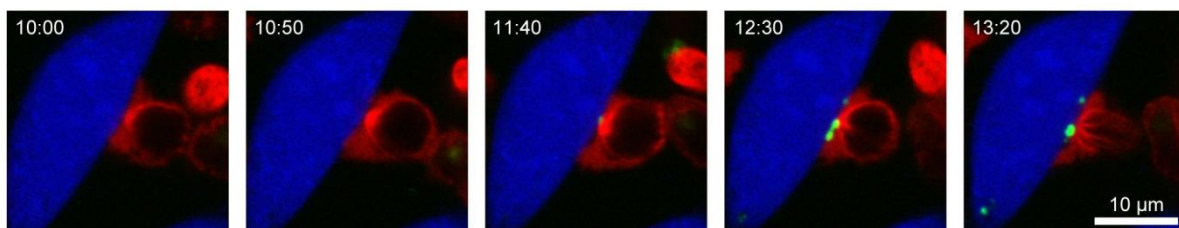


**Figure 5.9: “Time-lapse confocal microscopy confirms PS exposure on pre-synaptic membrane upon synapse formation.**

Montage of time-lapse confocal microscopy (Supplementary Video 3) reveals a bright punctate region of PS (detected by annexin V-Alexa Fluor 488 maintained during assay; shown in green) exposed on the CTLs membrane during synapse formation. Cell Trace Violet labelled target cells (MC57, shown in blue) were labelled with SIINFEKL and synapse formation is confirmed by the docking of the centrosome (detected by tubulin-cherry expressed in the CTLs; shown in red) at the point of contact between CTL and target. Timestamps are in minutes.”

## 5.4 Discussion

Here, we used GFP tagged recombinant perforin (Lopez, Susanto, et al., 2013) to determine the mechanism of the previously observed CTL resistance to perforin pore formation (Allbritton et al., 1988). Indeed, we show that even when CTLs bind equal amounts of perforin as target cells (by addition of higher concentrations of perforin), it fails to disrupt CTL membrane, as assessed by the lack of  $\text{Ca}^{2+}$  influx into the cell. Remarkably, CTL-bound non-porating perforin acquired properties of perforin pores, ie it became calcium independent (Figures 5.4 and 5.5.), a feature of perforin inserted into the membrane (Müller & Tschopp, 1994). These findings presented a paradox of perforin that has inserted/attached to the membrane irreversibly but not formed pores. By analysing perforin pore formation on lipid bilayers composed of varying concentrations of phosphatidylserine, it was subsequently found that a remarkably similar phenomenon occurs: instead of forming transmembrane pores, perforin assembles into non-porating structures that are resistant to removal by EGTA, lack the tight packing and resemble prepores (Rudd-Schmidt et al., 2019).

We hypothesized that exposure of PS on the outer leaflet of the T cell plasma membrane could be responsible for binding EGTA resistant but non-porating perforin. A strong colocalisation between PS (marked with annexin V) and recombinant WT-GFP-PRF observed using confocal microscopy, and the lack of perforin pores, as measured by  $\text{Ca}^{2+}$  flux, provided strong evidence in support of this hypothesis. To directly compare the efficacy of this protective mechanism, we added WT-GFP-PRF to a 1:1 mixture of CTL and EL4 targets whilst performing confocal imaging. Perforin bound to uniformly and lysed EL4 target cells, whilst on CTLs it preferentially localised to distinct regions of exposed PS and the cells remained intact (Figure 5.7, Figure 5.8. Supplementary videos 1 & 2). In fact, even one hour after the addition of WT-GFP-PRF, CTLs were seen to maintain healthy morphology, suggesting the perforin had been scavenged and completely inactivated. An immune synapse is a directed event, with perforin only released at the synaptic cleft. Therefore to put this protective mechanism into a physiologically relevant context, we set out to explore previous findings (Fischer et al., 2006), which demonstrated an exposure of PS on the pre-synaptic membrane upon antigen recognition, in real time. We show that upon synapse formation between the CTL and antigen-presenting target cells, PS was exposed on the presynaptic membrane (as detected by fluorescently labelled annexin V). This provided further evidence for our hypothesis that exposed PS within the immune synapse can act as a sink that binds and inactivates any perforin reaching the CTL membrane.

Non-apoptotic surface exposed PS has been shown to be increased in a number of cancer cells types (Riedl et al., 2011) and anionic phospholipids including PS have also been shown to be exposed to an increased level in tumour blood vessels (Ran et al., 2002). This abnormally elevated PS exposure in the tumour microenvironment has been shown to contribute to immunosuppression (Birge et al., 2016). Our current results suggest that the presence of these high levels of PS may not only create an immunosuppressive environment, but also inactivate perforin released by cytotoxic lymphocytes that overcome the immunosuppressive environment and form a synapse with these tumour cells.

The negative charge of PS allows specific cancer cell targeting by cationic peptides (Wodlej et al., 2019) and cationic liposomes (De et al., 2018). PS has also recently been successfully targeted by nanovesicles composed of Saposin C (SapC) coupled with Dioleoylphosphatidylserine (DOPS) (N'Guessan et al., 2020; Qi et al., 2009). A potential side-effect of these strategies, given the constitutive exposure of PS on activated CTLs (Figure 5.6, Figure 5.7), is the effect that such PS targeting molecules may have on CTL function. Will a payload of cytotoxic molecules intended solely for cancer cells also be delivered to all activated CTL? The fact that CTLs which have bound WT-GFP-PRF to their regions of exposed PS remain viable and motile (Figure 5.7, Figure 5.8. Supplementary videos 1 & 2), suggests immune function may not be interrupted by simply having a PS targeting marker for visualisation of tumours. However, if the PS targeting peptide/liposome/nanovesicle releases a toxic payload at this point of binding, this may adversely affect T cells thus adding to the already substantial problem of immunosuppression in the tumour microenvironment (Dunn et al., 2002; Mellman et al., 2011). It is, therefore, important to consider that potential side-effect of PS-targeting nanodrugs in pre/clinical trials.

A recent *in vivo* study showed that killing of tumour cells was increased when PS was blocked with a mouse anti-PS monoclonal antibody (mch1N11) (Gray et al., 2016). They found that when mch1N11 was used in combination with anti PD-1 therapy, the effect was further enhanced. This was attributed to increased tumour-infiltrating lymphocytes (TILs), increased expression of pro-immune activating cytokines and cell types, as well as downregulated pro-tumorigenic cytokines, all of which were observed after treatment. Given our current findings, it is tempting to speculate that blocking PS on target cells may also result in an increased susceptibility of these cells to perforin and therefore cytotoxic T cell attack, which could also contribute to the observed result of enhanced killing. Specific experiments looking at this will be worthwhile endeavours in the future. Interestingly, small doses of radiotherapy have been shown to be associated with increased PS exposure (Davis et al., 2019) and reported to induce angiogenesis around the tumour at the site of radiation exposure (Sofia Vala et al., 2010). A study using SapC-DOPS nanovesicles suggested this increase of PS could be utilised to sensitise cells prior to treatment with the PS-targeting nanovesicles (Davis et al., 2019).

It is worth noting that Phase 1 clinical trials using the PS specific antibody Bavituximab in combination with radiation therapy and chemotherapy (Capecitabine) have shown no toxicity (Meyer, 2018), paving the way for more extensive trials of PS antibodies in combination with traditional treatment regimens such as chemotherapy and radiotherapy. However, a recent review detailing antibody targeting of PS for the detection and immunotherapy of cancer (Belzile et al., 2018) has been criticised for the lack of discussion about the potential risk of complications relating to increased risk of thromboembolic events when PS is targeted (Zohar & Shoenfeld, 2018). Future studies will need to be carefully designed to account for this risk to ensure benefits outweigh potential side effects of the treatment.

## Chapter 6 Conclusion and Future Directions

### 6.1 “Lipid Order and Charge Protect Killer T cells from Accidental Death”

The first indications that CTL are protected from their own cytolytic granules within the synapse came from the early observations of killer cells being able to kill multiple target cells in succession, without being killed themselves (Berke et al., 1972; Rothstein et al., 1978). At this time, the mechanism of cytotoxicity was yet to be elucidated, nor had either perforin or granzymes been discovered, and so it was not possible to address the issue of CTL survival at the molecular or cellular level (Golstein, 1974). During the 1980s, population cell-based experiments identified the resistance of the CTL membrane to the content of their own cytolytic granules (Blakely et al., 1987; Shinkai et al., 1988; Verret et al., 1987). Although these studies hypothesized that such resistance would be important for the protection of killer cells during synapse interactions, no direct evidence that the CTL was specifically protected from perforin within the spatial confines of the immune synapse was presented, due to technical limitations and the lack of knowledge of the lipid organisation of the immune synapse.

In 2013, Lopez et al (Lopez, Susanto, et al., 2013) developed a novel technique in which PI added to culture medium would fluoresce upon entry into the target cell through transiently formed perforin pores - this allowed the observer to infer perforin pore formation in a live single-cell microscopy setting. Notably, the ‘blush’ of PI fluorescence was virtually never observed in the killer cell (see below). Importantly, this technique was applicable for use in imaging of immune synapse interactions. It permitted a detailed analysis and recording of discrete events such as the effector-target cell conjugation, calcium influx into the effector cell that triggers degranulation, target cell permeabilization by perforin and target cell apoptosis (Lopez, Jenkins, et al., 2013; Lopez, Susanto, et al., 2013). In this study, which analysed innate and adaptive cytotoxic lymphocytes from both mice and humans, it was conclusively shown that the cytotoxic lymphocyte membrane is protected from perforin pore formation within the immune synapse, as <1% of effector cells were permeabilized by perforin during synapse formation with target cells that were invariably punctured by perforin. This was the first direct evidence of cytotoxic lymphocytes being protected from their toxic cargo specifically due to resistance of the pre-synaptic membrane to perforin. In this same study (Lopez, Jenkins, et al., 2013), it was found that when loaded with a cognate peptide antigen, CTLs could become targets and be killed by a similar syngeneic CTL, indicating that protection from perforin is not absolute, but rather, is deployed specifically by the cell imparting the lethal hit, but not in the target. However, how this distinction could be made in cells derived from the same starting population remained unknown.

In this thesis, we identify that pre-synaptic membrane composition of CTLs is the primary factor in their protection from perforin (Rudd-Schmidt et al., 2019). Comprehensive experiments performed on both ternary lipid bilayer mixtures and with far more complex, but physiologically relevant whole cells demonstrated a clear preference of perforin binding for low order membranes, with high order membranes being refractory to perforin binding. This is consistent with the previous observations that perforin resistance is enhanced during synapse formation (Lopez, Jenkins, et al., 2013), as high membrane order lipid rafts are known to converge on the pre-synaptic membrane of effector cells

(Burack et al., 2002; Gaus et al., 2005; Owen et al., 2010), while antigen-presenting cells have their MHC class 1 locating to lower membrane order 'non-raft' regions (Goebel et al., 2002).

In addition to the 'shield' of high membrane order which protects the CTL from perforin binding, we have also found that PS is exposed on the outer leaflet of the pre-synaptic CTL membrane binds and inactivates any residual perforin that may bind. PS is normally localised to the inner leaflet of the plasma membrane and is only exposed when a cell undergoes apoptosis, but this is not the case with cytotoxic lymphocytes engaged in synapse formation. Thus the calcium influx results in the localised inhibition of flippase (Fischer et al., 2006; Ma et al., 2017) leading to PS externalisation at the pre-synaptic membrane, and this correlates well with the finding of increased perforin resistance during synapse formation. Overall, the combination of a high membrane order 'shield' and a sink of negatively charged PS to bind and inactivate any perforin that reaches the CTL membrane (Figure 6.1), provides CTLs with a level of redundancy in their self-protection, allowing them to function as effective serial killers.

The importance of this is paramount, as "unregulated binding and pore formation by perforin on the plasma membrane of CTLs and other cytotoxic lymphocytes would make immune killer cells as vulnerable to their own secreted potent cytotoxins as a target cell, and greatly reduce the efficiency of a cytotoxic response to dangerous pathogens. For example, killer cells would have to be raised in at least equal numbers to virus-infected cells to ensure clearance of any infection (Bocharov et al., 2015; Seedhom et al., 2009)—this would be a particular challenge in major organs such as the liver, where many trillions of parenchymal cells are typically infected in a very short time-frame. In addition, if every CTL was to die following interaction with a target cell, this would preclude any antigen-experienced CTL from differentiating into a memory cell. Clearly, such a scenario would have dire repercussions for the immune system's ability to efficiently eliminate serious pathogens, while compromising antigen recall responses and immune homeostasis. It is therefore not surprising that mammals have evolved mechanisms to ensure that perforin's deleterious effects on the killer cell are carefully controlled, just as there are multiple mechanisms in place to prevent the premature activation of perforin during its biosynthesis, processing, storage and release (Brennan et al., 2011; House et al., 2017; Lopez et al., 2012)."

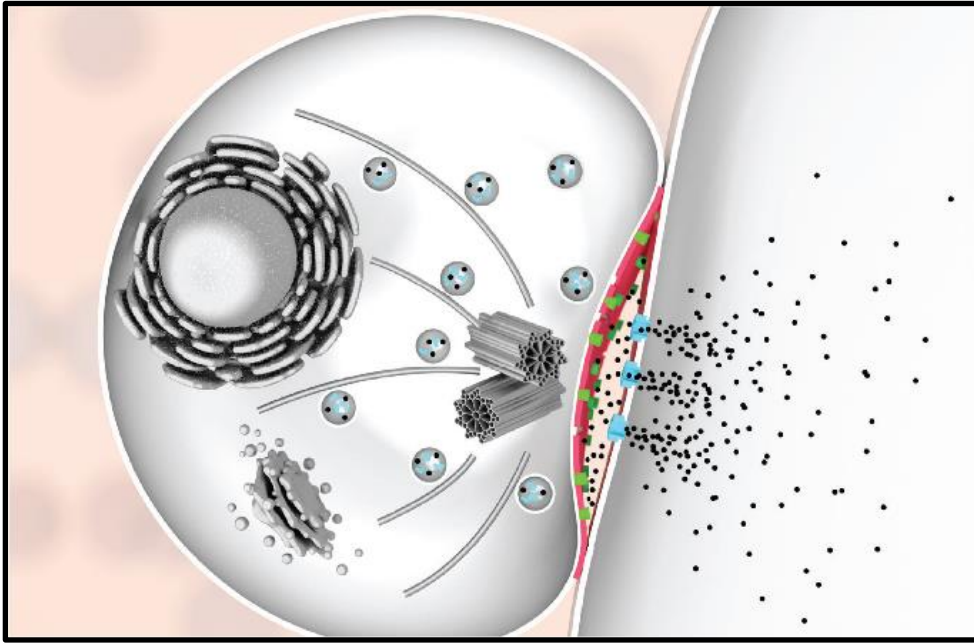


**Figure 6.1: “Mechanism of cytotoxic lymphocyte protection from secreted perforin.**

Illustration of a cytotoxic lymphocyte forming an immune synapse (shown are the microtubule-organizing centre and cytotoxic granule polarization), with granzymes (black dots) entering the target cells through perforin pores (light blue) in the target cell plasma membrane. High lipid order domains (red) and exposed phosphatidylserine (green) at the immunological synapse protect the lymphocyte against the perforin it secretes.” *\*Image created by Dr Adrian Hodel and reproduced from (Rudd-Schmidt et al., 2019)*

## **6.2 Future Directions**

In the current study we have identified the importance of membrane lipid order and charge in the resistance of CTLs to recombinant perforin, and extended the study to show that these lipid properties are highly relevant to the physiologically-relevant protection of CTLs during synapse formation. However, we are yet to directly visualise these protective mechanisms at play within the immune synapse, largely due to technical limitations. The immune synapse occupies a very small area, making direct visualisation of perforin/plasma membrane interaction a difficult task. Standard confocal microscopy suffers from the trade-offs that must be made between temporal and spatial resolution, and high-resolution TEM suffers from the sacrifice of all temporal information for high spatial resolution. One avenue we are currently pursuing is the usage of Lattice Light Sheet microscopy. This technology can provide detailed x-y-z resolution in combination with far superior temporal resolution (up to 1 entire volume containing a CTL/target cell immune synapse interaction per second). This form of microscopy has already been used successfully to image CTL synapses (Chen et al., 2014; Ritter et al., 2015), and work has been begun with our collaborators to replicate these experimental systems with the addition of exogenous annexin V as a marker of PS exposure.

The overarching experimental goal in further testing the findings in this thesis is to reach a point where we can sensitise CTLs to their own perforin, without affecting their ability to form a functional synapse. As high order lipid rafts play a central role in T cell signalling, it becomes difficult to reduce membrane order without affecting synapse formation. However, it may be possible to overcome this issue by utilising Antibody Dependent Cellular Cytotoxicity (ADCC). Experiments are already ongoing in our laboratory where CD20 expressing B cells are labelled with Rituximab, allowing them to be targeted by NK cells, and mimicking the mechanism by which patients' leukaemia and lymphoma cells are killed clinically (Salles et al., 2017). As this synapse may be formed differently to a conventional immune synapse, it may be less reliant on lipid-raft enabled signalling, but still provide directional release of perforin. In this way it may be feasible to reduce membrane order using 7KC before synapse formation, and then observe the effect on self-protection, which one would expect to be disrupted. Of course, the secondary protective mechanism of PS exposure by CTLs may also provide some redundancy to the high membrane order 'shield', a further factor to consider in these experiments.

Our current findings suggest that variations in membrane lipid composition might enable transformed cells to resist CTL attack, either constitutively, or in the context of cancer immunotherapy. Indeed, CTL attack may inadvertently select for such variants. The development of cancer immunotherapies has been one of the most exciting breakthroughs in cancer treatments, and has quickly been established as a new pillar of treatment. However, despite success in treatment of some blood cancers with CAR T cells (Maude et al., 2014; Porter et al., 2015) treatment of solid tumours had been relatively unsuccessful (Long et al., 2018). Checkpoint blockade has also provided very promising results in some, but not all cancers (Ribas & Wolchok, 2018). With very high membrane order (Guo et al., 2014; Rysman et al., 2010) and PS exposure (Riedl et al., 2011) already noted to be features of several cancer cell types, a marker that differentiates tumours based on their membrane properties may

be a therapeutically useful reagent. Given that TMH1-GFP-PRF can be used to measure perforin binding without inducing pore formation, TMH1-GFP-PRF identifies itself as a potential marker of tumour cells that may be resistant to perforin. Interpreting these results would need to take into account the ability of PS to bind and inactivate perforin, even on membranes that otherwise bind little perforin. Thus, TMH1-GFP-PRF binding as a single bio-marker may not directly correlate with target cell susceptibility. Therefore, a specifically designed screen combining TMH1-GFP-PRF and Annexin V to assess both lipid order *and* charge, may have more success as a diagnostic marker. Such an assessment could help inform treatment options appropriate for individual patients, based on how susceptible their tumour may be to perforin-dependent cytotoxic lymphocyte killing.

Potential therapeutic options to target both lipid order and charge are currently available and are being trialled in other contexts. Omega 3 fatty acids are already being considered as adjuvant therapies for cancer (Serini et al., 2016) and, as discussed in Chapter 5, antibodies targeting PS are already undergoing clinical trials. Our current study suggests these therapeutic approaches may have a lot to offer for sensitising tumour cells for targeting by immunotherapy. A whole genome CRISPR screen to determine the genes involved in perforin resistance, similar to those conducted to determine critical drivers for tumour cell resistance to CTL killing (Kearney et al., 2018) might also be used to identify targets for genetic modification to sensitise cells to immunotherapy.



## Bibliography:

- Allbritton, N. L., Verret, C. R., Wolley, R. C., & Eisen, H. N. (1988). Calcium ion concentrations and DNA fragmentation in target cell destruction by murine cloned cytotoxic T lymphocytes. *The Journal of Experimental Medicine*, 167(2), 514-527. doi:10.1084/jem.167.2.514
- Antia, R., Schlegel, R. A., & Williamson, P. (1992). Binding of perforin to membranes is sensitive to lipid spacing and not headgroup. *Immunology Letters*, 32(2), 153-157. doi:[https://doi.org/10.1016/0165-2478\(92\)90108-Z](https://doi.org/10.1016/0165-2478(92)90108-Z)
- Aron, M., Browning, R., Carugo, D., Sezgin, E., Bernardino de la Serna, J., Eggeling, C., & Stride, E. (2017). Spectral imaging toolbox: segmentation, hyperstack reconstruction, and batch processing of spectral images for the determination of cell and model membrane lipid order. *BMC bioinformatics*, 18(1), 254-254. doi:10.1186/s12859-017-1656-2
- Bagatoll, L. A., Parasassi, T., Fidelio, G. D., & Gratton, E. (1999). A Model for the Interaction of 6-Lauroyl-2-(N,N-dimethylamino)naphthalene with Lipid Environments: Implications for Spectral Properties. *Photochemistry and Photobiology*, 70(4), 557-564. doi:10.1111/j.1751-1097.1999.tb08251.x
- Bagatolli, L. A., Gratton, E., & Fidelio, G. D. (1998). Water Dynamics in Glycosphingolipid Aggregates Studied by LAURDAN Fluorescence. *Biophysical journal*, 75(1), 331-341. doi:[https://doi.org/10.1016/S0006-3495\(98\)77517-4](https://doi.org/10.1016/S0006-3495(98)77517-4)
- Balaji, K. N., Schaschke, N., Machleidt, W., Catalfamo, M., & Henkart, P. A. (2002). Surface cathepsin B protects cytotoxic lymphocytes from self-destruction after degranulation. *The Journal of Experimental Medicine*, 196(4), 493-503. doi:10.1084/jem.20011836
- Baran, K., Ciccone, A., Peters, C., Yagita, H., Bird, P. I., Villadangos, J. A., & Trapani, J. A. (2006). Cytotoxic T Lymphocytes from Cathepsin B-deficient Mice Survive Normally in Vitro and in Vivo after Encountering and Killing Target Cells. *Journal of Biological Chemistry*, 281(41), 30485-30491. Retrieved from <http://www.jbc.org/content/281/41/30485.abstract>
- Belzile, O., Huang, X., Gong, J., Carlson, J., Schroit, A. J., Brekken, R. A., & Freimark, B. D. (2018). Antibody targeting of phosphatidylserine for the detection and immunotherapy of cancer. *ImmunoTargets and therapy*, 7, 1-14. doi:10.2147/ITT.S134834
- Berke, G., Sullivan, K. A., & Amos, D. B. (1972). Tumor Immunity in vitro: Destruction of a Mouse Ascites Tumor through a Cycling Pathway. *Science*, 177(4047), 433. doi:10.1126/science.177.4047.433
- Birge, R. B., Boeltz, S., Kumar, S., Carlson, J., Wanderley, J., Calianese, D., . . . Herrmann, M. (2016). Phosphatidylserine is a global immunosuppressive signal in efferocytosis, infectious disease, and cancer. *Cell Death & Differentiation*, 23(6), 962-978. doi:10.1038/cdd.2016.11
- Blakely, A., Gorman, K., Ostergaard, H., Svoboda, K., Liu, C. C., Young, J. D., & Clark, W. R. (1987). Resistance of cloned cytotoxic T lymphocytes to cell-mediated cytotoxicity. *The Journal of Experimental Medicine*, 166(4), 1070-1083. doi:10.1084/jem.166.4.1070
- Blanco, A., & Blanco, G. (2017). Chapter 5 - Lipids. In A. Blanco & G. Blanco (Eds.), *Medical Biochemistry* (pp. 99-119): Academic Press.
- Bocharov, G., Argilaguet, J., & Meyerhans, A. (2015). Understanding experimental LCMV infection of mice: the role of mathematical models. *Journal of Immunology Research*, 2015.
- Brennan, Amelia J., Chia, J., Browne, Kylie A., Ciccone, A., Ellis, S., Lopez, Jamie A., . . . Voskoboinik, I. (2011). Protection from Endogenous Perforin: Glycans and the C Terminus Regulate Exocytic Trafficking in Cytotoxic Lymphocytes. *Immunity*, 34(6), 879-892. doi:<https://doi.org/10.1016/j.immuni.2011.04.007>
- Burack, W. R., Lee, K.-H., Holdorf, A. D., Dustin, M. L., & Shaw, A. S. (2002). Cutting Edge: Quantitative Imaging of Raft Accumulation in the Immunological Synapse. *The Journal of Immunology*, 169(6), 2837. doi:10.4049/jimmunol.169.6.2837
- Chaplin, D. D. (2010). Overview of the immune response. *Journal of Allergy and Clinical Immunology*, 125(2, Supplement 2), S3-S23. doi:<https://doi.org/10.1016/j.jaci.2009.12.980>

- Chaudhry, M. S., Gilmour, K. C., House, I. G., Layton, M., Panoskaltsis, N., Sohal, M., . . . Voskoboinik, I. (2016). Missense mutations in the perforin (PRF1) gene as a cause of hereditary cancer predisposition. *Oncoimmunology*, *5*(7), e1179415-e1179415. doi:10.1080/2162402X.2016.1179415
- Chen, B.-C., Legant, W. R., Wang, K., Shao, L., Milkie, D. E., Davidson, M. W., . . . Betzig, E. (2014). Lattice light-sheet microscopy: Imaging molecules to embryos at high spatiotemporal resolution. *Science*, *346*(6208), 1257998. doi:10.1126/science.1257998
- Chia, J., Yeo, K. P., Whisstock, J. C., Dunstone, M. A., Trapani, J. A., & Voskoboinik, I. (2009). Temperature sensitivity of human perforin mutants unmasks subtotal loss of cytotoxicity, delayed FHL, and a predisposition to cancer. *Proceedings of the National Academy of Sciences*, *106*(24), 9809. doi:10.1073/pnas.0903815106
- Chowdhury, D., & Lieberman, J. (2008). Death by a thousand cuts: granzyme pathways of programmed cell death. *Annual review of immunology*, *26*, 389-420. doi:10.1146/annurev.immunol.26.021607.090404
- Cohnen, A., Chiang, S. C., Stojanovic, A., Schmidt, H., Claus, M., Saftig, P., . . . Watzl, C. (2013). Surface CD107a/LAMP-1 protects natural killer cells from degranulation-associated damage. *Blood*, *122*(8), 1411-1418. doi:10.1182/blood-2012-07-441832
- Connell, S. D., Heath, G., Olmsted, P. D., & Kisil, A. (2013). Critical point fluctuations in supported lipid membranes. *Faraday Discussions*, *161*(0), 91-111. doi:10.1039/C2FD20119D
- Côte, M., Ménager, M. M., Burgess, A., Mahlaoui, N., Picard, C., Schaffner, C., . . . de Saint Basile, G. (2009). Munc18-2 deficiency causes familial hemophagocytic lymphohistiocytosis type 5 and impairs cytotoxic granule exocytosis in patient NK cells. *The Journal of clinical investigation*, *119*(12), 3765-3773. doi:10.1172/JCI40732
- Cullen, S. P., Adrain, C., Lüthi, A. U., Duriez, P. J., & Martin, S. J. (2007). Human and murine granzyme B exhibit divergent substrate preferences. *The Journal of Cell Biology*, *176*(4), 435-444. doi:10.1083/jcb.200612025
- Das, C., Sheikh, K. H., Olmsted, P. D., & Connell, S. D. (2010). Nanoscale mechanical probing of supported lipid bilayers with atomic force microscopy. *Physical Review E*, *82*(4), 041920. doi:10.1103/PhysRevE.82.041920
- Davis, H. W., Vallabhapurapu, S. D., Chu, Z., Vallabhapurapu, S. L., Franco, R. S., Mierzwa, M., . . . Qi, X. (2019). Enhanced phosphatidylserine-selective cancer therapy with irradiation and SapC-DOPS nanovesicles. *Oncotarget*, *10*(8), 856-868. doi:10.18632/oncotarget.26615
- De, M., Ghosh, S., Sen, T., Shadab, M., Banerjee, I., Basu, S., & Ali, N. (2018). A Novel Therapeutic Strategy for Cancer Using Phosphatidylserine Targeting Stearylamine-Bearing Cationic Liposomes. *Molecular therapy. Nucleic acids*, *10*, 9-27. doi:10.1016/j.omtn.2017.10.019
- de Saint Basile, G., Ménasché, G., & Fischer, A. (2010). Molecular mechanisms of biogenesis and exocytosis of cytotoxic granules. *Nature Reviews Immunology*, *10*(8), 568-579. doi:10.1038/nri2803
- Dempsey, P. W., Vaidya, S. A., & Cheng, G. (2003). The Art of War: Innate and adaptive immune responses. *Cellular and Molecular Life Sciences CMLS*, *60*(12), 2604-2621. doi:10.1007/s00018-003-3180-y
- Dillon, S. R., Mancini, M., Rosen, A., & Schlissel, M. S. (2000). Annexin V Binds to Viable B Cells and Colocalizes with a Marker of Lipid Rafts upon B Cell Receptor Activation. *The Journal of Immunology*, *164*(3), 1322. doi:10.4049/jimmunol.164.3.1322
- Dranoff, G. (2004). Cytokines in cancer pathogenesis and cancer therapy. *Nature Reviews Cancer*, *4*(1), 11-22. doi:10.1038/nrc1252
- Dunn, G. P., Bruce, A. T., Ikeda, H., Old, L. J., & Schreiber, R. D. (2002). Cancer immunoediting: from immunosurveillance to tumor escape. *Nature Immunology*, *3*(11), 991-998. doi:10.1038/ni1102-991

- Elliott, J. I., Surprenant, A., Marelli-Berg, F. M., Cooper, J. C., Cassady-Cain, R. L., Wooding, C., . . . Higgins, C. F. (2005). Membrane phosphatidylserine distribution as a non-apoptotic signalling mechanism in lymphocytes. *Nature Cell Biology*, *7*(8), 808-816. doi:10.1038/ncb1279
- Erazo-Oliveras, A., Fuentes, N. R., Wright, R. C., & Chapkin, R. S. (2018). Functional link between plasma membrane spatiotemporal dynamics, cancer biology, and dietary membrane-altering agents. *Cancer and Metastasis Reviews*, *37*(2), 519-544. doi:10.1007/s10555-018-9733-1
- Feldmann, J., Callebaut, I., Raposo, G., Certain, S., Bacq, D., Dumont, C., . . . de Saint Basile, G. (2003). Munc13-4 Is Essential for Cytolytic Granules Fusion and Is Mutated in a Form of Familial Hemophagocytic Lymphohistiocytosis (FHL3). *Cell*, *115*(4), 461-473. doi:[https://doi.org/10.1016/S0092-8674\(03\)00855-9](https://doi.org/10.1016/S0092-8674(03)00855-9)
- Fischer, K., Voelkl, S., Berger, J., Andreesen, R., Pomorski, T., & Mackensen, A. (2006). Antigen recognition induces phosphatidylserine exposure on the cell surface of human CD8+ T cells. *Blood*, *108*(13), 4094-4101. doi:10.1182/blood-2006-03-011742
- Fukuda, M. (1991). Lysosomal membrane glycoproteins. Structure, biosynthesis, and intracellular trafficking. *Journal of Biological Chemistry*, *266*(32), 21327-21330. Retrieved from <http://www.jbc.org/content/266/32/21327.short>
- Garrido, F., Aptsiauri, N., Doorduijn, E. M., Garcia Lora, A. M., & van Hall, T. (2016). The urgent need to recover MHC class I in cancers for effective immunotherapy. *Current opinion in immunology*, *39*, 44-51. doi:10.1016/j.coi.2015.12.007
- Gaus, K., Chklovskaya, E., Fazekas de St Groth, B., Jessup, W., & Harder, T. (2005). Condensation of the plasma membrane at the site of T lymphocyte activation. *The Journal of Cell Biology*, *171*(1), 121-131. doi:10.1083/jcb.200505047
- Gaus, K., Zech, T., & Harder, T. (2006). Visualizing membrane microdomains by Laurdan 2-photon microscopy (Review). *Molecular Membrane Biology*, *23*(1), 41-48. doi:10.1080/09687860500466857
- Geiger, B., Rosen, D., & Berke, G. (1982). Spatial relationships of microtubule-organizing centers and the contact area of cytotoxic T lymphocytes and target cells. *The Journal of Cell Biology*, *95*(1), 137-143. doi:10.1083/jcb.95.1.137
- Germain, R. N. (1994). MHC-dependent antigen processing and peptide presentation: Providing ligands for T lymphocyte activation. *Cell*, *76*(2), 287-299. doi:[https://doi.org/10.1016/0092-8674\(94\)90336-0](https://doi.org/10.1016/0092-8674(94)90336-0)
- Goebel, J., Forrest, K., Flynn, D., Rao, R., & Roszman, T. L. (2002). Lipid rafts, major histocompatibility complex molecules, and immune regulation. *Human Immunology*, *63*(10), 813-820. doi:[https://doi.org/10.1016/S0198-8859\(02\)00458-5](https://doi.org/10.1016/S0198-8859(02)00458-5)
- Golstein, P. (1974). Sensitivity of cytotoxic T cells to T-cell mediated cytotoxicity. *Nature*, *252*(5478), 81-83. doi:10.1038/252081a0
- Gray, M. J., Gong, J., Hatch, M. M. S., Nguyen, V., Hughes, C. C. W., Hutchins, J. T., & Freemark, B. D. (2016). Phosphatidylserine-targeting antibodies augment the anti-tumorigenic activity of anti-PD-1 therapy by enhancing immune activation and downregulating pro-oncogenic factors induced by T-cell checkpoint inhibition in murine triple-negative breast cancers. *Breast Cancer Research*, *18*(1), 50. doi:10.1186/s13058-016-0708-2
- Guo, S., Wang, Y., Zhou, D., & Li, Z. (2014). Significantly increased monounsaturated lipids relative to polyunsaturated lipids in six types of cancer microenvironment are observed by mass spectrometry imaging. *Scientific Reports*, *4*(1), 5959. doi:10.1038/srep05959
- Halle, S., Keyser, K. A., Stahl, F. R., Busche, A., Marquardt, A., Zheng, X., . . . Förster, R. (2016). In Vivo Killing Capacity of Cytotoxic T Cells Is Limited and Involves Dynamic Interactions and T Cell Cooperativity. *Immunity*, *44*(2), 233-245. doi:<https://doi.org/10.1016/j.immuni.2016.01.010>
- Hammond, A. T., Heberle, F. A., Baumgart, T., Holowka, D., Baird, B., & Feigenson, G. W. (2005). Crosslinking a lipid raft component triggers liquid ordered-liquid disordered phase separation in model plasma membranes. *Proceedings of the National Academy of Sciences of the United States of America*, *102*(18), 6320-6325. doi:10.1073/pnas.0405654102

- Henter, J. I., Elinder, G., Soder, O., Hansson, M., Andersson, B., & Andersson, U. (1991). Hypercytokinemia in familial hemophagocytic lymphohistiocytosis. *Blood*, *78*(11), 2918-2922. doi:10.1182/blood.V78.11.2918.2918
- Hope, M. J., Bally, M. B., Webb, G., & Cullis, P. R. (1985). Production of large unilamellar vesicles by a rapid extrusion procedure. Characterization of size distribution, trapped volume and ability to maintain a membrane potential. *Biochimica et Biophysica Acta (BBA) - Biomembranes*, *812*(1), 55-65. doi:[https://doi.org/10.1016/0005-2736\(85\)90521-8](https://doi.org/10.1016/0005-2736(85)90521-8)
- House, I. G., House, C. M., Brennan, A. J., Gilan, O., Dawson, M. A., Whisstock, J. C., . . . Voskoboinik, I. (2017). Regulation of perforin activation and pre-synaptic toxicity through C-terminal glycosylation. *EMBO reports*, *18*(10), 1775-1785. doi:10.15252/embr.201744351
- Jenkins, M. R., Rudd-Schmidt, J. A., Lopez, J. A., Ramsbottom, K. M., Mannering, S. I., Andrews, D. M., . . . Trapani, J. A. (2015). Failed CTL/NK cell killing and cytokine hypersecretion are directly linked through prolonged synapse time. *Journal of Experimental Medicine*, *212*(3), 307-317. doi:10.1084/jem.20140964
- Jiang, S., Ojcius, D. M., & Young, J. D. E. (1990). Perforin binding to cells and lipid membranes determined by a simple competition assay. *Journal of Immunological Methods*, *126*(1), 29-37. doi:[https://doi.org/10.1016/0022-1759\(90\)90008-J](https://doi.org/10.1016/0022-1759(90)90008-J)
- Jiang, S. B., Persechini, P. M., Zychlinsky, A., Liu, C. C., Perussia, B., & Young, J. D. (1988). Resistance of cytolytic lymphocytes to perforin-mediated killing. Lack of correlation with complement-associated homologous species restriction. *The Journal of Experimental Medicine*, *168*(6), 2207-2219. doi:10.1084/jem.168.6.2207
- Kaech, S., Wherry, E. J., & Ahmed, R. (2002). Kaech, S.M., Wherry, E.J. & Ahmed, R. Effector and memory T-cell differentiation: implications for vaccine development. *Nat. Rev. Immunol.* *2*, 251-262. *Nature reviews. Immunology*, *2*, 251-262. doi:10.1038/nri778
- Kearney, C. J., Vervoort, S. J., Hogg, S. J., Ramsbottom, K. M., Freeman, A. J., Lalaoui, N., . . . Oliaro, J. (2018). Tumor immune evasion arises through loss of TNF sensitivity. *Science Immunology*, *3*(23), eaar3451. doi:10.1126/sciimmunol.aar3451
- Koopman, G., Reutelingsperger, C. P., Kuijten, G. A., Keehnen, R. M., Pals, S. T., & van Oers, M. H. (1994). Annexin V for flow cytometric detection of phosphatidylserine expression on B cells undergoing apoptosis. *Blood*, *84*(5), 1415-1420. doi:10.1182/blood.V84.5.1415.1415
- Kremer, J. R., Mastrorarde, D. N., & McIntosh, J. R. (1996). Computer Visualization of Three-Dimensional Image Data Using IMOD. *Journal of Structural Biology*, *116*(1), 71-76. doi:<https://doi.org/10.1006/jsbi.1996.0013>
- Kupfer, A., & Dennert, G. (1984). Reorientation of the microtubule-organizing center and the Golgi apparatus in cloned cytotoxic lymphocytes triggered by binding to lysable target cells. *The Journal of Immunology*, *133*(5), 2762. Retrieved from <http://www.jimmunol.org/content/133/5/2762.abstract>
- Law, R. H. P., Lukyanova, N., Voskoboinik, I., Caradoc-Davies, T. T., Baran, K., Dunstone, M. A., . . . Whisstock, J. C. (2010). The structural basis for membrane binding and pore formation by lymphocyte perforin. *Nature*, *468*(7322), 447-451. doi:10.1038/nature09518
- Lehmann, C., Zeis, M., Schmitz, N., & Uharek, L. (2000). Impaired binding of perforin on the surface of tumor cells is a cause of target cell resistance against cytotoxic effector cells. *Blood*, *96*(2), 594-600. doi:10.1182/blood.V96.2.594
- Leung, C., Hodel, A. W., Brennan, A. J., Lukyanova, N., Tran, S., House, C. M., . . . Hoogenboom, B. W. (2017). Real-time visualization of perforin nanopore assembly. *Nature Nanotechnology*, *12*(5), 467-473. doi:10.1038/nnano.2016.303
- Leventis, P. A., & Grinstein, S. (2010). The Distribution and Function of Phosphatidylserine in Cellular Membranes. *Annual Review of Biophysics*, *39*(1), 407-427. doi:10.1146/annurev.biophys.093008.131234

- Ljunggren, H.-G., & Kärre, K. (1990). In search of the 'missing self': MHC molecules and NK cell recognition. *Immunology Today*, *11*, 237-244. doi:[https://doi.org/10.1016/0167-5699\(90\)90097-S](https://doi.org/10.1016/0167-5699(90)90097-S)
- Long, K. B., Young, R. M., Boesteanu, A. C., Davis, M. M., Melenhorst, J. J., Lacey, S. F., . . . Fraietta, J. A. (2018). CAR T Cell Therapy of Non-hematopoietic Malignancies: Detours on the Road to Clinical Success. *Frontiers in immunology*, *9*, 2740. Retrieved from <https://www.frontiersin.org/article/10.3389/fimmu.2018.02740>
- Lopez, J. A., Brennan, A. J., Whisstock, J. C., Voskoboinik, I., & Trapani, J. A. (2012). Protecting a serial killer: pathways for perforin trafficking and self-defence ensure sequential target cell death. *Trends in Immunology*, *33*(8), 406-412. doi:<https://doi.org/10.1016/j.it.2012.04.001>
- Lopez, J. A., Jenkins, M. R., Rudd-Schmidt, J. A., Brennan, A. J., Danne, J. C., Mannering, S. I., . . . Voskoboinik, I. (2013). Rapid and Unidirectional Perforin Pore Delivery at the Cytotoxic Immune Synapse. *The Journal of Immunology*, *191*(5), 2328. doi:10.4049/jimmunol.1301205
- Lopez, J. A., Susanto, O., Jenkins, M. R., Lukoyanova, N., Sutton, V. R., Law, R. H. P., . . . Voskoboinik, I. (2013). Perforin forms transient pores on the target cell plasma membrane to facilitate rapid access of granzymes during killer cell attack. *Blood*, *121*(14), 2659-2668. doi:10.1182/blood-2012-07-446146
- Lowin, B., Hahne, M., Mattmann, C., & Tschopp, J. (1994). Cytolytic T-cell cytotoxicity is mediated through perforin and Fas lytic pathways. *Nature*, *370*(6491), 650-652. doi:10.1038/370650a0
- Lukoyanova, N., Hoogenboom, B. W., & Saibil, H. R. (2016). The membrane attack complex, perforin and cholesterol-dependent cytolysin superfamily of pore-forming proteins. *Journal of Cell Science*, *129*(11), 2125. doi:10.1242/jcs.182741
- Lynch, D. H., Ramsdell, F., & Alderson, M. R. (1995). Fas and FasL in the homeostatic regulation of immune responses. *Immunology Today*, *16*(12), 569-574. doi:[https://doi.org/10.1016/0167-5699\(95\)80079-4](https://doi.org/10.1016/0167-5699(95)80079-4)
- Ma, Y., Poole, K., Goyette, J., & Gaus, K. (2017). Introducing Membrane Charge and Membrane Potential to T Cell Signaling. *Frontiers in immunology*, *8*, 1513. Retrieved from <https://www.frontiersin.org/article/10.3389/fimmu.2017.01513>
- Marsh, M., Schmid, S., Kern, H., Harms, E., Male, P., Mellman, I., & Helenius, A. (1987). Rapid analytical and preparative isolation of functional endosomes by free flow electrophoresis. *Journal of Cell Biology*, *104*(4), 875-886. doi:10.1083/jcb.104.4.875
- Massey, J. B., & Pownall, H. J. (2005). The Polar Nature of 7-Ketocholesterol Determines Its Location within Membrane Domains and the Kinetics of Membrane Microsolubilization by Apolipoprotein A-I. *Biochemistry*, *44*(30), 10423-10433. doi:10.1021/bi0506425
- Maude, S. L., Frey, N., Shaw, P. A., Aplenc, R., Barrett, D. M., Bunin, N. J., . . . Grupp, S. A. (2014). Chimeric Antigen Receptor T Cells for Sustained Remissions in Leukemia. *New England Journal of Medicine*, *371*(16), 1507-1517. doi:10.1056/NEJMoa1407222
- Mellman, I., Coukos, G., & Dranoff, G. (2011). Cancer immunotherapy comes of age. *Nature*, *480*(7378), 480-489. doi:10.1038/nature10673
- Metkar, S. S., Aguilar-Santelises, M., Wang, B., & Froelich, C. J. (2001). Flow cytometry cannot assess surface binding of perforin to target cells. *Blood*, *97*(7), 2181-2183. doi:10.1182/blood.V97.7.2181
- Metkar, S. S., Marchioretto, M., Antonini, V., Lunelli, L., Wang, B., Gilbert, R. J. C., . . . Froelich, C. J. (2015). Perforin oligomers form arcs in cellular membranes: a locus for intracellular delivery of granzymes. *Cell death and differentiation*, *22*(1), 74-85. doi:10.1038/cdd.2014.110
- Metkar, S. S., Wang, B., Catalan, E., Anderluh, G., Gilbert, R. J. C., Pardo, J., & Froelich, C. J. (2011). Perforin rapidly induces plasma membrane phospholipid flip-flop. *PLOS ONE*, *6*(9), e24286-e24286. doi:10.1371/journal.pone.0024286
- Metzler, R., Jeon, J. H., & Cherstvy, A. G. (2016). Non-Brownian diffusion in lipid membranes: Experiments and simulations. *Biochimica et Biophysica Acta (BBA) - Biomembranes*, *1858*(10), 2451-2467. doi:<https://doi.org/10.1016/j.bbamem.2016.01.022>



- Meyer, J. A., Yull; Anandam, Joselin; Karri, Sirisha; Syed, Samira; Verma, Udit; Abdelnaby, Abier; Raja, Grace; Dong, Ying; Shaalan Beg, Muhammad; Balch, Glen. (2018). A Phase I Clinical Trial of the Phosphatidylserine-targeting Antibody Baviximab in Combination With Radiation Therapy and Capecitabine in the Preoperative Treatment of Rectal Adenocarcinoma. *American Journal of Clinical Oncology*, 41(10), 972-976.
- Miguel, L., Owen, D. M., Lim, C., Liebig, C., Evans, J., Magee, A. I., & Jury, E. C. (2011). Primary Human CD4+ T Cells Have Diverse Levels of Membrane Lipid Order That Correlate with Their Function. *The Journal of Immunology*, 186(6), 3505. doi:10.4049/jimmunol.1002980
- Morrison, B. J., Steel, J. C., & Morris, J. C. (2018). Reduction of MHC-I expression limits T-lymphocyte-mediated killing of Cancer-initiating cells. *BMC Cancer*, 18(1), 469. doi:10.1186/s12885-018-4389-3
- Müller, C., & Tschopp, J. (1994). Resistance of CTL to perforin-mediated lysis. Evidence for a lymphocyte membrane protein interacting with perforin. *The Journal of Immunology*, 153(6), 2470. Retrieved from <http://www.jimmunol.org/content/153/6/2470.abstract>
- N'Guessan, K. F., Patel, P. H., & Qi, X. (2020). SapC-DOPS – a Phosphatidylserine-targeted Nanovesicle for selective Cancer therapy. *Cell Communication and Signaling*, 18(1), 6. doi:10.1186/s12964-019-0476-6
- Ohadi, M., Lalloz, M. R., Sham, P., Zhao, J., Dearlove, A. M., Shiach, C., . . . Layton, D. M. (1999). Localization of a gene for familial hemophagocytic lymphohistiocytosis at chromosome 9q21.3-22 by homozygosity mapping. *American journal of human genetics*, 64(1), 165-171. doi:10.1086/302187
- Ojcus, D. M., Jiang, S., Persechini, P. M., Storch, J., & Young, J. D.-E. (1990). Resistance to the pore-forming protein of cytotoxic T cells: Comparison of target cell membrane rigidity. *Molecular Immunology*, 27(9), 839-845. doi:[https://doi.org/10.1016/0161-5890\(90\)90149-T](https://doi.org/10.1016/0161-5890(90)90149-T)
- Owen, D. M., Oddos, S., Kumar, S., Davis, D. M., Neil, M. A. A., French, P. M. W., . . . Cebeckauer, M. (2010). High plasma membrane lipid order imaged at the immunological synapse periphery in live T cells. *Molecular Membrane Biology*, 27(4-6), 178-189. doi:10.3109/09687688.2010.495353
- Owen, D. M., Rentero, C., Magenau, A., Abu-Siniyeh, A., & Gaus, K. (2012). Quantitative imaging of membrane lipid order in cells and organisms. *Nature Protocols*, 7(1), 24-35. doi:10.1038/nprot.2011.419
- Parkin, J., & Cohen, B. (2001). An overview of the immune system. *The Lancet*, 357(9270), 1777-1789. doi:[https://doi.org/10.1016/S0140-6736\(00\)04904-7](https://doi.org/10.1016/S0140-6736(00)04904-7)
- Paul, William E. (2011). Bridging Innate and Adaptive Immunity. *Cell*, 147(6), 1212-1215. doi:<https://doi.org/10.1016/j.cell.2011.11.036>
- Pham, K., Shimoni, R., Charnley, M., Ludford-Menting, M. J., Hawkins, E. D., Ramsbottom, K., . . . Russell, S. M. (2015). Asymmetric cell division during T cell development controls downstream fate. *The Journal of Cell Biology*, 210(6), 933-950. doi:10.1083/jcb.201502053
- Porter, D. L., Hwang, W.-T., Frey, N. V., Lacey, S. F., Shaw, P. A., Loren, A. W., . . . June, C. H. (2015). Chimeric antigen receptor T cells persist and induce sustained remissions in relapsed refractory chronic lymphocytic leukemia. *Science Translational Medicine*, 7(303), 303ra139. doi:10.1126/scitranslmed.aac5415
- Praper, T., Beseničar, M. P., Istinič, H., Podlesek, Z., Metkar, S. S., Froelich, C. J., & Anderluh, G. (2010). Human perforin permeabilizing activity, but not binding to lipid membranes, is affected by pH. *Molecular Immunology*, 47(15), 2492-2504. doi:<https://doi.org/10.1016/j.molimm.2010.06.001>
- Praper, T., Sonnen, A., Viero, G., Kladnik, A., Froelich, C. J., Anderluh, G., . . . Gilbert, R. J. C. (2011). Human perforin employs different avenues to damage membranes. *The Journal of biological chemistry*, 286(4), 2946-2955. doi:10.1074/jbc.M110.169417

- Qi, X., Chu, Z., Mahller, Y. Y., Stringer, K. F., Witte, D. P., & Cripe, T. P. (2009). Cancer-Selective Targeting and Cytotoxicity by Liposomal-Coupled Lysosomal Saposin C Protein. *Clinical Cancer Research*, 15(18), 5840. doi:10.1158/1078-0432.CCR-08-3285
- Ran, S., Downes, A., & Thorpe, P. E. (2002). Increased Exposure of Anionic Phospholipids on the Surface of Tumor Blood Vessels. *Cancer Research*, 62(21), 6132. Retrieved from <http://cancerres.aacrjournals.org/content/62/21/6132.abstract>
- Rentero, C., Zech, T., Quinn, C. M., Engelhardt, K., Williamson, D., Grewal, T., . . . Gaus, K. (2008). Functional Implications of Plasma Membrane Condensation for T Cell Activation. *PLOS ONE*, 3(5), e2262. doi:10.1371/journal.pone.0002262
- Ribas, A., & Wolchok, J. D. (2018). Cancer immunotherapy using checkpoint blockade. *Science*, 359(6382), 1350. doi:10.1126/science.aar4060
- Riedl, S., Rinner, B., Asslaber, M., Schaidler, H., Walzer, S., Novak, A., . . . Zweytick, D. (2011). In search of a novel target — Phosphatidylserine exposed by non-apoptotic tumor cells and metastases of malignancies with poor treatment efficacy. *Biochimica et Biophysica Acta (BBA) - Biomembranes*, 1808(11), 2638-2645. doi:<https://doi.org/10.1016/j.bbamem.2011.07.026>
- Ritter, A. T., Asano, Y., Stinchcombe, J. C., Dieckmann, N. M. G., Chen, B.-C., Gawden-Bone, C., . . . Griffiths, G. M. (2015). Actin depletion initiates events leading to granule secretion at the immunological synapse. *Immunity*, 42(5), 864-876. doi:10.1016/j.immuni.2015.04.013
- Rojko, N., & Anderluh, G. (2015). How Lipid Membranes Affect Pore Forming Toxin Activity. *Accounts of Chemical Research*, 48(12), 3073-3079. doi:10.1021/acs.accounts.5b00403
- Rothstein, T. L., Mage, M., Jones, G., & McHugh, L. L. (1978). Cytotoxic T Lymphocyte Sequential Killing of Immobilized Allogeneic Tumor Target Cells Measured by Time-Lapse Microcinematography. *The Journal of Immunology*, 121(5), 1652. Retrieved from <http://www.jimmunol.org/content/121/5/1652.abstract>
- Rudd-Schmidt, J. A., Hodel, A. W., Noori, T., Lopez, J. A., Cho, H.-J., Verschoor, S., . . . Voskoboinik, I. (2019). Lipid order and charge protect killer T cells from accidental death. *Nature Communications*, 10(1), 5396. doi:10.1038/s41467-019-13385-x
- Rysman, E., Brusselmans, K., Scheys, K., Timmermans, L., Derua, R., Munck, S., . . . Swinnen, J. V. (2010). De novo Lipogenesis Protects Cancer Cells from Free Radicals and Chemotherapeutics by Promoting Membrane Lipid Saturation. *Cancer Research*, 70(20), 8117. doi:10.1158/0008-5472.CAN-09-3871
- Salles, G., Barrett, M., Foà, R., Maurer, J., O'Brien, S., Valente, N., . . . Maloney, D. G. (2017). Rituximab in B-Cell Hematologic Malignancies: A Review of 20 Years of Clinical Experience. *Advances in Therapy*, 34(10), 2232-2273. doi:10.1007/s12325-017-0612-x
- Schenborn, E. T., & Goiffon, V. (2000). Calcium Phosphate Transfection of Mammalian Cultured Cells. In M. J. Tymms (Ed.), *Transcription Factor Protocols* (pp. 135-145). Totowa, NJ: Humana Press.
- Schindelin, J., Arganda-Carreras, I., Frise, E., Kaynig, V., Longair, M., Pietzsch, T., . . . Cardona, A. (2012). Fiji: an open-source platform for biological-image analysis. *Nature Methods*, 9(7), 676-682. doi:10.1038/nmeth.2019
- Seedhom, M. O., Jellison, E. R., Daniels, K. A., & Welsh, R. M. (2009). High frequencies of virus-specific CD8+ T-cell precursors. *Journal of virology*, 83(24), 12907-12916. doi:10.1128/JVI.01722-09
- Serini, S., Ottens Vasconcelos, R., Fasano, E., & Calviello, G. (2016). How plausible is the use of dietary n-3 PUFA in the adjuvant therapy of cancer? *Nutrition Research Reviews*, 29(1), 102-125. doi:10.1017/S0954422416000044
- Sezgin, E., Waithe, D., Bernardino de la Serna, J., & Eggeling, C. (2015). Spectral Imaging to Measure Heterogeneity in Membrane Lipid Packing. *ChemPhysChem*, 16(7), 1387-1394. doi:10.1002/cphc.201402794
- Shifrin, N., Raulet, D. H., & Ardolino, M. (2014). NK cell self tolerance, responsiveness and missing self recognition. *Seminars in immunology*, 26(2), 138-144. doi:10.1016/j.smim.2014.02.007

- Shinkai, Y., Ishikawa, H., Hattori, M., & Okuimira, K. (1988). Resistance of mouse cytolytic cells to pore-forming protein-mediated cytolysis. *European Journal of Immunology*, *18*(1), 29-33. doi:10.1002/eji.1830180106
- Simons, K., & Vaz, W. L. C. (2004). Model Systems, Lipid Rafts, and Cell Membranes. *Annual Review of Biophysics and Biomolecular Structure*, *33*(1), 269-295. doi:10.1146/annurev.biophys.32.110601.141803
- Sofia Vala, I., Martins, L. R., Imaizumi, N., Nunes, R. J., Rino, J., Kuonen, F., . . . Santos, S. C. R. (2010). Low doses of ionizing radiation promote tumor growth and metastasis by enhancing angiogenesis. *PLOS ONE*, *5*(6), e11222-e11222. doi:10.1371/journal.pone.0011222
- Stepp, S. E., Dufourcq-Lagelouse, R., Deist, F. L., Bhawan, S., Certain, S., Mathew, P. A., . . . Kumar, V. (1999). Perforin Gene Defects in Familial Hemophagocytic Lymphohistiocytosis. *Science*, *286*(5446), 1957. doi:10.1126/science.286.5446.1957
- Stinchcombe, J. C., Majorovits, E., Bossi, G., Fuller, S., & Griffiths, G. M. (2006). Centrosome polarization delivers secretory granules to the immunological synapse. *Nature*, *443*(7110), 462-465. doi:10.1038/nature05071
- Sutton, V. R., Brennan, A. J., Ellis, S., Danne, J., Thia, K., Jenkins, M. R., . . . Trapani, J. A. (2016). Serglycin determines secretory granule repertoire and regulates natural killer cell and cytotoxic T lymphocyte cytotoxicity. *The FEBS Journal*, *283*(5), 947-961. doi:10.1111/febs.13649
- Sutton, V. R., Waterhouse, N. J., Baran, K., Browne, K., Voskoboinik, I., & Trapani, J. A. (2008). Measuring cell death mediated by cytotoxic lymphocytes or their granule effector molecules. *Methods*, *44*(3), 241-249. doi:<https://doi.org/10.1016/j.ymeth.2007.11.011>
- Tavano, R., Gri, G., Molon, B., Marinari, B., Rudd, C. E., Tuosto, L., & Viola, A. (2004). CD28 and Lipid Rafts Coordinate Recruitment of Lck to the Immunological Synapse of Human T Lymphocytes. *The Journal of Immunology*, *173*(9), 5392. doi:10.4049/jimmunol.173.9.5392
- Traore, Daouda A. K., Brennan, Amelia J., Law, Ruby H. P., Dogovski, C., Perugini, Matthew A., Lukoyanova, N., . . . Voskoboinik, I. (2013). Defining the interaction of perforin with calcium and the phospholipid membrane. *Biochemical Journal*, *456*(3), 323-335. doi:10.1042/BJ20130999
- Trapani, J. A., & Smyth, M. J. (2002). Functional significance of the perforin/granzyme cell death pathway. *Nature Reviews Immunology*, *2*(10), 735-747. doi:10.1038/nri911
- Trapani, J. A., Thia, K. Y. T., Andrews, M., Davis, I. D., Gedye, C., Parente, P., . . . Cebon, J. S. (2013). Human perforin mutations and susceptibility to multiple primary cancers. *Oncimmunology*, *2*(4), e24185-e24185. doi:10.4161/onci.24185
- van Meer, G., Voelker, D. R., & Feigenson, G. W. (2008). Membrane lipids: where they are and how they behave. *Nature Reviews Molecular Cell Biology*, *9*(2), 112-124. doi:10.1038/nrm2330
- Veatch, S. L., & Keller, S. L. (2005). Miscibility Phase Diagrams of Giant Vesicles Containing Sphingomyelin. *Physical Review Letters*, *94*(14), 148101. doi:10.1103/PhysRevLett.94.148101
- Verret, C. R., Firmenich, A. A., Kranz, D. M., & Eisen, H. N. (1987). Resistance of cytotoxic T lymphocytes to the lytic effects of their toxic granules. *The Journal of Experimental Medicine*, *166*(5), 1536-1547. doi:10.1084/jem.166.5.1536
- Viola, A., Schroeder, S., Sakakibara, Y., & Lanzavecchia, A. (1999). T Lymphocyte Costimulation Mediated by Reorganization of Membrane Microdomains. *Science*, *283*(5402), 680. doi:10.1126/science.283.5402.680
- Voskoboinik, I., Smyth, M. J., & Trapani, J. A. (2006). Perforin-mediated target-cell death and immune homeostasis. *Nature Reviews Immunology*, *6*(12), 940-952. doi:10.1038/nri1983
- Voskoboinik, I., Thia, M.-C., De Bono, A., Browne, K., Cretney, E., Jackson, J. T., . . . Trapani, J. A. (2004). The Functional Basis for Hemophagocytic Lymphohistiocytosis in a Patient with Co-inherited Missense Mutations in the Perforin (PFN1) Gene. *Journal of Experimental Medicine*, *200*(6), 811-816. doi:10.1084/jem.20040776
- Voskoboinik, I., Thia, M.-C., Fletcher, J., Ciccone, A., Browne, K., Smyth, M. J., & Trapani, J. A. (2005). Calcium-dependent Plasma Membrane Binding and Cell Lysis by Perforin Are Mediated



- through Its C2 Domain: A CRITICAL ROLE FOR ASPARTATE RESIDUES 429, 435, 483, AND 485 BUT NOT 491. *Journal of Biological Chemistry*, 280(9), 8426-8434. Retrieved from <http://www.jbc.org/content/280/9/8426.abstract>
- Voskoboinik, I., & Trapani, J. A. (2013). Perforinopathy: a spectrum of human immune disease caused by defective perforin delivery or function. *Frontiers in immunology*, 4, 441-441. doi:10.3389/fimmu.2013.00441
- Voskoboinik, I., Whisstock, J. C., & Trapani, J. A. (2015). Perforin and granzymes: function, dysfunction and human pathology. *Nature Reviews Immunology*, 15(6), 388-400. doi:10.1038/nri3839
- Waring, P., & Müllbacher, A. (1999). Cell death induced by the Fas/Fas ligand pathway and its role in pathology. *Immunology & Cell Biology*, 77(4), 312-317. doi:10.1046/j.1440-1711.1999.00837.x
- Weninger, W., Manjunath, N., & Von Andrian, U. H. (2002). Migration and differentiation of CD8+ T cells. *Immunological Reviews*, 186(1), 221-233. doi:10.1034/j.1600-065X.2002.18618.x
- Williams, M. A., & Fukuda, M. (1990). Accumulation of membrane glycoproteins in lysosomes requires a tyrosine residue at a particular position in the cytoplasmic tail. *The Journal of Cell Biology*, 111(3), 955-966. doi:10.1083/jcb.111.3.955
- Wodlej, C., Riedl, S., Rinner, B., Leber, R., Drechsler, C., Voelker, D. R., . . . Zweytick, D. (2019). Interaction of two antitumor peptides with membrane lipids – Influence of phosphatidylserine and cholesterol on specificity for melanoma cells. *PLOS ONE*, 14(1), e0211187. doi:10.1371/journal.pone.0211187
- Yagi, H., Conroy, P. J., Leung, E. W. W., Law, R. H. P., Trapani, J. A., Voskoboinik, I., . . . Norton, R. S. (2015). Structural Basis for Ca<sup>2+</sup>-mediated Interaction of the Perforin C2 Domain with Lipid Membranes. *Journal of Biological Chemistry*, 290(42), 25213-25226. Retrieved from <http://www.jbc.org/content/290/42/25213.abstract>
- Young, J. D., Damiano, A., DiNome, M. A., Leong, L. G., & Cohn, Z. A. (1987). Dissociation of membrane binding and lytic activities of the lymphocyte pore-forming protein (perforin). *The Journal of Experimental Medicine*, 165(5), 1371-1382. doi:10.1084/jem.165.5.1371
- Zalman, L. S., Wood, L. M., & Müller-Eberhard, H. J. (1987). Inhibition of antibody-dependent lymphocyte cytotoxicity by homologous restriction factor incorporated into target cell membranes. *The Journal of Experimental Medicine*, 166(4), 947-955. doi:10.1084/jem.166.4.947
- Zech, T., Ejsing, C. S., Gaus, K., de Wet, B., Shevchenko, A., Simons, K., & Harder, T. (2009). Accumulation of raft lipids in T-cell plasma membrane domains engaged in TCR signalling. *The EMBO journal*, 28(5), 466-476. doi:10.1038/emboj.2009.6
- Zohar, D. N., & Shoenfeld, Y. (2018). Antibody targeting of phosphatidylserine for detection and immunotherapy of cancer. *ImmunoTargets and therapy*, 7, 51-53. doi:10.2147/ITT.S169383
- zur Stadt, U., Schmidt, S., Kasper, B., Beutel, K., Diler, A. S., Henter, J.-I., . . . Hennies, H. C. (2005). Linkage of familial hemophagocytic lymphohistiocytosis (FHL) type-4 to chromosome 6q24 and identification of mutations in syntaxin 11. *Human Molecular Genetics*, 14(6), 827-834. doi:10.1093/hmg/ddi076

# Appendix 1: Detailed Atomic Force Microscopy Methods

(Experiments designed and performed by Dr Adrian Hodel)

## “Materials and Methods

### **Lipid vesicle and AFM sample preparation**

1,2-dioleoyl-sn-glycero-3-phosphocholine (DOPC), 1,2-dioleoyl-sn-glycero-3-phospho-L-serine (DOPS), egg SM, cholesterol, and 7KC were purchased from Avanti Polar Lipids (Alabaster, AL, USA) as powder or dissolved in chloroform. The lipids were mixed in the desired molar ratio, and small unilamellar vesicles were prepared using the lipid extrusion method (Leung et al., 2017) (Hope et al., 1985). Indicated lipid ratios and percentages refer to molar values and are given with  $\pm 5\%$  confidence intervals.

A total of 4  $\mu\text{L}$  of the small unilamellar vesicles were injected onto a freshly cleaved mica surface (Agar Scientific, Essex, UK) in the presence of 80  $\mu\text{L}$  of 20mM HEPES, 150mM NaCl, 25mM  $\text{Mg}^{2+}$ , 5mM  $\text{Ca}^{2+}$ , pH 7.4, adsorption buffer. A 30 min incubation above the main transition temperature of the lipids allowed the vesicles to rupture and adsorb onto the mica surface, yielding an extended lipid bilayer film. Excess vesicles were removed by washing the samples at least nine times with 80  $\mu\text{L}$  of the adsorption buffer. Supported lipid bilayers containing DOPS (Figure 5.5) were washed with 20mM HEPES, 150mM NaCl, 5 mM  $\text{Ca}^{2+}$ , pH 7.4, instead of the adsorption buffer to remove  $\text{Mg}^{2+}$  or excess  $\text{Ca}^{2+}$  ions, as they would interfere with perforin binding to the (negatively charged) membranes.

Perforin was diluted up to ca. tenfold in 20mM HEPES, 150mM NaCl and injected onto supported lipid bilayers in the adsorption buffer, leading to a final protein concentration of about 150 nM, and incubated for 5 min at 37 °C. The AFM samples used in Figure 4.7 were incubated for a reduced duration (2 min instead of 5 min) and subsequently washed six times with the adsorption buffer to counteract excessive aggregation on some of the lipid mixtures under study.

For unlocking TMH1 perforin and TMH1-GFP perforin after their binding to the membrane (Figures 4.8 and 5.5), the mutant proteins were incubated with 2mM DTT (Sigma-Aldrich) for 10 min at 37 °C.

Mobile, membrane-bound TMH1-PRF in Fig. 5.5 was fixed by addition of 0.04% glutaraldehyde (TAAB Laboratories, Reading, UK), labelled +GA in the figures) and 10 min incubation at room temperature. The samples were next washed with 20mM HEPES, 150mM NaCl, 5mM  $\text{Ca}^{2+}$ , pH 7.4, prior to AFM imaging.

## AFM imaging and data processing

AFM images were recorded by force-distance curve-based imaging (PeakForce Tapping) on a MultiMode 8 system (Bruker, Santa Barbara, CA, USA). PeakForce Tapping was performed at 2 kHz and a maximum tip-sample separation between 5 and 20 nm. Images were typically recorded at ca. 6 min/frame on an E scanner (Bruker, Santa Barbara, CA, USA) with temperature control. MSNL-E and -F probes (Bruker, Santa Barbara, CA, USA) were used at forces between 50 and 100 pN.

Raw AFM data were processed in NanoScope Analysis software version 1.80 (Bruker, Santa Barbara, CA, USA). AFM images were flattened with respect to the lipid surface, using a height threshold and second-order flattening. Height values indicated in the manuscript are given with  $\pm 1$  nm confidence intervals, with the uncertainty related to both scanner calibration and the possible sample deformation in the AFM images. Values for perforin coverage (Figure 4.7) were estimated by considering the number of pixels above a height threshold, located 6–8 nm above the membrane surface and adjusted to counteract broadening effects of differently shaped AFM tips. The values for perforin coverage obtained by this method are either given as area percentage, or as values between 0 and 1 when normalized with respect to a 100% DOPC reference. In the case of Fig. 5.5c, for which we recorded data at a higher pixel resolution, the perforin coverage was determined by tracing pore shapes with 3dmod 4.9.4 (BL3DEMC & Regents of the University of Colorado, (Kremer et al., 1996)). The traces were normalized with respect to a reference coverage as measured on pure DOPC membranes, resulting in values of coverage between 0 and 1.”


## **Appendix 2: Associated Publication**

ARTICLE

<https://doi.org/10.1038/s41467-019-13385-x>

OPEN

# Lipid order and charge protect killer T cells from accidental death

Jesse A. Rudd-Schmidt<sup>1,2,9</sup>, Adrian W. Hodel<sup>3,4,9</sup>, Tahereh Noori<sup>1</sup>, Jamie A. Lopez<sup>1,8</sup>, Hyun-Jung Cho<sup>5</sup>, Sandra Verschoor<sup>6</sup>, Annette Ciccone<sup>6</sup>, Joseph A. Trapani<sup>2,6</sup>, Bart W. Hoogenboom<sup>3,4,7,10\*</sup>  & Ilia Voskoboinik<sup>1,2,10\*</sup>

Killer T cells (cytotoxic T lymphocytes, CTLs) maintain immune homeostasis by eliminating virus-infected and cancerous cells. CTLs achieve this by forming an immunological synapse with their targets and secreting a pore-forming protein (perforin) and pro-apoptotic serine proteases (granzymes) into the synaptic cleft. Although the CTL and the target cell are both exposed to perforin within the synapse, only the target cell membrane is disrupted, while the CTL is invariably spared. How CTLs escape unscathed remains a mystery. Here, we report that CTLs achieve this via two protective properties of their plasma membrane within the synapse: high lipid order repels perforin and, in addition, exposed phosphatidylserine sequesters and inactivates perforin. The resulting resistance of CTLs to perforin explains their ability to kill target cells in rapid succession and to survive these encounters. Furthermore, these mechanisms imply an unsuspected role for plasma membrane organization in protecting cells from immune attack.

<sup>1</sup>Killer Cell Biology Laboratory, Peter MacCallum Cancer Centre, 305 Grattan Street, Melbourne, VIC 3000, Australia. <sup>2</sup>Sir Peter MacCallum Department of Oncology, University of Melbourne, Melbourne, VIC 3000, Australia. <sup>3</sup>London Centre for Nanotechnology, University College London, 19 Gordon Street, London WC1H 0AH, UK. <sup>4</sup>Institute of Structural and Molecular Biology, University College London, Gower Street, London WC1E 6BT, UK. <sup>5</sup>Biological Optical Microscopy Platform, The University of Melbourne, Parkville, VIC 3010, Australia. <sup>6</sup>Cancer Cell Death Laboratory, Peter MacCallum Cancer Centre, 305 Grattan Street, Melbourne, VIC 3000, Australia. <sup>7</sup>Department of Physics and Astronomy, University College London, Gower Street, London WC1E 6BT, UK. <sup>8</sup>Present address: Bristol-Myers Squibb, 4 Nexus Ct, Mulgrave, VIC 3170, Australia. <sup>9</sup>These authors contributed equally: Jesse A. Rudd-Schmidt, Adrian W. Hodel. <sup>10</sup>These authors jointly supervised the work: Bart W. Hoogenboom, Ilia Voskoboinik. \*email: [b.hoogenboom@ucl.ac.uk](mailto:b.hoogenboom@ucl.ac.uk); [ilia.voskoboinik@petermac.org](mailto:ilia.voskoboinik@petermac.org)

The immune system relies heavily on killer T cells (cytotoxic T lymphocytes, CTLs) to eliminate virus-infected or cancerous cells. A CTL binds to, and forms an immunological synapse with its target, then secretes a  $\text{Ca}^{2+}$ -dependent pore-forming protein (perforin) and a cocktail of pro-apoptotic serine proteases (granzymes) into the synaptic cleft<sup>1,2</sup>. Perforin-mediated membrane disruption is indispensable for allowing granzymes access to key substrates in the target cell cytosol, enabling the initiation of apoptosis of dangerous cells and to maintain immune homeostasis. Consequently, failure to release functional perforin results in fatal immune dysregulation or increased susceptibility to viruses and to haematological cancers<sup>1,3,4</sup>.

In a first and essential step, secreted perforin interacts with a target cell via  $\text{Ca}^{2+}$ -dependent membrane binding, mediated through its C2 domain. This is followed by oligomerization into short and non-inserted prepore assemblies and, ultimately, by insertion and further assembly of an entire mature pore across the plasma membrane<sup>5–7</sup>. Although the CTL and the target cell plasma membranes are both exposed to perforin within the synapse, paradoxically, only the target cell membrane is disrupted<sup>8</sup>. As a consequence, granzymes will penetrate and kill the target cell, whereas the CTL is almost invariably spared.

A number of mechanisms have been advanced to account for this apparently unidirectional action of perforin. Early reports indicated that perforin binds to specific lipid headgroups<sup>9</sup>, but subsequent work suggested tight lipid spacing to be a more relevant factor, making lymphocytes inherently resistant to perforin<sup>10</sup>. Yet CTLs can be killed by fratricide, provided that they can present cognate peptide on MHC<sup>1</sup>. Other explanations advanced to date include cleavage and inactivation of secreted perforin by the constitutive lysosomal cysteine protease cathepsin B (CatB)<sup>11</sup>, but this hypothesis was also refuted as CTLs from CatB-null mice survive multiple successive interactions with target cells with the resilience of CatB-competent counterparts<sup>12</sup>. In addition, some lymphocyte protection may potentially be acquired through externalization of an abundant cytotoxic

granule transmembrane protein, LAMP-1<sup>13</sup>. These various explanations should be considered in the context of recent single-cell analyses, which revealed that more than 95% of killer lymphocytes survive their encounter with a single target, ensuring their ability to disengage, then engage again to successively kill other dangerous cells<sup>8,14</sup>. This result highlights the extraordinary effectiveness of the mechanism(s) underpinning the target-cell specificity of, and/or lymphocyte protection against perforin in the immune synapse.

In this study, we use a variety of biochemical, biophysical and cell biological approaches to resolve the critical and long-standing question of the unidirectional action of perforin in the immunological synapse. We demonstrate that the CTL protects itself from perforin by dynamic control of its membrane lipid composition. Specifically, we identify two protective mechanisms: the CTL membrane repels perforin by arranging its lipids in a higher-ordered state (lipid rafts) at the immunological synapse, while also exposing phosphatidylserine (PS) within the synapse, thus creating a negatively charged sink that sequesters and inactivates any residual perforin. The resistance of CTLs to perforin underpins their capacity to kill multiple targets, and enables them to maintain immune homeostasis.

## Results

**CTLs are resistant to perforin binding and lysis.** We initially explored whether killer lymphocytes are intrinsically more resistant to perforin than their targets, and found that both primary activated CTLs (CD8<sup>+</sup> T cells from BL/6 OTI transgenic mice) and natural killer cells (isolated from BL/6 mice) required 10s- to 100s-fold more recombinant perforin to achieve the same level of lysis as common target cell lines (Fig. 1a). This suggests that perforin binds less efficiently to killer lymphocyte membranes and/or that its pore-forming function is impaired on these membranes.

To assess perforin binding levels without the confounding effect of cell lysis, we used a non-lytic mutant of perforin (TMH1-PRF) that binds as efficiently to target membranes as wild-type

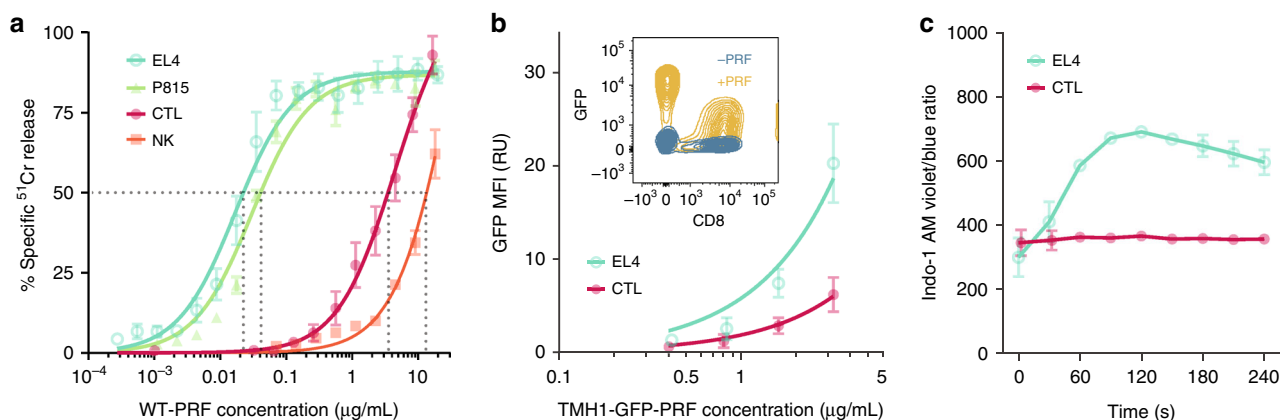


**Fig. 1** CTLs bind less perforin and resist pore formation. **a** <sup>51</sup>Cr release cytotoxicity assay on CTLs, natural killer (NK) cells, and EL4 and P815 target cells upon exposure to recombinant WT-PRF. CTLs are 2–3 orders of magnitude more resistant than target cells, as assessed at 50% <sup>51</sup>Cr release (dotted lines). Curves represent Michaelis–Menten fits to the data. **b** Binding of TMH1-GFP-PRF to a 1:1 mixture of CTL and EL4 cells, as assessed by flow cytometry, with GFP geometric mean fluorescence intensity (MFI) measured in relative units (RU). The cells were stained with anti-CD8-allophycocyanin (APC) prior to flow cytometry to differentiate the two cell types. The comparison was made for CTL and EL4 cells of the same size, as derived from forward and side scatter. Curves represent Michaelis–Menten fits to the data. Inset: example of flow cytometry data with TMH-GFP-PRF staining of a 1:1 mixture of CD8<sup>+</sup> (CTL) and CD8<sup>-</sup> (EL4) cells. **c**  $\text{Ca}^{2+}$  influx into Indo-1 AM labelled CTL and EL4 cells upon exposure to sub-lytic amounts of WT-GFP-PRF. Membrane perforation by perforin was measured via the  $\text{Ca}^{2+}$  influx over time, detected as an increase in the ratio of violet (400 nm) to blue (475 nm) fluorescence emission; WT-GFP-PRF was added at  $t = 0$ . See Supplementary Fig. 1b, c for control experiments that demonstrate similar levels of perforin binding to both cell types, as well as the specificity of the observed difference to perforin. Curves provide a visual guide connecting data points. Throughout the panels, each data point represents a mean  $\pm$  standard error of mean (s.e.m.) of three independent experiments. Source data for all panels are provided as a Source Data file.

perforin (WT-PRF), but incorporates an engineered disulphide bond that tethers the transmembrane domain and prevents its insertion into the target cell membrane<sup>6</sup>. Upon binding to the membrane, TMH1-PRF instead forms short prepore oligomers on the membrane, which represent a transient, intermediate state of WT-PRF pore assembly<sup>6</sup>. GFP-tagged variants (WT-GFP-PRF<sup>15</sup> and TMH1-GFP-PRF) enabled us to measure perforin binding to cells directly by fluorescence. As previously shown for TMH1-PRF<sup>6</sup>, the pore forming and lytic functions of TMH1-GFP-PRF were restored by reducing the engineered disulphide bond with dithiothreitol (DTT, Supplementary Fig. 1a). Using TMH1-GFP-PRF, we found that CTLs (CD8<sup>+</sup>) indeed bound less perforin than EL4 (CD8<sup>-</sup>) target cells of the same size (Fig. 1b, Supplementary Fig. 2a).

Although lower than the observed binding levels for target cells, perforin binding to CTLs is far from negligible (Fig. 1b), yet their plasma membranes almost invariably withstand disruption, as shown here and elsewhere<sup>8</sup>. Moreover, when the concentration of WT-GFP-PRF was adjusted so that CTLs and target cells bound similar amounts of perforin to their membranes, the CTL membranes still remained intact, while the target cell membranes were perforated, as indicated by Ca<sup>2+</sup> flux (Fig. 1c, Supplementary Figs. 1b, c, 2b). These results were confirmed further by demonstrating the survival of CTLs despite their binding significant amounts of WT-GFP-PRF (Fig. 2a, -EGTA, Supplementary Fig. 2a; note the significant GFP<sup>+</sup> population for CD8<sup>+</sup> cells at 37 °C).

We next (Fig. 2a, +EGTA) compared this CTL-bound perforin with the two known assembly states of perforin. In the early stages of pore formation, non-porating, prepore assembly intermediates are formed by WT-PRF at lower temperature and by TMH1-PRF in the absence of DTT<sup>6</sup>. These prepores can be removed from the membrane by depleting free Ca<sup>2+</sup> by the addition of EGTA. After binding, WT-PRF can form functional, transmembrane pore assemblies on target cells and model membranes at 37 °C. These perforin pores are EGTA resistant<sup>16</sup>. Intriguingly, although not lytic, the CTL-bound WT-GFP-PRF resembled functional, membrane-inserted perforin by being resistant to EGTA (Fig. 2a, +EGTA, Supplementary Fig. 2a). This is in contrast to the EGTA sensitivity shown by the non-lytic TMH1-GFP-PRF (Fig. 2b; for quantification of all conditions, see Fig. 2c). Taken together, these observations indicate that CTLs have an additional layer of protection, where membrane-bound perforin remains non-functional (i.e., non-porating) despite being apparently inserted into the membrane.

To explain both the reduced membrane binding and the reduced functionality of membrane-bound perforin on CTLs, we hypothesized that CTL plasma membranes may be more resistant to perforin binding and pore formation due to their lipid composition<sup>10</sup>. This hypothesis was also motivated by the observations that perforin does not require partner proteins for its membrane binding and pore formation; that it has no known inhibitors in the CTL membrane<sup>12</sup>; and that our experiments (Supplementary Figs. 2c, 3) did not confirm a previously postulated protective role of cytotoxic granule membrane protein CD107a (LAMP-1)<sup>13</sup>.

### High lipid order protects membranes from perforin binding.

To assess perforin binding and pore formation on membranes of defined lipid composition, we used atomic force microscopy (AFM) on supported lipid bilayers<sup>6,17–20</sup>. Ternary mixtures of cholesterol, sphingomyelin (SM) and (liquid-phase) phosphatidylcholine (PC) provided general biophysical model systems for the plasma membrane in which to assess the effect of lipid order<sup>21–23</sup>. By systematically varying membrane order across

single-phase and phase-separated regimes of this model membrane system (Supplementary Fig. 4), we found that perforin (specifically: WT-PRF) readily forms pores on PC-rich, liquid-disordered lipid phases, but avoids SM/cholesterol-rich liquid-ordered domains (Fig. 3a, b). Overall, higher SM and cholesterol content caused the membranes to be increasingly refractory to perforin pore formation (see dark areas in Fig. 3a), coinciding with regimes of enhanced lipid order<sup>21–23</sup>. Membrane binding of the non-porating TMH1-PRF mutant followed the same pattern (Supplementary Fig. 5), demonstrating that the observed reduction in WT-PRF pore formation on SM/cholesterol-rich membranes was due to a reduction in perforin binding. When more disorder-prone variants of SM (18:1 SM<sup>24</sup>) and of cholesterol (7-ketocholesterol, 7KC<sup>25</sup>) were used, perforin binding and pore formation were restored (Fig. 3c, d, Supplementary Fig. 6). Hence increased lipid order causes membranes to be refractory to perforin binding (and thus also to pore formation).

To test the effect of membrane order in live cells<sup>26</sup>, we reduced membrane order in CTLs by loading them with increasing quantities of 7KC<sup>25</sup>—thus substituting cholesterol in the membrane—prior to perforin exposure (Fig. 4a). Of note, a non-toxic concentration of 7KC (as used here) did not sensitize the cells to osmotic stress (Fig. 4b, c, Supplementary Fig. 2d). As predicted by our AFM findings, increased disorder in the CTL plasma membrane led to an increase of TMH1-GFP-PRF binding (Fig. 4d, Supplementary Fig. 2e) and accordingly to an increase in lysis by WT-PRF (Fig. 4e, Supplementary Fig. 2d), compared with cholesterol-treated cells. Remarkably, thus treated CTLs had their perforin sensitivity increased by up to tenfold, to levels comparable with untreated target cells (Fig. 4e). This increased sensitization to perforin was also observed for primary natural killer cells (Fig. 4f), but less so for target cells (Fig. 4e). We conclude that enhanced lipid order in the CTL plasma membrane reduces the efficiency of perforin binding. Consistent with this conclusion and the differences in perforin sensitivity between CTLs and their targets (Figs. 1, 2), we also note that CD8<sup>+</sup> T cells show over 30-fold higher staining for lipid raft marker GM1 than target cells (Supplementary Fig. 7).

**PS inactivates membrane-bound perforin.** Having determined a lipid-based mechanism that protects CTLs from perforin binding, we next set out to further explore our surprising observation of non-functional, yet membrane-bound and possibly inserted perforin on the CTLs (Figs. 1b, c, 2). To this end, we expanded the AFM analysis to phospholipids that are typically located in the inner leaflet of the plasma membrane<sup>27</sup>. Surprisingly, we found that perforin efficiently bound to membranes composed of PS, but did not form the well-defined, static arc- or ring-shaped assemblies that are characteristic<sup>5,6,19</sup> of transmembrane pores (Fig. 5a). Instead, WT-PRF and DTT-unlocked TMH1-PRF formed static protein clusters on PS, which sat up to ~5 nm higher above the membrane surface than locked (-DTT) TMH1-PRF prepores on both PC and PS. These static clusters were also higher (by the same amount) than functional perforin (WT-PRF and TMH1-PRF +DTT) on PC membranes. Fully consistent with our observations on CTL-bound perforin (Fig. 2a), the perforin clusters on PS membranes were resistant to Ca<sup>2+</sup> depletion by EGTA (Fig. 5b). In binary PC/PS mixtures, cluster formation was increased and functional pore formation reduced upon increasing PS content (Fig. 5c). We explored these unexpected observations further by assessing the behaviour of perforin on model membranes doped with other negatively charged lipids, specifically: DOPG (1,2-dioleoyl-*sn*-glycero-3-phospho-(1'-*rac*-glycerol)) or CS (cholesterol sulphate). Similar to PS, perforin pore assembly was impaired on both membranes (Supplementary Fig. 8). These



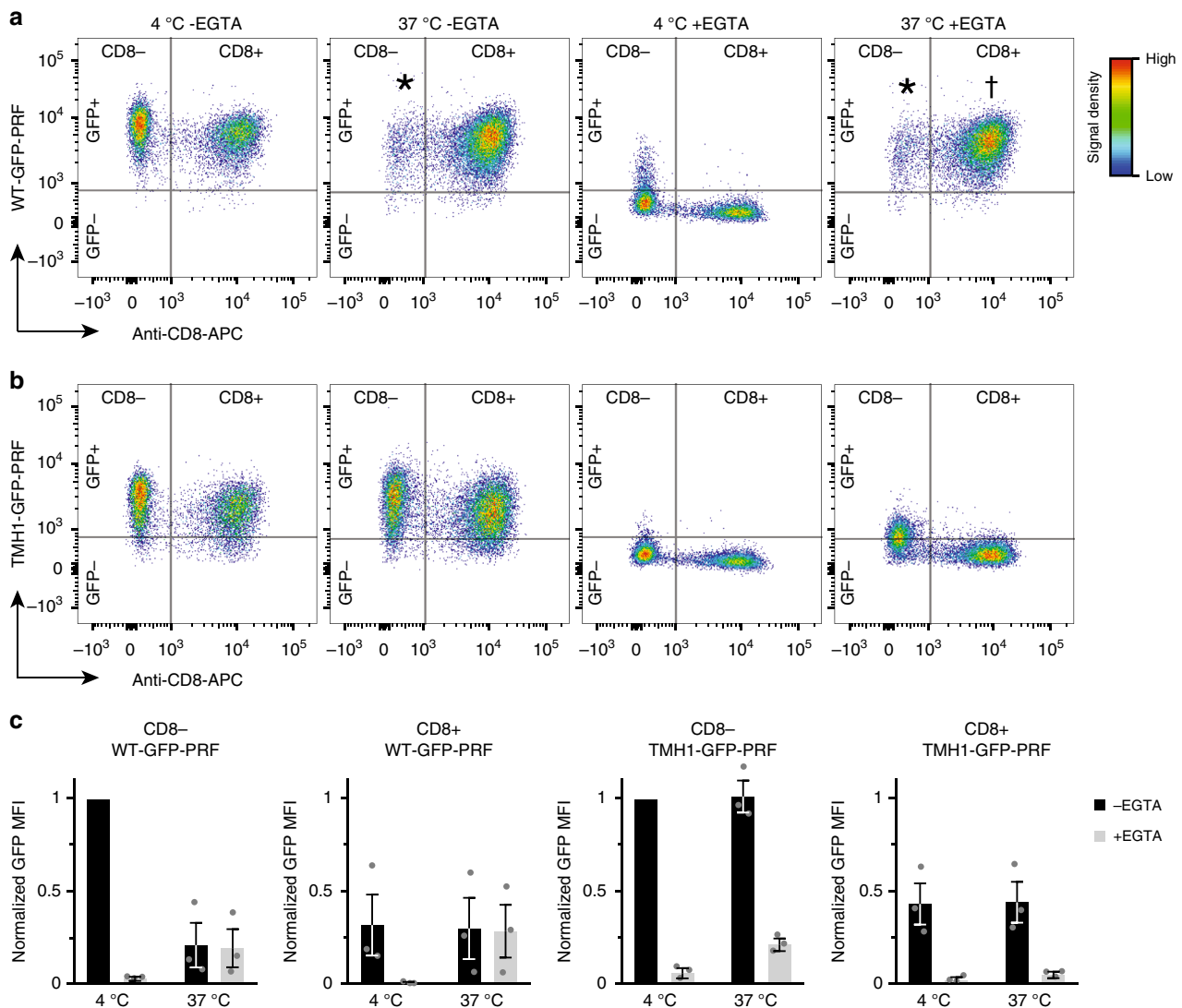


**Fig. 2** Residual perforin bound to CTLs is deactivated. **a** Binding of WT-GFP-PRF to EL4 (CD8<sup>-</sup>) and CTL (CD8<sup>+</sup>) cells, at concentrations that are sub-lytic to CTLs, as assessed by flow cytometry. At 4 °C and in the presence of Ca<sup>2+</sup> (–EGTA), both cell types bind perforin (GFP<sup>+</sup>), but the CTLs at a lower level than EL4 cells. At 37 °C and in the presence of Ca<sup>2+</sup> (–EGTA), WT-GFP-PRF is lytic to the EL4 cells, so no significant CD8<sup>-</sup> population remains under those conditions (asterisks). Upon subsequent Ca<sup>2+</sup> chelation by 2 mM EGTA, non-porating perforin assemblies (WT-GFP-PRF at 4 °C) are removed from the cell membranes (GFP<sup>-</sup>). However, Ca<sup>2+</sup> chelation does not affect WT-GFP-PRF bound to CTLs at 37 °C (GFP<sup>+</sup>, dagger), despite WT-GFP-PRF being apparently non-porating (see Fig. 1c). **b** Binding of non-lytic TMH1-GFP-PRF to EL4 (CD8<sup>-</sup>) and CTL (CD8<sup>+</sup>) cells, as assessed by flow cytometry. In the presence of Ca<sup>2+</sup> (–EGTA), TMH1-GFP-PRF binds to both cell types, but less to CTLs, as observed for WT-GFP-PRF. Upon subsequent Ca<sup>2+</sup> chelation by 2 mM EGTA (+EGTA), TMH1-GFP-PRF is invariably removed from the cell membranes, leaving only GFP<sup>-</sup> populations (both at 4 °C and 37 °C). **c** Quantification of flow cytometry results, with MFI of WT-GFP-PRF and TMH-GFP-PRF signals, normalized to the respective MFIs for the CD8<sup>-</sup> population at 4 °C. EGTA exposure drastically reduces the GFP MFI for all cases at 4 °C and for (non-lytic) TMH1-GFP-PRF at 37 °C. By contrast, WT-GFP-PRF is EGTA resistant once bound to CD8<sup>+</sup> cells at 37 °C. Note that the low GFP MPI at 37 °C in the first panel (CD8<sup>-</sup>, WT-GFP-PRF) is due to the majority of the CD8<sup>-</sup> cells being killed and thus not yielding a GFP signal in the flow cytometer anymore. The TMH1-GFP-PRF data (–EGTA) allow for a quantitative comparison between binding to CD8<sup>+</sup> and CD8<sup>-</sup> cells, showing that the CTLs (CD8<sup>+</sup>) bind less than half as much perforin as the target cells (CD8<sup>-</sup>). Each column represents a mean (±s.e.m.) of three independent flow cytometry experiments. Source data for **c** are provided as a Source Data file.

results show that the abnormal behaviour of perforin on PS membranes, i.e., the formation of non-porating assemblies, is due to the negative charge of the membrane surface.

On closer inspection by negative-stain electron microscopy on PS monolayers (Fig. 6a), the perforin clusters were found to consist of intermediates that appear similar to prepore (TMH1-PRF) assemblies in their size and subunit spacing (for quantification, see Fig. 6b, c), albeit more aggregated. Specifically, the subunit spacing of the clustered assemblies is  $3.8 \pm 0.8$  nm, compared with  $3.7 \pm 0.7$  nm for the locked TMH1-PRF as measured on PS here, and with  $3.86 \pm 0.13$  nm for locked

TMH1-PRF and with  $2.55 \pm 0.09$  nm for functional perforin pores (WT-PRF and TMH1-PRF +DTT) as previously determined on PC-rich membranes<sup>6</sup>. Taken together, these observations on PS are consistent with perforin assembly that is trapped in a dysfunctional (dead-end) state that prevents it from completing the prepore-to-pore transition.

If our hypotheses are correct, we would expect perforin to colocalize with exposed PS<sup>28</sup> on the CTL plasma membrane. To test this, we performed confocal microscopy on activated CTLs that were pre-treated with annexin V-Alexa Fluor 568, as a marker for PS exposed on the cell surface<sup>29</sup>. Importantly, this pre-



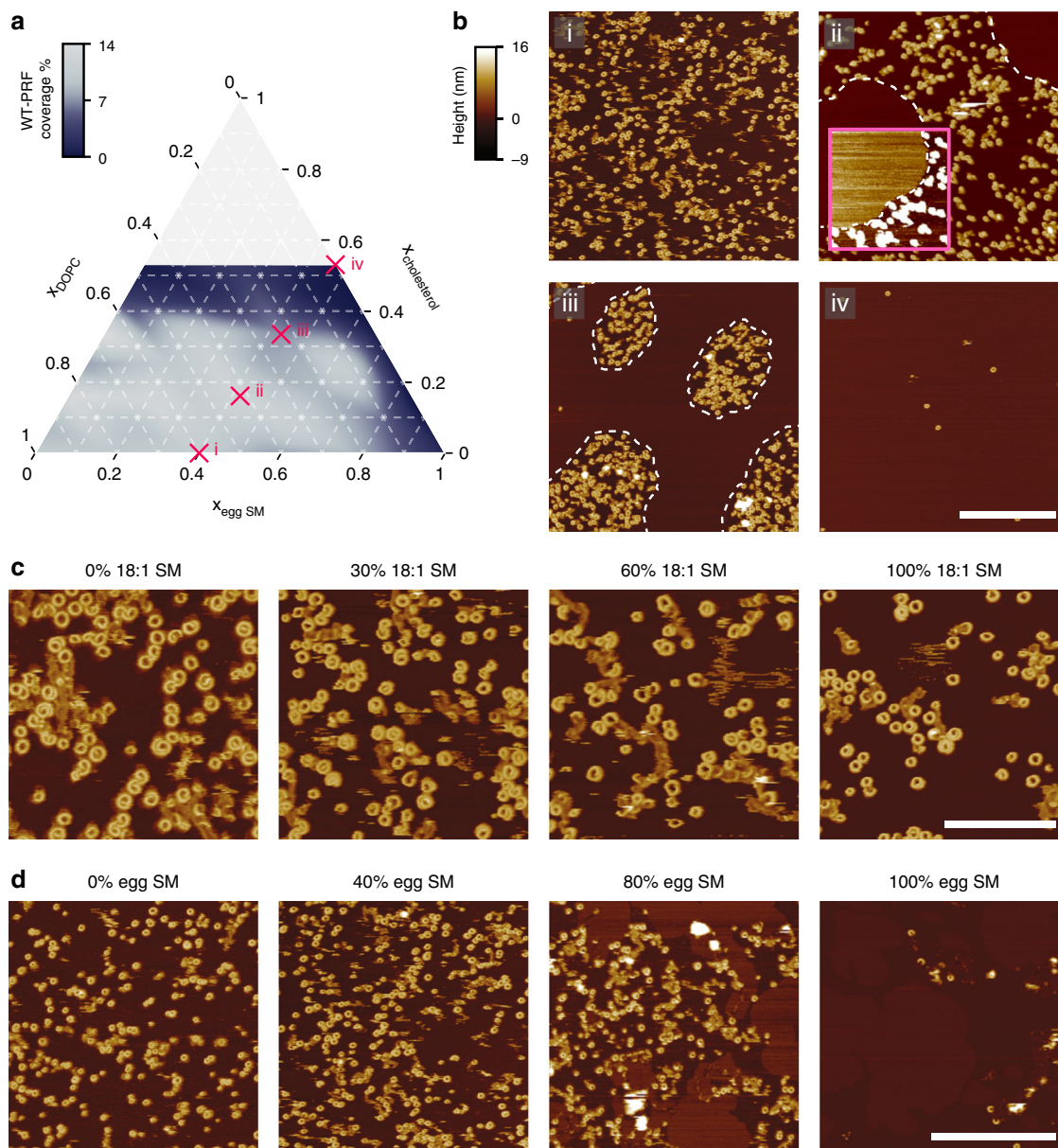


**Fig. 3** Lipid order protects membranes from perforin pore formation. **a** Perforin coverage (as % of membrane surface, as assessed by AFM imaging) after incubation of supported DOPC/egg SM/cholesterol bilayers with 150 nM WT-PRF, as a function of the molar fractions ( $x$ ) for the constituents of the bilayer (total = 1). See Supplementary Fig. 4 for explanation of the lipid phases observed in these membranes. Source data are provided as a Source Data file. **b** AFM images of perforin pores on supported lipid bilayers of the compositions i–iv labelled in **a**. AFM samples were incubated and imaged at 37 °C. For the area marked by a pink square in the top right image, the colour scale has been saturated (4 nm instead of 25 nm full range) to more clearly identify the enhanced thickness (height) of a liquid-ordered domain and the absence of perforin pores (white at this scale) on such domains. Throughout the images, lipid-phase boundaries are marked by dashed lines. Scale bar, 500 nm. **c** Representative AFM scans of supported DOPC bilayers, doped with different relative amounts of 18:1 SM (0–100%), and incubated with 150 nM WT-PRF. The doping with this disorder-prone SM variant does not appear to affect perforin pore formation, showing a similar coverage across all samples. This demonstrates that the observed perforin inhibition on egg SM membranes in **a** and **b** is not due to the SM headgroup (identical for egg SM and 18:1 SM), but due to the SM-induced changes in membrane order; unlike egg SM, pure 18:1 SM is in a liquid disordered state at 37 °C, just like DOPC<sup>24</sup>. Colour scale as in **b**. Scale bar, 200 nm. **d** As **c**, for comparison, except that the DOPC bilayer was doped with egg SM (0–100%). Phase separation is visible at 80%, and perforin coverage is notably diminished at 100% egg SM. These images were extracted from the dataset used to compose the plot shown in **a**. Note the different length scale. Colour scale as in **b**. Scale bar, 500 nm. All samples were incubated and imaged at 37 °C.

labelling with annexin V ensured detection only of PS already exposed on the CTL membrane before perforin addition, thus avoiding any contribution of PS flip/flop upon perforin association with the plasma membrane<sup>30</sup>. WT-GFP-PRF colocalized with punctate regions corresponding to (non-apoptotic) externalized PS (Fig. 7a, b). These punctate regions were also enriched for

the lipid-raft marker cholera toxin B (labelled GM1 in Fig. 7a, b), as was previously reported for both CTLs<sup>31</sup> and B cells<sup>32</sup>. To directly investigate the efficacy of this protective mechanism, WT-GFP-PRF was added to a 1:1 mixture of EL4 cells and CTLs in the presence of annexin V-Alexa Fluor 647 to identify exposed PS (Fig. 7c). EL4 cells bound perforin uniformly around their

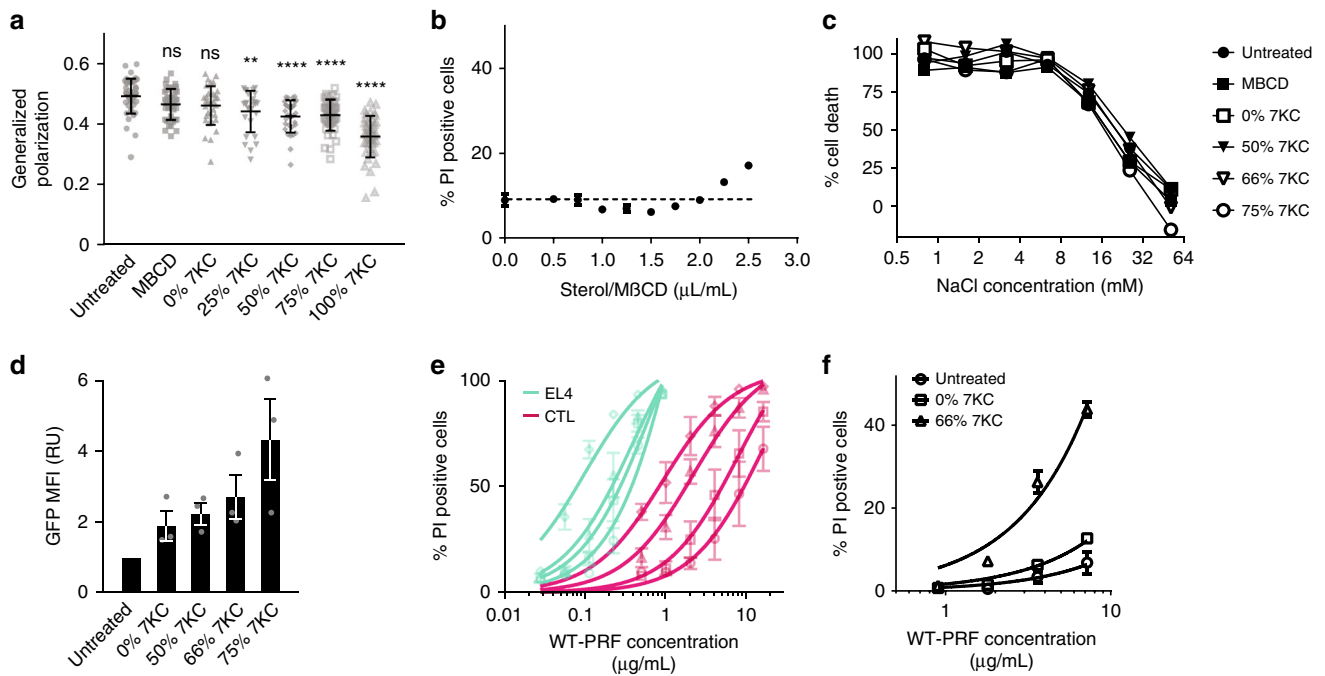


**Fig. 4** Reduced membrane order sensitizes cells to perforin lysis. **a** Lipid order in the CTL plasma membrane for cells treated with different ratios of 7KC/cholesterol, as measured by GP values<sup>26</sup> (see Methods). Data points represent individual cells, measured in three independent experiments and are overlaid with mean  $\pm$  s.e.m.; statistical significance was assessed using ANOVA with Dunnett's post-hoc analysis, where 'ns'—not significant,  $**p < 0.01$ ,  $****p < 0.001$ . **b** Determination of a non-cytotoxic concentration of 7KC. A total of  $5 \times 10^5$  CTLs were treated with increasing amounts of a 75% 7KC/25% cholesterol mix in M $\beta$ CD, and cell death assessed by propidium iodide (PI) staining. A total of 2.25  $\mu$ L/mL was chosen as the optimal concentration for following cholesterol loading experiments. Data points show mean  $\pm$  s.e.m. of three independent experiments with the dotted line marking background cell death (no sterol/M $\beta$ CD added). **c** 7KC treatment of CTLs does not sensitize cells to osmotic stress.  $^{51}$ Cr-loaded CTLs were treated with varying ratios of 7KC/cholesterol, incubated at different concentrations of NaCl, and cell death assessed by  $^{51}$ Cr release. Data points show mean of two independent experiments, with three technical replicates each. **d** Perforin binding to CTLs pre-loaded with different ratios of 7KC/cholesterol. The GFP MFI of cells that had been exposed to TMH1-GFP-PRF at 37  $^{\circ}$ C was measured by flow cytometry and normalized to the MFI of untreated cells. The data represent mean  $\pm$  s.e.m. of three independent experiments. **e** The reduced membrane order of 7KC-treated CTLs (red) and EL4s (blue) sensitizes the cells to WT-PRF lysis, as determined by PI staining of untreated cells (circles) and cells loaded with 50% (squares), 66% (triangles) and 75% (diamonds) 7KC. Data points show mean  $\pm$  s.e.m. of three independent experiments. Curves represent Michaelis-Menten fits. **f** Reduced membrane order of 7KC-treated murine NK cells sensitizes the cells to WT-PRF lysis. Data show mean PI staining of untreated cells (circles) and cells loaded with 0% (squares) and 66% (triangles) 7KC. Error bars represent s.e.m. ( $n = 3$  for all points except highest perforin concentration where  $n = 2$ ). Source data for all panels are provided as a Source Data file.

periphery and were lysed within minutes, whereas on CTLs, perforin signal was strongly associated with distinct regions where PS was exposed (Fig. 7b, c; Supplementary Video 1). Of note, nucleated cells employ an exocytic membrane repair response that is capable of protecting cells from an acute perforin lysis<sup>15</sup>, meaning EL4 cells do not immediately become annexin V positive, at least not for the perforin concentrations used here. However, over time, more EL4 cells die from perforin-induced damage, as highlighted in Supplementary Video 2.

Overall, inefficient perforin binding to CTLs (Fig. 1b), coupled with its inactivation by the plasma membrane PS, provides an explanation for their resistance to perforin lysis (Supplementary Video 2, Supplementary Fig. 9). Linking the results of AFM and cell-based experiments, it is important to note that the effective exposure of PS in the outer leaflet of our homogeneous supported bilayer can be lower than the overall PS concentration by more than a factor of 2, due to interaction of the charged PS headgroups (in the inner leaflet) with the mica substrate<sup>33</sup>. While this does not affect the overall trend observed for increased PS contents, it implies that the externalized PS in the cell membrane can be at levels well below 60% (observed in Fig. 5c) to achieve the same inhibitory effect on perforin pore assembly.

Taken together, we conclude that killer lymphocytes are protected in at least two ways against the perforin they secrete:

the lipid ordering in their membranes acts as a deflective shield against perforin binding and, in addition, perforin is scavenged and neutralized via the formation of non-lytic perforin clusters due to (negatively charged) PS that is externalized on the lymphocyte pre-synaptic membrane.

To consider this in the context of the immune synapse, we note that SM- and cholesterol-rich lipid domains (rafts) dynamically re-arrange and merge at the CTL membrane during immune synapse formation, as extensively demonstrated by others<sup>34–36</sup>. Hence, the presynaptic membrane will have a further increased lipid order compared with the overall CTL membranes tested here, thus enhancing its protection against perforin binding. In addition, PS was found to be exposed on T-cell membranes and directed to the presynaptic membrane<sup>31,37,38</sup> (Fig. 7d; Supplementary Video 3), allowing PS to act as a sink that binds and inactivates any perforin reaching the CTL membrane in the immune synapse (Fig. 8).

## Discussion

Unregulated binding and pore formation by perforin on the plasma membrane of CTLs and other cytotoxic lymphocytes would make immune killer cells as vulnerable to their own secreted potent cytotoxins as a target cell, and greatly reduce the efficiency of a cytotoxic response to dangerous pathogens. For



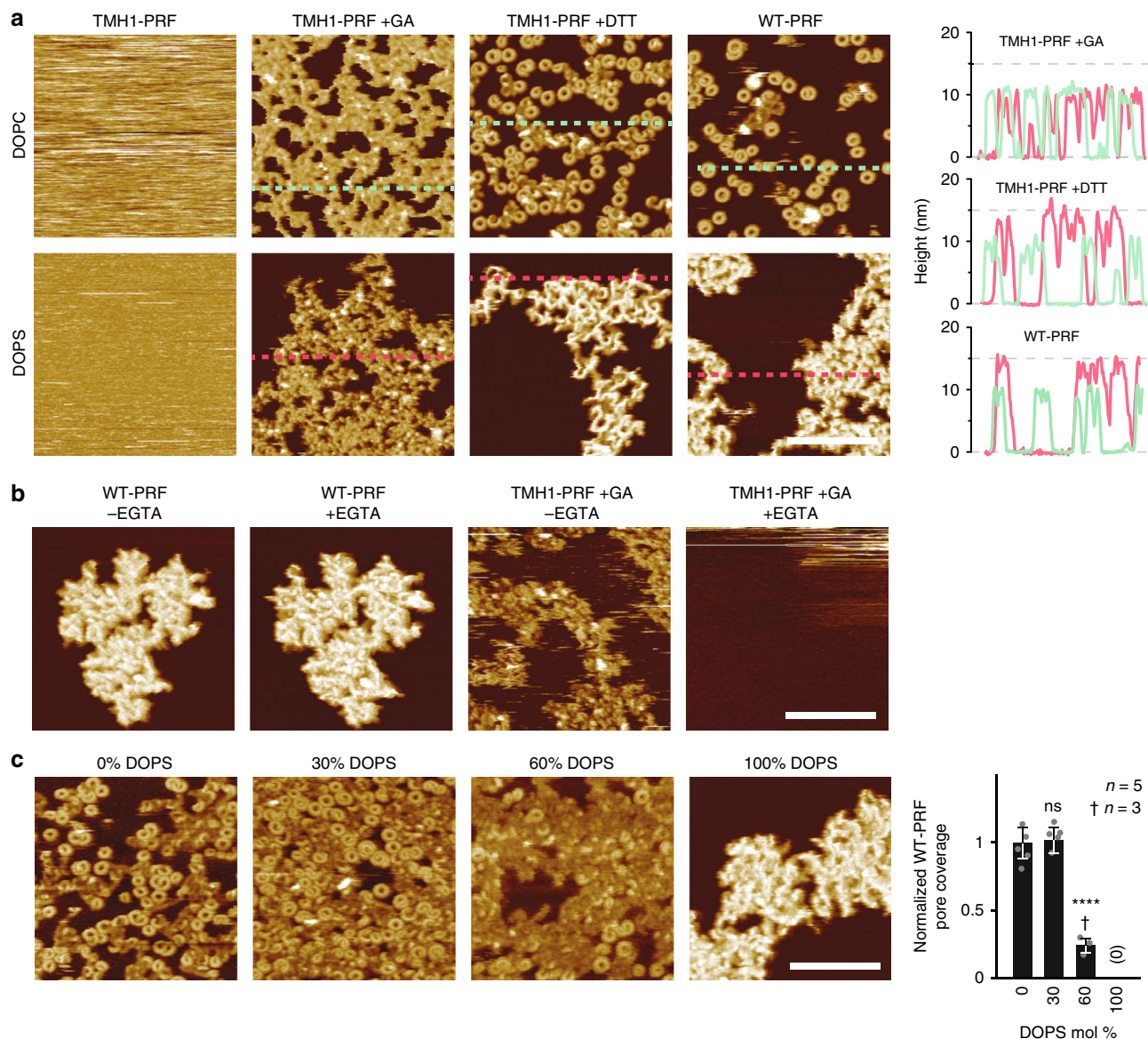


**Fig. 5** Perforin forms non-porating clusters on phosphatidylserine membranes. **a** AFM images of DOPC and DOPS supported lipid bilayers after incubation with TMH1-PRF without or with glutaraldehyde (+GA) fixation, with unlocked (+DTT) TMH1-PRF, or with WT-PRF. Height profiles were plotted as acquired along the dashed lines in the AFM image. On DOPC, prepare locked TMH1-PRF, and TMH1-PRF +DTT and WT-PRF assemblies all extend 10–11 nm above the membrane surface, in agreement with previous observations<sup>5,6,19</sup>. On DOPS, fixed (and locked) TMH1-PRF assemblies have the same height, but the clusters of unlocked TMH1-PRF (+DTT) and WT-PRF are distinctly taller, about 15 nm above the membrane. **b** AFM images of DOPS supported lipid bilayers incubated with WT-PRF or TMH1-PRF +GA, before and after Ca<sup>2+</sup> chelation by washing the membrane with 5 mM EGTA (±EGTA). Clusters formed by WT-PRF are not removed or visibly affected by washing the membrane with EGTA. In contrast, cross-linked plaques of TMH1-PRF +GA are removed after the EGTA wash. This is consistent with failure of TMH1-PRF to insert into the membrane<sup>6</sup> and suggests that WT-PRF partially inserts into the DOPS membrane. All samples were incubated at 37 °C and imaged at room temperature. Colour (height) scale for all panels as in Fig. 3b. **c** AFM images of supported DOPC bilayers mixed with 0–100% DOPS, after incubation with 150 nM WT-PRF. The images show decreased formation of arc- and ring-shaped perforin pores upon increased DOPS content, and an increased amount of clustering. Bar graph on the right shows quantification (see Methods; mean ± standard deviation) of pore formation on DOPS containing membranes: for 60% DOPS, there is a significant decrease in the number of pores, and at 100% DOPS there are no unambiguous pore features found. Statistical significance was assessed using ANOVA with Dunnett’s post-hoc analysis, where ‘ns’—not significant, \*\*\*\**p* < 0.001. Scale bars, 200 nm.

example, killer cells would have to be raised in at least equal numbers to virus-infected cells to ensure clearance of any infection<sup>39,40</sup>—this would be a particular challenge in major organs such as the liver, where many trillions of parenchymal cells are typically infected in a very short time-frame. In addition, if every CTL was to die following interaction with a target cell, this would preclude any antigen-experienced CTL from differentiating into a memory cell. Clearly, such a scenario would have

dire repercussions for the immune system’s ability to efficiently eliminate serious pathogens, while compromising antigen recall responses and immune homeostasis. It is therefore not surprising that mammals have evolved mechanisms to ensure that perforin’s deleterious effects on the killer cell are carefully controlled, just as there are multiple mechanisms in place to prevent the premature activation of perforin during its biosynthesis, processing, storage and release<sup>41–43</sup>.

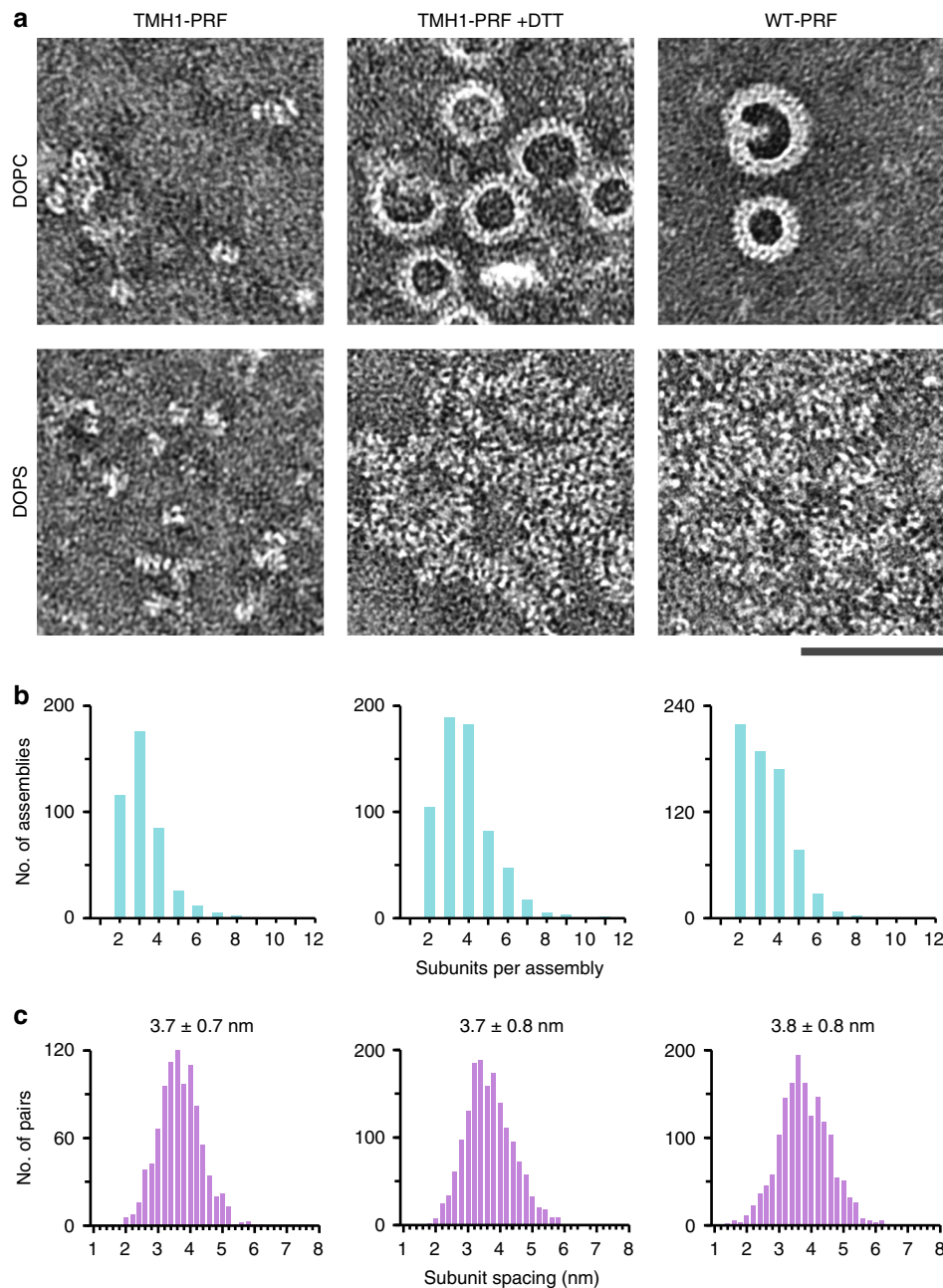


**Fig. 6** On DOPS, perforin assemblies retain properties found in prepores. **a** EM images of DOPC and DOPS monolayers after incubation with TMH1-PRF (-DTT), unlocked TMH1-PRF +DTT, or with WT-PRF, at subunit resolution. On DOPC, TMH1-PRF prepores are visible as short, loose assemblies, which grow into arc- and ring-shaped pores after unlocking (TMH1-PRF +DTT) or when using WT-PRF, accompanied by a tighter subunit packing, and fully consistent with previous observations<sup>6</sup>. On DOPS, initially short assemblies formed by TMH1-PRF appear similar to prepores formed on DOPC. After unlocking with DTT or when incubating with WT-PRF, the clusters retain signatures of short assemblies, and lack the tight packing observed for perforin pores. Scale bar, 50 nm. **b** Length distributions of assemblies as found in isolated assemblies and clusters on DOPS that show subunit repetitions (see Methods). **c** Average subunit spacing ( $\pm$  standard deviation) on DOPS; these results are comparable with previously published data on perforin prepore (TMH1-PRF) assemblies formed on PC-rich membranes, with sizes ranging between 2 and 10 subunits and a subunit spacing of  $3.86 \pm 0.13$  nm; on such PC rich membranes, pore assemblies are significantly larger and have a tighter subunit spacing,  $2.55 \pm 0.09$  nm<sup>6</sup>. Source data for **b** and **c** are provided as a Source Data file.

Here, we have demonstrated that some physiologically relevant types of lipid membrane composition are far less susceptible to perforin binding and/or poration than others; and that CTLs use these more resistant lipid formulations in a two-layered self-defence mechanism to maximize protection. In particular, the lymphocytes become refractory to secreted killer proteins due to increased plasma membrane lipid order, thus reducing perforin binding, and the exposure of negative charge

on the membrane surface via PS, thus inactivating residual perforin within the immune synapse. These self-protection mechanisms provide each CTL with the ability to kill many successive targets, which is essential for timely viral or cancer cell clearance and for host immune homeostasis. This represents a hitherto unsuspected role for lymphocyte lipid organization, going beyond previously demonstrated effects on immune signalling<sup>44</sup>. Finally, our findings suggest a lipid-based



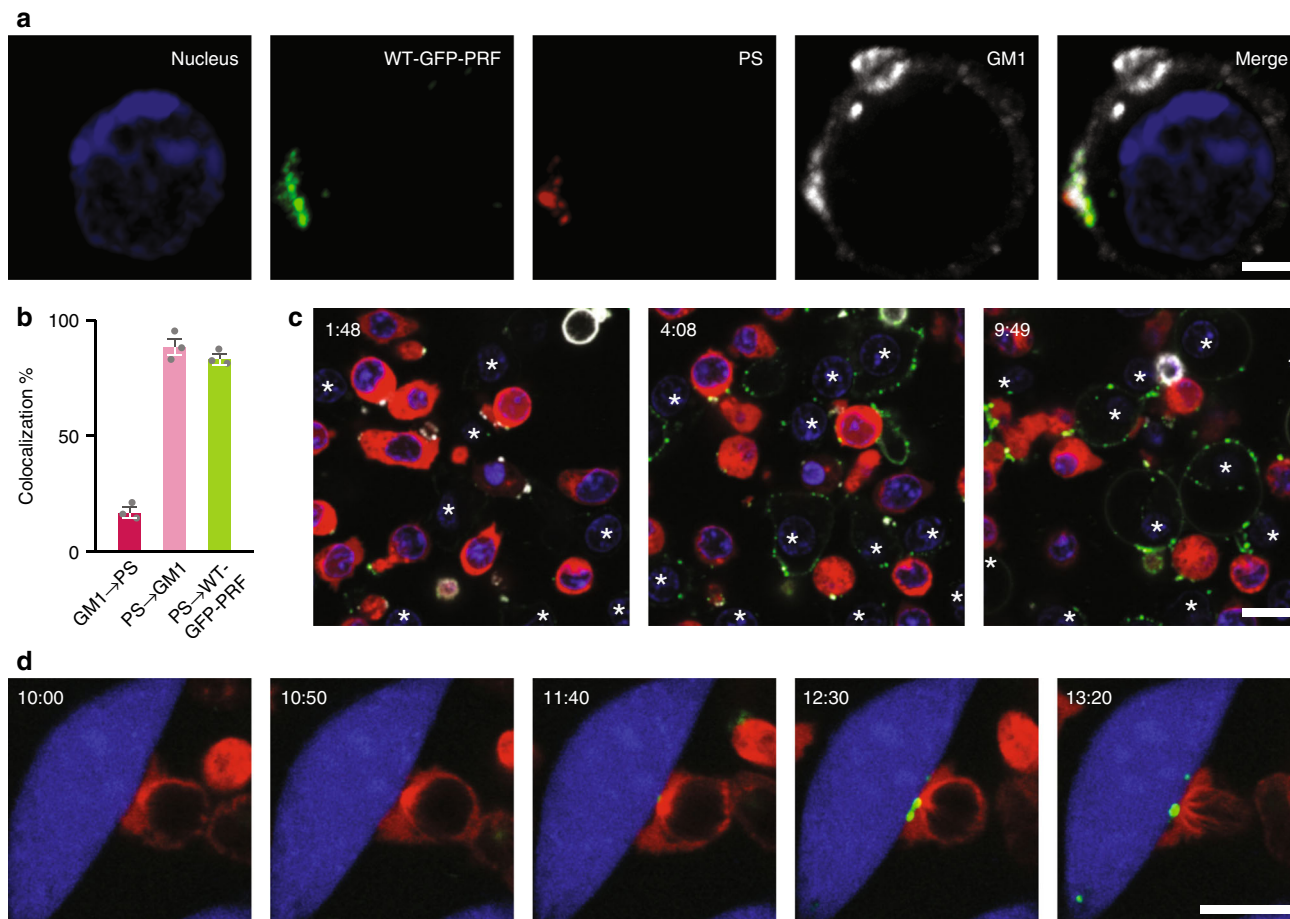


**Fig. 7** Perforin binding to phosphatidylserine on the CTL plasma membrane. **a** Colocalization of GM1 (detected by cholera toxin subunit B-Alexa Fluor 647), externalized PS (detected by annexin V-Alexa 568) and recombinant WT-GFP-PRF (signal enhanced by GFP-TAG polyclonal antibody-Alexa 488) on a CTL. The nucleus (blue) is detected by Hoechst 34580. **b** Quantitative analysis (see Methods) of **a** shows low colocalization levels of GM1 with PS (17%) but high colocalization of PS with GM1 (88%) and PS with WT-GFP-PRF (83%). This indicates that the vast majority of PS is contained within lipid raft areas (whereas there are many lipid raft areas which do not contain PS) and more than 80% of this PS binds WT-GFP-PRF. Sixty-two cells were analysed, and the mean  $\pm$  s.e.m. of three independent experiments is shown for each condition. Source data are provided as a Source Data file. **c** Montage of time-lapse confocal microscopy (Supplementary Video 1). WT-GFP-PRF (green) was added at 1:17 min to a mixture of CTLs transduced with cherry-tubulin (red) and EL4 cells (white asterisks). Hoechst 33342 staining (blue) shows the nucleus of both cell types. Annexin V-Alexa 647 (white) was maintained in the culture medium throughout the assay; it binds to PS exposed on the CTLs and to PS on and within EL4 cells that are exposed to cytotoxic levels of perforin and that lose membrane integrity. EL4 cells are seen to bind WT-GFP-PRF uniformly before gradually becoming annexin V positive, whilst perforin on the CTL membrane localizes precisely (and almost immediately) to regions of exposed PS, without lysing the CTLs (Supplementary Video 2). **d** Montage of time-lapse confocal microscopy (Supplementary Video 3) reveals a bright punctate region of PS (detected by annexin V-Alexa 488 maintained during assay; shown in green) exposed on the CTL membrane during synapse formation. Cell Trace Violet labelled target cells (MC57, shown in blue) were labelled with SIINFEKL and synapse formation is confirmed by the docking of the centrosome (detected by cherry-tubulin expressed in the *Prfl*<sup>-/-</sup> CTL; shown in red) at the point of contact between CTL and target. Timestamps in **c** and **d** are in minutes. Scale bars: **a**, 2  $\mu$ m; **c**, **d**, 10  $\mu$ m.

mechanism through which transformed cells might achieve resistance to CTL attack, e.g. in the context of cancer immunotherapies.

## Methods

**Lipid vesicle and AFM sample preparation.** 1,2-dioleoyl-*sn*-glycero-3-phosphocholine (DOPC), 1,2-dioleoyl-*sn*-glycero-3-phospho-L-serine (DOPS), DOPG, egg SM, *N*-oleoyl-D-erythro-sphingosylphosphorylcholine (18:1 SM), cholesterol, cholesterol 3-sulphate (CS), and 7KC were purchased from Avanti Polar Lipids (Alabaster, AL, USA) as powder or dissolved in chloroform or in case of CS in a chloroform/methanol/water mixture (20:9:1 volume ratio). The lipids were mixed in the desired molar ratio, and small unilamellar vesicles were prepared using the lipid extrusion method<sup>6,45</sup>. Indicated lipid ratios and percentages refer to molar values and are given with  $\pm 5\%$  confidence intervals.

A total of 4  $\mu$ L of the small unilamellar vesicles were injected onto a freshly cleaved mica surface (Agar Scientific, Essex, UK) in the presence of 80  $\mu$ L of 20 mM HEPES, 150 mM NaCl, 25 mM Mg<sup>2+</sup>, 5 mM Ca<sup>2+</sup>, pH 7.4, adsorption buffer. To form pure DOPG bilayers, an adsorption buffer containing 10 mM Ca<sup>2+</sup> and no Mg<sup>2+</sup> was used. A 30 min incubation above the main transition temperature of the

lipids allowed the vesicles to rupture and adsorb onto the mica surface, yielding an extended lipid bilayer film. Excess vesicles were removed by washing the samples at least nine times with 80  $\mu$ L of the adsorption buffer. Supported lipid bilayers containing DOPS (Figs. 5, 6), DOPG, or CS (Supplementary Fig. 8) were washed with 20 mM HEPES, 150 mM NaCl, 5 mM Ca<sup>2+</sup>, pH 7.4, instead of the adsorption buffer to remove Mg<sup>2+</sup> or excess Ca<sup>2+</sup> ions, as they would interfere with perforin binding to the (negatively charged) membranes.

Perforin was diluted up to ca. tenfold in 20 mM HEPES, 150 mM NaCl and injected onto supported lipid bilayers in the adsorption buffer, leading to a final protein concentration of about 150 nM, and incubated for 5 min at 37 °C. The AFM samples used in Fig. 3 were incubated for a reduced duration (2 min instead of 5 min) and subsequently washed six times with the adsorption buffer to counteract excessive aggregation on some of the lipid mixtures under study.

For unlocking TMH1 perforin and TMH1-GFP perforin after their binding to the membrane (Figs. 5, 6; Supplementary Fig. 5), the mutant proteins were incubated with 2 mM DTT (Sigma-Aldrich) for 10 min at 37 °C.

Mobile, membrane-bound TMH1-PRF in Fig. 5 was fixed by addition of 0.04% glutaraldehyde (TAAB Laboratories, Reading, UK), labelled +GA in the figures) and 10 min incubation at room temperature. The samples were next washed with 20 mM HEPES, 150 mM NaCl, 5 mM Ca<sup>2+</sup>, pH 7.4, prior to AFM imaging.

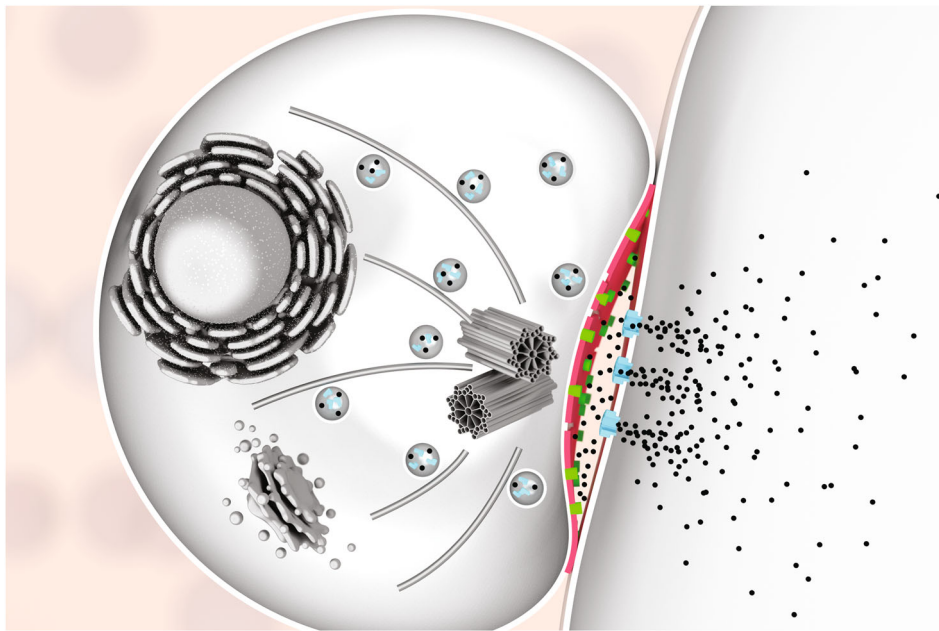


**Fig. 8** Mechanism of cytotoxic lymphocyte protection from secreted perforin. Illustration of a cytotoxic lymphocyte forming an immune synapse (shown are the microtubule-organizing centre and cytototoxic granule polarization), with granzymes (black dots) entering the target cells through perforin pores (light blue) in the target cell plasma membrane. High lipid order domains (red) and exposed phosphatidylserine (green) at the immunological synapse protect the lymphocyte against the perforin it secretes.

**AFM imaging and data processing.** AFM images were recorded by force-distance curve-based imaging (PeakForce Tapping) on a MultiMode 8 system (Bruker, Santa Barbara, CA, USA). PeakForce Tapping was performed at 2 kHz and a maximum tip-sample separation between 5 and 20 nm. Images were typically recorded at ca. 6 min/frame on an E scanner (Bruker, Santa Barbara, CA, USA) with temperature control. MSNL-E and -F probes (Bruker, Santa Barbara, CA, USA) were used at forces between 50 and 100 pN.

Raw AFM data were processed in NanoScope Analysis software version 1.80 (Bruker, Santa Barbara, CA, USA). AFM images were flattened with respect to the lipid surface, using a height threshold and second-order flattening. Height values indicated in the manuscript are given with  $\pm 1$  nm confidence intervals, with the uncertainty related to both scanner calibration and the possible sample deformation in the AFM images. Values for perforin coverage (Fig. 3) were estimated by considering the number of pixels above a height threshold, located 6–8 nm above the membrane surface and adjusted to counteract broadening effects of differently shaped AFM tips. The values for perforin coverage obtained by this method are either given as area percentage, or as values between 0 and 1 when normalized with respect to a 100% DOPC reference. In the case of Fig. 5c and Supplementary Fig. 8, for which we recorded data at a higher pixel resolution, the perforin coverage was determined by tracing pore shapes with 3dmod 4.9.4 (BL3DEMC & Regents of the University of Colorado,<sup>46</sup>). The traces were normalized with respect to a reference coverage as measured on pure DOPC membranes, resulting in values of coverage between 0 and 1.

**Electron microscopy.** Negatively stained samples of perforin on pure DOPC and DOPS monolayers were prepared in polytetrafluoroethylene (PTFE) troughs<sup>6,47</sup> containing 35  $\mu$ L of buffer (20 mM HEPES, 150 mM NaCl, 5 mM  $\text{Ca}^{2+}$ , pH 7.4) containing ca. 1.2 nM WT- or TMH1-PRF. In brief, 0.3  $\mu$ L of 1 mg/mL lipid in chloroform was placed at the air/buffer interface to form a lipid monolayer. After 1 min, a 200-mesh carbon-film-coated gold grid (Agar Scientific, Essex, UK) was placed on the lipid monolayer and incubated for 15 min at 37 °C (for TMH1-PRF, 2 mM DTT was added after 5 min). The samples were subsequently washed and stained with 2% w/w uranyl acetate.

Electron micrographs were recorded on a 4kx4k Ultrascan 4000 CCD camera (Gatan, Pleasanton, CA, USA), using a Tecnai T12 microscope (FEI Company, Hillsboro, OR, USA) operating at an accelerating voltage of 120 kV, a magnification of 67k (1.64 Å pixel size), and an underfocus of 0.5–1  $\mu$ m. Final adjustments on the raw images were done in Fiji/ImageJ 1.50e<sup>48</sup>. Raw images were processed with a Gaussian bandpass filter with a range of 4–300 pixels and binned by a factor of two to reduce noise, yielding a 2048  $\times$  2048 pixel image. The contrast was adjusted with the Auto setting in the Fiji/ImageJ software.

In EM data with well-resolved assemblies and assembly subunits in perforin clusters on DOPS (Fig. 6), histograms of assembly sizes and subunit distances were obtained from a custom interface written in Matlab R2016A (Mathworks, Cambridge, UK). Within the interface, perforin subunits were located and marked

by hand within each assembly. In the EM images recorded on DOPS, perforin assemblies appeared sufficiently separated to distinguish them from one another, and their subunits were sufficiently clear to allow such manual tracing.

**Cell culture.** Murine cell lines EL4 (ATCC TIB-39), P815 (ATCC TIB-64) and MC57 (ATCC CRL-2295) were maintained in SAFC DMEM (Sigma-Aldrich, Missouri, USA) media supplemented with 10% FCS (Gibco, Loughborough, UK), 15 mM HEPES (Merck, Missouri, USA), 44 mM  $\text{NaHCO}_3$  (Merck, Missouri, USA) and 2 mM Glutamax (Gibco, Loughborough, UK) at 37 °C in 10%  $\text{CO}_2$ . Primary murine  $\text{CD8}^+$  T cells (CTLs) and purified natural killer cells were generated from BL/6 OTI transgenic mice or BL/6 mice, respectively, and maintained as described previously<sup>49</sup> (approved by the Peter MacCallum Cancer Centre Animal Ethics Committee).

Wild-type perforin (WT-PRF), perforin-GFP fusion protein (WT-GFP-PRF), TMH1 perforin mutant (TMH1-PRF) and its GFP fusion protein (TMH1-GFP-PRF) were expressed and purified using baculovirus expression system<sup>6,15</sup>.

**Sorting/surface staining analysis of transduced cells.** To obtain a truncated form of CD107a (LAMP-1) that is retained on the cell membrane<sup>13</sup>, the sequence was cloned into the MSCV-IRES-GFP retroviral vector and transduced into EL4 and *Pf1*<sup>-/-</sup> OTI T cells<sup>6</sup>. After sorting for equal protein expression levels of the truncated CD107a construct and of an empty vector control (via GFP fluorescence), cells were stained (on the day of the <sup>51</sup>Cr release assay) with anti-CD107a-phycoerythrin (PE) antibody (eBioscience, California, USA) to assess surface levels of CD107a (Supplementary Fig. 3a). Cherry-tubulin fusion<sup>50</sup> was cloned into a MSCV vector, naive CTLs transduced and Cherry-positive cells were sorted 3 days later and used in experiments shown in Fig. 7c, d, Supplementary Fig. 9 and Supplementary Videos 1–3.

**Cytotoxicity assay.** For <sup>51</sup>Cr release assays<sup>51</sup> (Fig. 1a, Supplementary Figs. 1a, 2b, c),  $2 \times 10^6$  target cells were incubated with 200  $\mu$ Ci of <sup>51</sup>Cr (sodium chromate) in 200  $\mu$ L of complete DMEM media for 1 h at 37 °C. Where required for antigen-dependent CTL killing assay (Supplementary Fig. 3c), 1  $\mu$ M SIINFEKL peptide (GenScript, New Jersey, USA) was included in this incubation step. After 1 h, the cells were washed three times with complete DMEM and either incubated with OTI T cells at the desired effector/target ratio for 4 h, or mixed with various amounts of recombinant perforin and incubated for 1 h; these assays were conducted in 96-well plates in either 200  $\mu$ L (OTI T cell assays) or 100  $\mu$ L reactions (recombinant perforin assays). The plates were then centrifuged, supernatant collected, and its radioactivity assessed using a 1470 Wizard Automatic Gamma Counter (Wallac, Turku, Finland). Percentage specific <sup>51</sup>Cr release was calculated as  $[(^{51}\text{Cr}_{\text{assay}} - ^{51}\text{Cr}_{\text{spontaneous}})/(^{51}\text{Cr}_{\text{total}} - ^{51}\text{Cr}_{\text{spontaneous}}) \times 100]$ ; <sup>51</sup>Cr<sub>total</sub> was the level of radioactivity in target cells lysed with 1% Triton X-100, and <sup>51</sup>Cr<sub>spontaneous</sub> was the level

of radioactivity released by target cells incubated in the media in the absence of CTL or recombinant perforin for 4 h or 1 h, respectively.

**Perforin binding assays accessed via flow cytometry.** For the flow cytometry assays of perforin binding (Figs. 1b, 2, 4d), cells were washed three times in DMEM containing 0.1% BSA (Roche Diagnostics, Mannheim, Germany) and resuspended at  $10^6$  cells/mL. EL-4 (not pulsed with the SIINFEKL antigen) and CTLs were then mixed 1:1 to remain at a final concentration of  $10^6$  cells/mL. WT-GFP-PRF or TMH1-GFP-PRF was added to the mixture, and cells were incubated at 4 °C or 37 °C for 30 min. Unbound perforin was removed by washing the cells in 0.1% BSA DMEM, cells were stained with anti-CD8 APC (eBioscience, California, USA) and analysed using a Fortessa X20 flow cytometer (BD Biosciences, New Jersey, USA). To demonstrate  $Ca^{2+}$ -specific perforin binding, cells were treated with 2 mM EGTA prior to staining with anti-CD8 APC.

**Surface staining for GM1 analysis.** Cells were washed three times in complete DMEM and resuspended at  $10^6$  cells/mL. EL-4 (not pulsed with the SIINFEKL antigen) and CTLs were then mixed 1:1 to remain at a final concentration of  $10^6$  cells/mL. Cells were stained with anti-CD8 PE antibody (eBioscience, California, USA) and CTxB-Alexa Fluor 647 (Molecular Probes, Oregon, USA) and analysed using a Fortessa X20 flow cytometer (BD Biosciences, New Jersey, USA) (Supplementary Fig. 7).

**Unlocking of TMH1-GFP-PRF on cells.** TMH1-GFP-PRF was added to  $^{51}Cr$ -labelled EL4 cells resuspended in DMEM supplemented with 0.1% BSA at 37 °C. After 30 min, cells were washed with serum-free media, and 0.75 mM DTT was added to unlock the protein. After 5 min, DTT was quenched by addition of 0.1% BSA, and cells were incubated for a further 2 h at 37 °C (Supplementary Fig. 1a).

**Calcium flux assay.** CTLs and EL4 cells were labelled separately with a ratiometric (400 nm/475 nm) calcium fluorophore Indo-1AM (Invitrogen, California, USA)<sup>8,15</sup> and treated with varying amounts of WT-GFP-PRF to determine amounts for which both cell types stained with a similar level of GFP (Supplementary Fig. 1b). Time-course flow cytometry was performed<sup>15</sup> following WT-GFP-PRF addition (Fig. 1c). Cells treated with 1 µg/mL ionomycin (Sigma-Aldrich, Missouri, USA) were used as controls (Supplementary Fig. 1c).

**Modification of cellular cholesterol using 7KC.** Cholesterol or 7KC (both Sigma Aldrich, Missouri, USA) were dissolved in 100% ethanol at 15 mg/mL and mixed at different ratios. Cholesterol/7KC mixtures (as well as 100% cholesterol designated as 0% 7KC in Fig. 4, or 100% 7KC) were added drop-wise over a period of 30 min, to a solution of 50 mg/mL methyl-β-cyclodextran (MβCD, Sigma Aldrich, Missouri, USA) in PBS, which was heated to 80 °C, to achieve the final stock concentration of 1.5 mg/mL. Cells were washed three times in 0.1% BSA RPMI-1640 (Gibco, Paisley, UK) before being resuspended at  $0.5 \times 10^6$ /mL. Up to 2.25 µL of cholesterol/7KC stock solutions in MβCD were then added to 1 mL of cells; the cells were incubated at 37 °C for 30 min, then washed three times in 0.1% BSA DMEM, resuspended at  $10^6$ /mL and immediately used for either perforin binding or lysis experiments, or laurdan microscopy (Fig. 4).

**Assessment of membrane order via laurdan microscopy.** Cells were incubated in 0.1% BSA DMEM supplemented with 5 µM laurdan (Molecular Probes, Oregon, USA) in DMSO for 1 h. Cells were then pelleted and resuspended in 250 µL serum-free DMEM before being plated out in 8-well Nunc Lab-Tek II #1.5H glass-bottom chamber wells (Thermo Fisher Scientific, Massachusetts, USA). After allowing the cells to adhere for 20 min at 37 °C, 50 µL of 0.5% BSA solution was added to maintain cell viability during imaging. Lambda stacks were recorded using a Zeiss Elyra PS.1 microscope with a Tokai Hit stage/objective heater attached, and 5% CO<sub>2</sub>/humidity maintained (Zeiss, Oberkochen, Germany). An optical zoom of 2 was applied to a Plan-Apochromat 63×/1.4 Oil DIC lens (Zeiss, Oberkochen, Germany) and images were obtained every 8.9 nm from 410 nm to 695 nm using a line average of 16. Recorded stacks were exported to the Spectral Imaging Toolbox in Matlab<sup>52</sup>, where the data were segmented to isolate the laurdan signal from the plasma membranes of individual cells and the generalized polarization (GP) of the plasma membrane calculated (Fig. 4a). Images of a reference solution (laurdan in DMSO) were obtained with the same microscope settings as used for the imaging of cells, and a reference value (GP<sub>ref</sub>) of 0.207 was used for laurdan<sup>26</sup>. For details of GP calculation using the Spectral Imaging Toolbox, see ref. <sup>52</sup>.

**Live cell imaging of annexin V-labelled cells.** For Fig. 7c, Supplementary Fig. 9 and Supplementary Videos 1 and 2, a 1:1 mixture of EL4 and Cherry-tubulin expressing OTI T cells was washed three times in 0.1% BSA DMEM, labelled with 5 µM Hoechst 33342 (Life Technologies, California, USA), washed three times and then resuspended in a 1:50 stock dilution of annexin V-Alexa 647 in 0.1% BSA DMEM. These cells were then plated into 8-well Nunc Lab-Tek II #1.5H glass-bottom chamber wells (Thermo Fisher Scientific, Massachusetts, USA). WT-GFP-PRF was added during imaging. Cells were imaged using a Zeiss Elyra PS.1 microscope with a Tokai Hit stage/objective heater attached, and 5% CO<sub>2</sub>/humidity

maintained (Zeiss, Oberkochen, Germany). Imaging was performed using a Plan-Apochromat 63×/1.4 Oil DIC lens (Zeiss, Oberkochen, Germany) using an optical zoom of 1 and a line average of 4.

For live-cell imaging of PS exposure at the immunological synapse (as detected by annexin V labelling) (Fig. 7d, Supplementary Video 3), MC57 target cells were trypsinized and washed. A total of  $10^6$  cells were then resuspended in 500 µL of 5 µM Cell Trace Violet solution (Invitrogen, California, United States) in PBS for 20 min at 37 °C; 10 mL of complete medium was then added to these cells to quench any unbound dye. Cells were pelleted, resuspended in complete DMEM media, counted and plated at 30,000 cells ( $10^6$  cells/mL) per well of an 8-well ibidi-treat imaging chamber (Ibidi, Martinsried, Germany), 1 day before imaging. Approximately 4 h before imaging, cells were labelled with 1 µM SIINFEKL (GenScript, New Jersey, USA) at 37 °C for 1 h, before being washed three times in complete DMEM, and allowed to rest. Cherry tubulin transduced OTI T cells from *Prfl<sup>-/-</sup>* mice were then resuspended in 300 µL of a 1:50 stock dilution of annexin V-Alexa Fluor 488 (Invitrogen, California, USA) in complete DMEM before being added to the microscopy chamber. All medium was removed from the MC57 cells, such that both the MC57 and OTI T cells were imaged in the presence of a 1:50 stock dilution of annexin V-Alexa Fluor 488. Cells were imaged using a Zeiss Elyra PS.1 microscope with a Tokai Hit stage/objective heater attached, and 5% CO<sub>2</sub>/humidity maintained (Zeiss, Oberkochen, Germany). Imaging was performed using a C-Apochromat 63×/1.2W Korr UV-VIS-IR lens (Zeiss, Oberkochen, Germany) using an optical zoom of 1 and a line average of 8.

**Fixed cell samples for colocalization analysis.** Hydrophobic barriers were drawn on #1.5H coverslips (Menzel Glaser, Leicestershire, UK) using a mini-PAP PEN (Life Technologies, California, USA) and the resulting wells coated with 0.1 mg/mL poly-L-lysine (Sigma Aldrich, Missouri, USA) and dried for >2 h. OTI T cells were pre-labelled with annexin V-Alexa Fluor 568 (Invitrogen, California, USA) for 10 min at room temperature in 0.1% BSA DMEM. After washing three times in 0.1% BSA DMEM, cells were then treated with WT-GFP-PRF for 30 min at 37 °C, washed three times and added to the wells. The cells were allowed to adhere for 10 min at 37 °C, and the wells washed gently with Hanks Balanced Salt Solution (HBSS, Sigma Aldrich, Missouri, USA) containing 2.5 mM CaCl<sub>2</sub> and 1 mM MgCl<sub>2</sub> (both from Sigma-Aldrich, Missouri, USA) to remove any unbound cells. Cells were fixed with 4% EM Grade paraformaldehyde (Electron Microscopy Sciences, Pennsylvania, USA) (in HBSS, with 2.5 mM CaCl<sub>2</sub>) for 30 min at room temperature and washed with 0.1 M lysine (Sigma-Aldrich, Missouri, USA) in HBSS with 2.5 mM CaCl<sub>2</sub>. After 30 min, lysine was removed, and samples washed four times with HBSS with 2.5 mM CaCl<sub>2</sub>. HBSS containing 2.5 mM CaCl<sub>2</sub> and 2% BSA was then added to the wells and incubated for 1 h at room temperature (with gentle shaking) to block non-specific antibody binding. A 1:100 stock dilution of GFP-tag polyclonal antibody-Alexa Fluor 488 (Invitrogen, California, USA) and 2 µg/mL CTxB-Alexa Fluor 647 (Molecular Probes, Oregon, USA) in HBSS containing 2.5 mM CaCl<sub>2</sub> and 2% BSA was then added to wells and incubated overnight at 4 °C. The cells were washed four times and incubated with 5 µg/mL Hoechst 34580 (Life Technologies, California, USA) for 30 min at room temperature. Cells were subsequently washed four times and allowed to dry before being mounted onto slides using Vectashield mounting medium (H1000, Vector Laboratories, California, USA) and sealed.

Fixed samples (Fig. 7a, b) were imaged using a Zeiss Elyra PS.1 microscope, using sequential imaging in line-scan mode. A Plan-Apochromat 63×/1.4 Oil DIC lens (Zeiss, Oberkochen, Germany) was used with zoom set to 2 and a pixel size of 70 nm. Frame size was set to 1024 × 1024 and samples were imaged using a line average of 8 and a z-stack interval of 200 nm. Background fluorescence levels for each channel were obtained using negative control images (primary antibody omitted) of the same acquisition setting and used to set thresholds for colocalization analysis. A channel alignment slide containing 200 nm multispec beads (Zeiss, Oberkochen, Germany) was imaged and used as a reference to correct for chromatic aberration. An ImageJ macro was written to segment individual cells from a field of view and to create mask channels in Fiji/ImageJ.

Colocalization analysis was performed on individual cells using Imaris 8.4.2 (Bitplane, Belfast, UK). The analysis was performed in the mask channels created previously. The threshold of each channel was set as the maximum intensity value of the negative control. The percentage of colocalization of a channel (Fig. 7b) was calculated as the sum of colocalized intensity above the threshold divided by the sum of total intensity above the threshold:

$$\text{Colocalization} = \frac{\sum I_{\text{above threshold}}^{\text{colocalized}}}{\sum I_{\text{above threshold}}^{\text{total}}} \times 100. \quad (1)$$

**Reporting Summary.** Further information on research design is available in the Nature Research Reporting Summary linked to this article.

## Data availability

Data supporting the findings of this manuscript are available from the corresponding authors upon reasonable request. A reporting summary for this Article is available as a Supplementary Information file. The source data underlying Figs. 1, 2c, 3a, 4, 5b, 6b, c, 7b, and Supplementary Figs. 1, 3b, c, 7, and 8b are provided as a Source Data file.



Received: 18 June 2019; Accepted: 6 November 2019;

Published online: 27 November 2019

## References

- Voskoboinik, I., Whisstock, J. C. & Trapani, J. A. Perforin and granzymes: function, dysfunction and human pathology. *Nat. Rev. Immunol.* **15**, 388–400 (2015).
- Golstein, P. & Griffiths, G. M. An early history of T cell-mediated cytotoxicity. *Nat. Rev. Immunol.* **18**, 527–535 (2018).
- Stepp, S. & Dufourcq-Lagelouse, R. Perforin gene defects in familial hemophagocytic lymphohistiocytosis. *Science* **286**, 1957–1959 (1999).
- De Saint Basile, G., Ménasché, G. & Fischer, A. Molecular mechanisms of biogenesis and exocytosis of cytotoxic granules. *Nat. Rev. Immunol.* **10**, 568–579 (2010).
- Law, R. H. P. et al. The structural basis for membrane binding and pore formation by lymphocyte perforin. *Nature* **468**, 447–451 (2010).
- Leung, C. et al. Real-time visualization of perforin nanopore assembly. *Nat. Nanotechnol.* **12**, 467–473 (2017).
- Basu, R. et al. Cytotoxic T cells use mechanical force to potentiate target cell killing. *Cell* **165**, 100–110 (2016).
- Lopez, J. A. et al. Rapid and unidirectional perforin pore delivery at the cytotoxic immune synapse. *J. Immunol.* **191**, 2328–2334 (2013).
- Tschopp, J., Schäfer, S., Masson, D., Peitsch, M. C. & Heusser, C. Phosphorylcholine acts as a Ca<sup>2+</sup>-dependent receptor molecule for lymphocyte perforin. *Nature* **337**, 272–274 (1989).
- Antia, R., Schlegel, R. A. & Williamson, P. Binding of perforin to membranes is sensitive to lipid spacing and not headgroup. *Immunol. Lett.* **32**, 153–157 (1992).
- Balaji, K. N., Schaschke, N., Machleidt, W., Catalfamo, M. & Henkart, P. A. Surface cathepsin B protects cytotoxic lymphocytes from self-destruction after degranulation. *J. Exp. Med.* **196**, 493–503 (2002).
- Baran, K. et al. Cytotoxic T lymphocytes from cathepsin B-deficient mice survive normally in vitro and in vivo after encountering and killing target cells. *J. Biol. Chem.* **281**, 30485–30491 (2006).
- Cohen, A. et al. Surface CD107a / LAMP-1 protects natural killer cells from degranulation-associated damage. *Blood* **122**, 1411–1418 (2013).
- Jenkins, M. R. et al. Failed CTL/NK cell killing and cytokine hypersecretion are directly linked through prolonged synapse time. *J. Exp. Med.* **212**, 307–317 (2015).
- Lopez, J. A. et al. Perforin forms transient pores on the target cell plasma membrane to facilitate rapid access of granzymes during killer cell attack. *Blood* **121**, 2659–2668 (2013).
- Traore, D. A. K. et al. Defining the interaction of perforin with calcium and the phospholipid membrane. *Biochem. J.* **456**, 323–335 (2013).
- Ruan, Y. et al. Membrane damaging activity involves arc formation and lineaction – implication for listeria monocytogenes escape from phagocytic vacuole. *PLoS Pathog.* **12**, 1–18 (2016).
- Mulvihill, E. et al. Mechanism of membrane pore formation by human gasdermin D. *EMBO J.* **37**, e98321 (2018).
- Metkar, S. S. et al. Perforin oligomers form arcs in cellular membranes: a locus for intracellular delivery of granzymes. *Cell Death Differ.* **22**, 74–85 (2015).
- Leung, C. et al. Stepwise visualization of membrane pore formation by suliyisin, a bacterial cholesterol-dependent cytolysin. *Elife* **3**, e04247 (2014).
- Simons, K. & Vaz, W. L. C. Model systems, lipid rafts, and cell membranes. *Annu. Rev. Biophys. Biomol. Struct.* **33**, 269–295 (2004).
- Connell, S. D., Heath, G., Olmsted, P. D. & Kisel, A. Critical point fluctuations in supported lipid membranes. *Faraday Discuss.* **161**, 91–111 (2013).
- Veatch, S. L. & Keller, S. L. Miscibility phase diagrams of giant vesicles containing sphingomyelin. *Phys. Rev. Lett.* **94**, 148101 (2005).
- Marsh, D. *Handbook of Lipid Bilayers* (CRC Press, 2013).
- Massey, J. B. & Pownall, H. J. The polar nature of 7-ketocholesterol determines its location within membrane domains and the kinetics of membrane microsububilization by apolipoprotein A-I. *Biochemistry* **44**, 10423–10433 (2005).
- Owen, D. M., Rentero, C., Magenau, A., Abu-Siniyeh, A. & Gaus, K. Quantitative imaging of membrane lipid order in cells and organisms. *Nat. Protoc.* **7**, 24–35 (2012).
- Leventis, P. A. & Grinstein, S. The distribution and function of phosphatidylserine in cellular membranes. *Annu. Rev. Biophys.* **39**, 407–427 (2010).
- Elliott, J. I. et al. Membrane phosphatidylserine distribution as a non-apoptotic signalling mechanism in lymphocytes. *Nat. Cell Biol.* **7**, 808–816 (2005).
- Koopman, D. et al. Annexin V for flow cytometric detection of phosphatidylserine expression on B cells undergoing apoptosis. *Blood* **84**, 11–12 (1994).
- Metkar, S. S. et al. Perforin rapidly induces plasma membrane phospholipid flip-flop. *PLoS ONE* **6**, e24286 (2011).
- Fischer, K. et al. Antigen recognition induces phosphatidylserine exposure on the cell surface of human CD8+ T cells. *Blood* **108**, 4094–4101 (2006).
- Dillon, S. R., Mancini, M., Rosen, A. & Schlessel, M. S. Annexin V binds to viable B cells and colocalizes with a marker of lipid rafts upon B cell receptor activation. *J. Immunol.* **164**, 1322–1332 (2000).
- Richter, R. P., Maury, N. & Brissson, A. R. On the effect of the solid support on the interleaflet distribution of lipids in supported lipid bilayers. *Langmuir* **21**, 299–304 (2005).
- Gaus, K., Chklovskaya, E., Fazekas De St. Groth, B., Jessup, W. & Harder, T. Condensation of the plasma membrane at the site of T lymphocyte activation. *J. Cell Biol.* **171**, 121–131 (2005).
- Owen, D. M. et al. High plasma membrane lipid order imaged at the immunological synapse periphery in live T cells. *Mol. Membr. Biol.* **27**, 178–189 (2010).
- Burack, W. R., Lee, K.-H., Holdorf, A. D., Dustin, M. L. & Shaw, A. S. Cutting edge: quantitative imaging of raft accumulation in the immunological synapse. *J. Immunol.* **169**, 2837–2841 (2002).
- Zech, T. et al. Accumulation of raft lipids in T-cell plasma membrane domains engaged in TCR signalling. *EMBO J.* **28**, 466–476 (2009).
- Ma, Y., Poole, K., Goyette, J. & Gaus, K. Introducing membrane charge and membrane potential to T cell signaling. *Front. Immunol.* **8**, 1513 (2017).
- Seedhom, M. O., Jellison, E. R., Daniels, K. A. & Welsh, R. M. High frequencies of virus-specific CD8+ T-cell precursors. *J. Virol.* **83**, 12907–12916 (2009).
- Bocharov, G., Argilaguet, J. & Meyerhans, A. Understanding experimental LCMV infection of mice: the role of mathematical models. *J. Immunol. Res.* **2015**, 739706 (2015).
- Brennan, A. J. et al. Protection from endogenous perforin: glycans and the C terminus regulate exocytic trafficking in cytotoxic lymphocytes. *Immunity* **34**, 879–892 (2011).
- Lopez, J. A., Brennan, A. J., Whisstock, J. C., Voskoboinik, I. & Trapani, J. A. Protecting a serial killer: pathways for perforin trafficking and self-defence ensure sequential target cell death. *Trends Immunol.* **33**, 406–412 (2012).
- House, I. G. et al. Regulation of perforin activation and pre-synaptic toxicity through C-terminal glycosylation. *EMBO Rep.* **18**, e201744351 (2017).
- Wu, W., Shi, X. & Xu, C. Regulation of T cell signalling by membrane lipids. *Nat. Rev. Immunol.* **16**, 690–701 (2016).
- Hope, M. J., Bally, M. B., Webb, G. & Cullis, P. R. Production of large unilamellar vesicles by a rapid extrusion procedure. Characterization of size distribution, trapped volume and ability to maintain a membrane potential. *Biochim. Biophys. Acta Biomembr.* **812**, 55–65 (1985).
- Kremer, J. R., Mastronarde, D. N. & McIntosh, J. R. Computer visualization of three-dimensional image data using IMOD. *J. Struct. Biol.* **116**, 71–76 (1996).
- Dang, T. X., Hotze, E. M., Rouiller, I., Tweten, R. K. & Wilson-Kubalek, E. M. Prepore to pore transition of a cholesterol-dependent cytolysin visualized by electron microscopy. *J. Struct. Biol.* **150**, 100–108 (2005).
- Schindelin, J. et al. Fiji: an open-source platform for biological-image analysis. *Nat. Methods* **9**, 676–682 (2012).
- Sutton, V. R. et al. Serglycin determines secretory granule repertoire and regulates natural killer cell and cytotoxic T lymphocyte cytotoxicity. *FEBS J.* **283**, 947–961 (2016).
- Pham, K. et al. Asymmetric cell division during T cell development controls downstream fate. *J. Cell Biol.* **210**, 933–950 (2015).
- Sutton, V. R. et al. Measuring cell death mediated by cytotoxic lymphocytes or their granule effector molecules. *Methods* **44**, 241–249 (2008).
- Aron, M. et al. Spectral imaging toolbox: segmentation, hyperstack reconstruction, and batch processing of spectral images for the determination of cell and model membrane lipid order. *BMC Bioinformatics* **18**, 1–8 (2017).

## Acknowledgements

We thank Richard Thorogate and Shu Chen for technical support; Natalya Lukoyanova for advice on electron microscopy experiments; Helen Saibil, Ricardo Henriques and Dylan Owen for discussions and comments on the manuscript. We also thank the following Peter MacCallum Cancer Centre core facilities for technical support: Ralph Rossi and the Flow Cytometry facility, Sarah Ellis and the Centre for Advanced Histology and Microscopy. This work has been funded by the NHMRC Project Grant (1128587), the NHMRC Fellowship (1059126), the BBSRC (BB/J005932/1, BB/J006254/1 and BB/N015487/1); the EPSRC (EP/M028100/1); and the Sackler Foundation. This research was supported by the Australian Cancer Research Foundation (for the Peter MacCallum Cancer Centre core facilities).

## Author contributions

J.A.R.-S. designed, performed and analysed cell-based and microscopy assays and wrote the paper. A.W.H. designed, performed and analysed AFM and EM experiments



and co-wrote the paper. T.N. performed and analysed cell-based assays. J.A.L. performed cell-based assays. H.-J.C. designed and analysed the microscopy-based assays. S.V. and A. C. expressed and purified perforin. J.A.T. conceived the study and co-wrote the paper. B. W.H. and I.V. contributed equally, co-led this work, and jointly conceived and supervised the study, designed the experiments, analysed the data and wrote the paper. All authors read and commented on the paper.

### Competing interests

The authors declare no competing interests.

### Additional information

**Supplementary information** is available for this paper at <https://doi.org/10.1038/s41467-019-13385-x>.

**Correspondence** and requests for materials should be addressed to B.W.H. or I.V.

**Peer review information** *Nature Communications* thanks Matthias Amrein, Rodney Tweten and the other, anonymous, reviewer(s) for their contribution to the peer review of this work. Peer reviewer reports are available.

**Reprints and permission information** is available at <http://www.nature.com/reprints>

**Publisher's note** Springer Nature remains neutral with regard to jurisdictional claims in published maps and institutional affiliations.



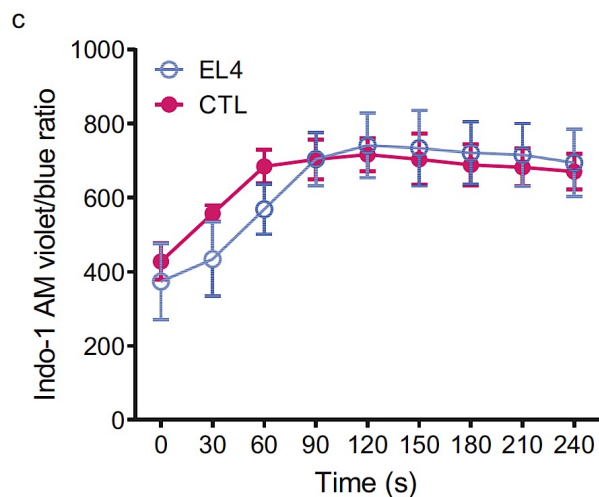
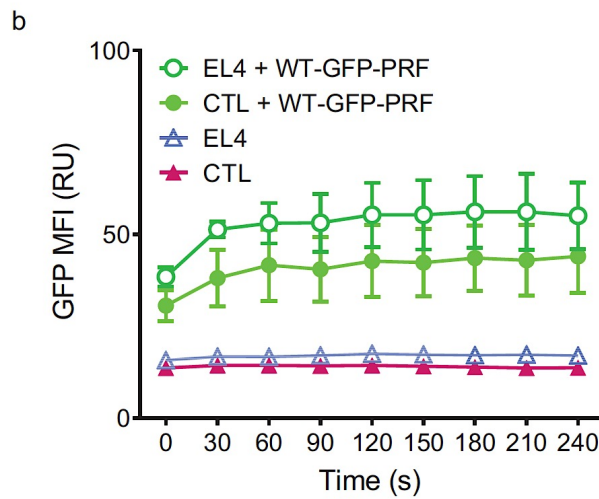
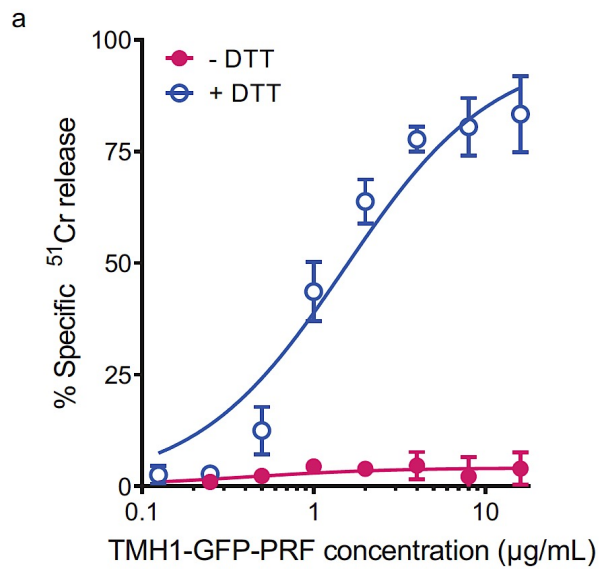
**Open Access** This article is licensed under a Creative Commons Attribution 4.0 International License, which permits use, sharing, adaptation, distribution and reproduction in any medium or format, as long as you give appropriate credit to the original author(s) and the source, provide a link to the Creative Commons license, and indicate if changes were made. The images or other third party material in this article are included in the article's Creative Commons license, unless indicated otherwise in a credit line to the material. If material is not included in the article's Creative Commons license and your intended use is not permitted by statutory regulation or exceeds the permitted use, you will need to obtain permission directly from the copyright holder. To view a copy of this license, visit <http://creativecommons.org/licenses/by/4.0/>.

© The Author(s) 2019

# **Lipid order and charge protect killer T cells from accidental death**

## **Supplementary Information**

Jesse A. Rudd-Schmidt, Adrian W. Hodel, Tahereh Noori, Jamie A. Lopez, Hyun-Jung Cho, Sandra Verschoor, Annette Ciccone, Joseph A. Trapani, Bart W. Hoogenboom & Ilia Voskoboinik



**Supplementary Figure 1. Control experiments validating TMH1-GFP-PRF mutant and Ca<sup>2+</sup> flux measurements.**

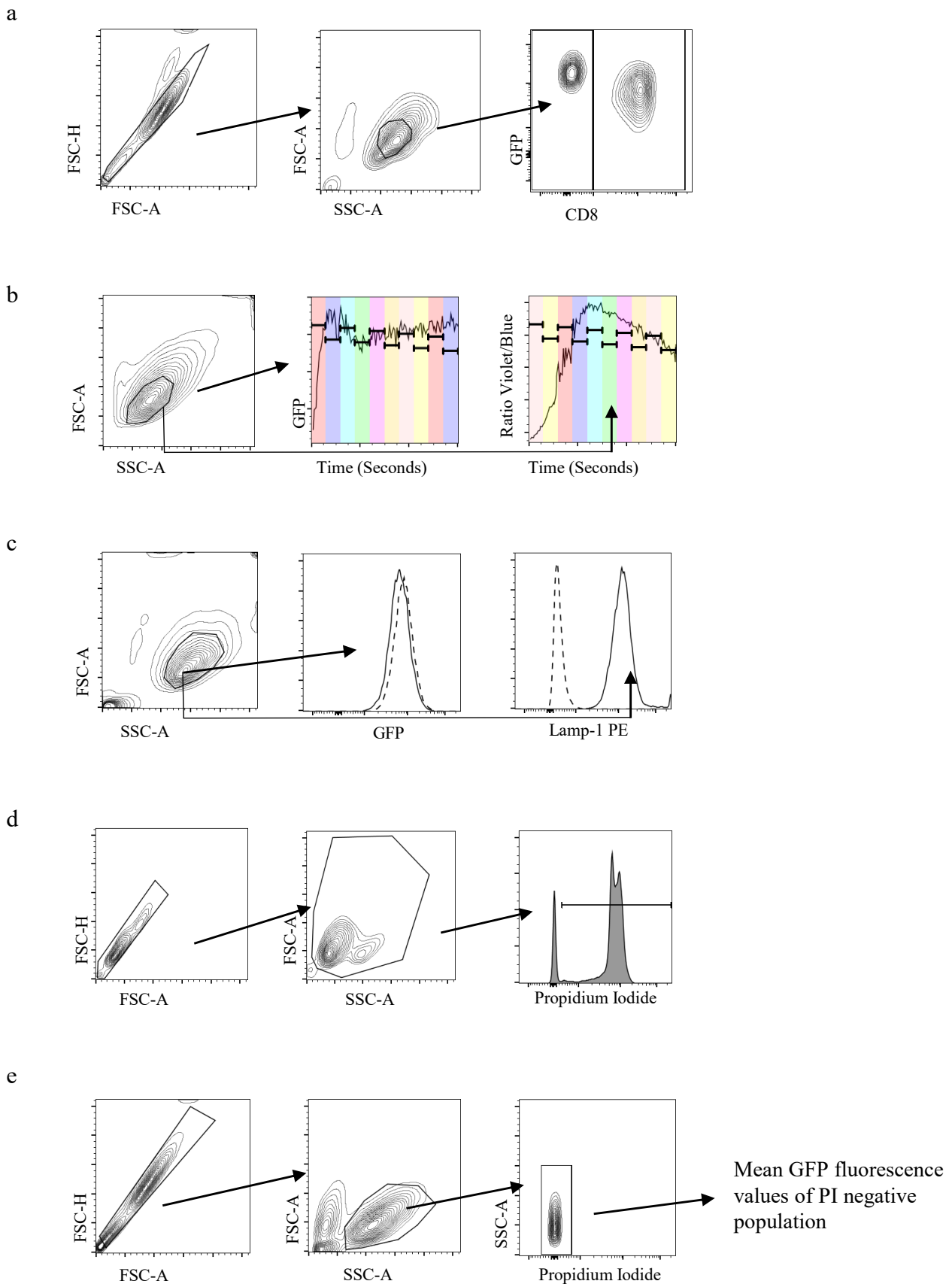
**a**, Functionality of TMH1-GFP-PRF as assessed by <sup>51</sup>Cr release assay. Recombinant TMH1-GFP-PRF is not cytotoxic to EL4 cells over a wide range of perforin concentrations (-DTT). However,

when 0.75 mM DTT is added to this cell-bound perforin, the engineered disulphide-bond in TMH1-GFP-PRF is unlocked. As a consequence, the functionality of TMH1-GFP-PRF is restored, as here demonstrated by its cytotoxicity to the EL4 cells ( $^{51}\text{Cr}$  release increasing with TMH1-GFP-PRF concentration, +DTT). Each data point represents a mean ( $\pm$  standard deviation, SD) of 3 independent experiments; curves represent Michaelis-Menten fits to the data. For an extensive validation of the behaviour and functionality (+DTT) of the TMH1-PRF mutant see <sup>1</sup>.

**b**, WT-GFP-PRF was dosed such that similar amounts bound to the EL4 cells and CTLs. To this end, firstly a sub-lytic amount of WT-GFP-PRF was determined for the EL4 cells (on the day of each experiment), and then increasing amounts of WT-GFP-PRF were added to the CTLs until a similar MFI was achieved, and experiments were then conducted with these optimized conditions. Each data point represents a mean ( $\pm$  SD) of 3 independent experiments. An unpaired t-test performed on EL4 + WT-GFP-PRF and CTL + WT-GFP-PRF shows  $P < 0.05$  for  $t = 30$  s, but no significant difference for all other time points.

**c**, Indo-1 AM violet/blue fluorescence ratio (400 nm/475 nm) increases in both cell types when  $\text{Ca}^{2+}$  influx is induced by the  $\text{Ca}^{2+}$  ionophore ionomycin, demonstrating that both types of cells show a similar response to Indo-1 AM labelling. Each data point represents a mean ( $\pm$  SD) of 3 independent experiments.

Source data for all panels are provided as a Source Data file.



**Supplementary Figure 2. Gating Strategies used for flow cytometry analysis.**

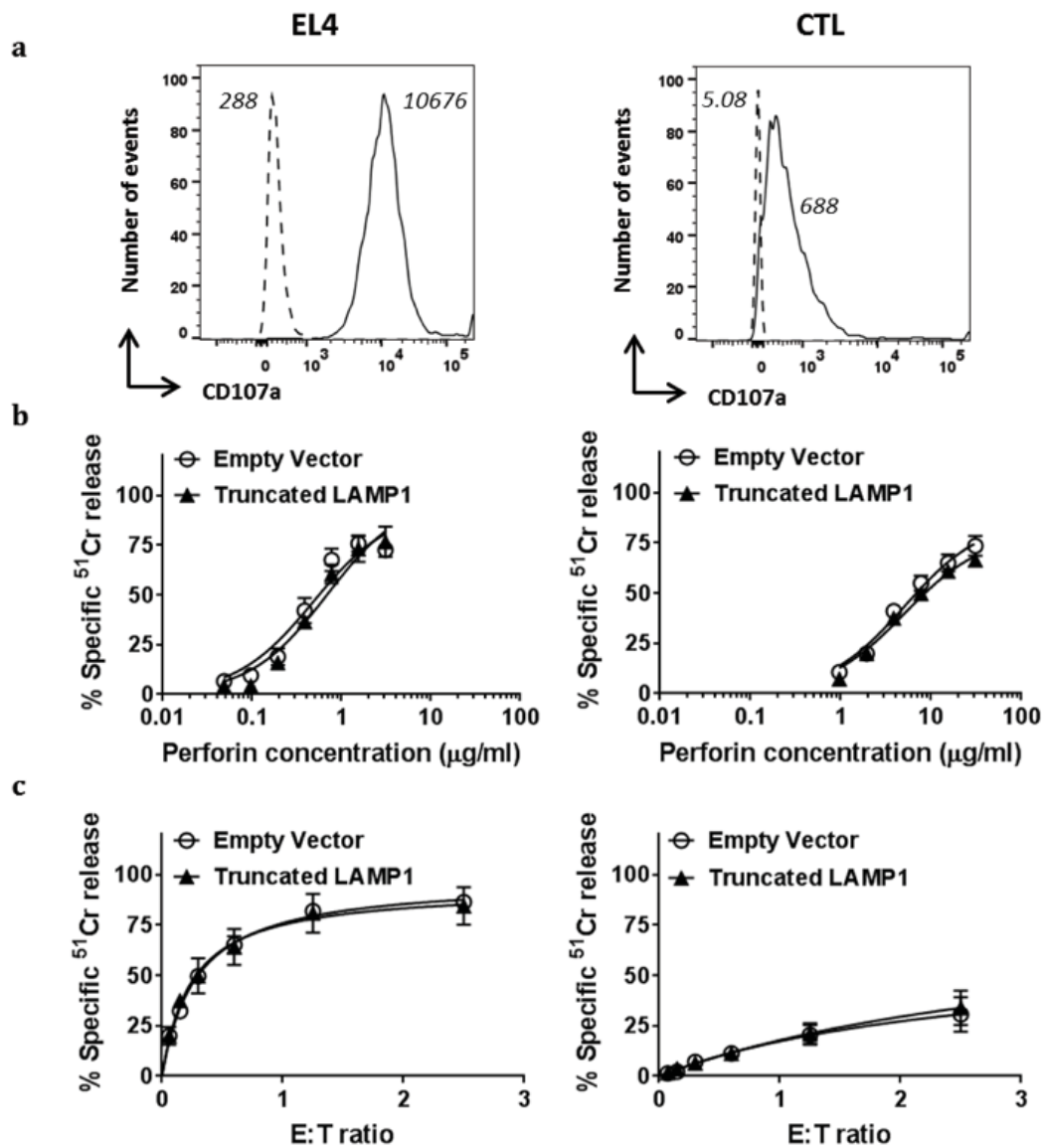
**a**, Gating strategy used to analyse cells of the same size within a mixture of CD8<sup>+</sup> T cells and EL4 target cells for either perforin vs CD8 (Figs. 1b, 2a,b,c) or GM1 vs CD8 (Supplementary Fig. 8).

**b,** Gating strategy used to analyse EL4 or CD8<sup>+</sup> T cells of the same size for perforin binding over time (Supplementary Fig. 1b) and Indo-1 AM fluorescence (Violet/Blue) over time (Fig. 1c, Supplementary Fig. 1c).

**c,** Gating strategy used to analyse equal GFP expression of EL4 and CD8<sup>+</sup> T cells transduced with either empty MSCV-GFP (dashed line) or truncated LAMP-1-MSCV-GFP (solid line) (Supplementary Fig. 3), and surface LAMP-1 expression (as detected by anti-LAMP1-PE antibodies) of EL4 or CD8<sup>+</sup> T cells transduced with truncated LAMP-1.

**d,** Gating strategy used to analyse cell death (propidium iodide positivity) of EL4 or CD8<sup>+</sup>T cells treated with 7KC (Fig. 4b) or with 7KC and perforin (Fig. 4e).

**e,** Gating strategy used to analyse the mean GFP fluorescence of CD8<sup>+</sup> T cells treated with 7KC and then incubated with TMH-GFP perforin (Fig. 4d).



**Supplementary Figure 3. High surface levels of CD107a (LAMP-1) do not protect cells from recombinant perforin lysis or killing by CTLs.**

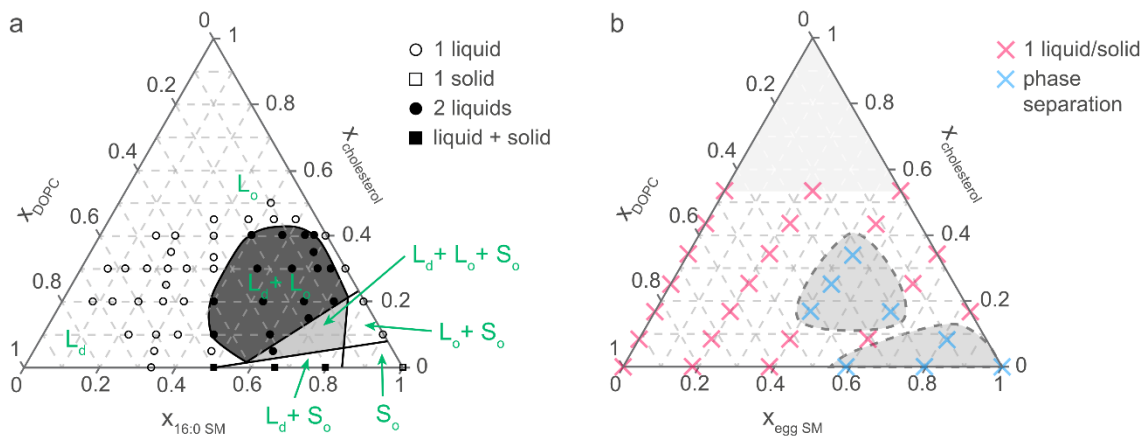
**a**, Surface staining for CD107a of EL4 and *Prf1*<sup>-/-</sup> OTI (CTLs). EL4 cells (left) transduced with a truncated form of CD107a<sup>2</sup> (shown by solid line) have a 37-fold higher surface expression of CD107a than EL4 cells transduced with an empty vector (shown by dashed line), as detected by surface staining with anti-CD107a-Phycoerythrin antibody. CTLs (right) transduced with the same truncated form of CD107a (shown by solid line) have a 135-fold higher surface expression of CD107a than CTL cells transduced with an empty vector (shown by dashed line). Both histograms are representative examples of surface staining performed on the day of every experiment, the number of events has been standardized to the mode to allow clear comparison of both histograms and geometric mean fluorescence intensity (MFI) values from which fold difference values were calculated are shown next to each peak.

**b**,  $^{51}\text{Cr}$  release of EL4 (left) and CTL (right) cells upon exposure to recombinant WT-PRF. There is no significant difference in perforin sensitivity between cells transduced with an empty vector and with truncated CD107a.

**c**,  $^{51}\text{Cr}$  release of SIINFEKL labelled EL4 (left) and CTL (right) target cells incubated with activated WT OTI CTLs, as a function of the ratio of effector to target cells (E:T ratio). Again, there is no significant difference in sensitivity to killing between target cells transduced with an empty vector or with truncated CD107a, for both EL4 and CTL target cells.

For **b**, and **c**, each data point represents a mean ( $\pm$  standard error of mean) of 3 independent experiments; curves represent Michaelis-Menten fits to the data. Source data for these two panels are provided as a Source Data file.



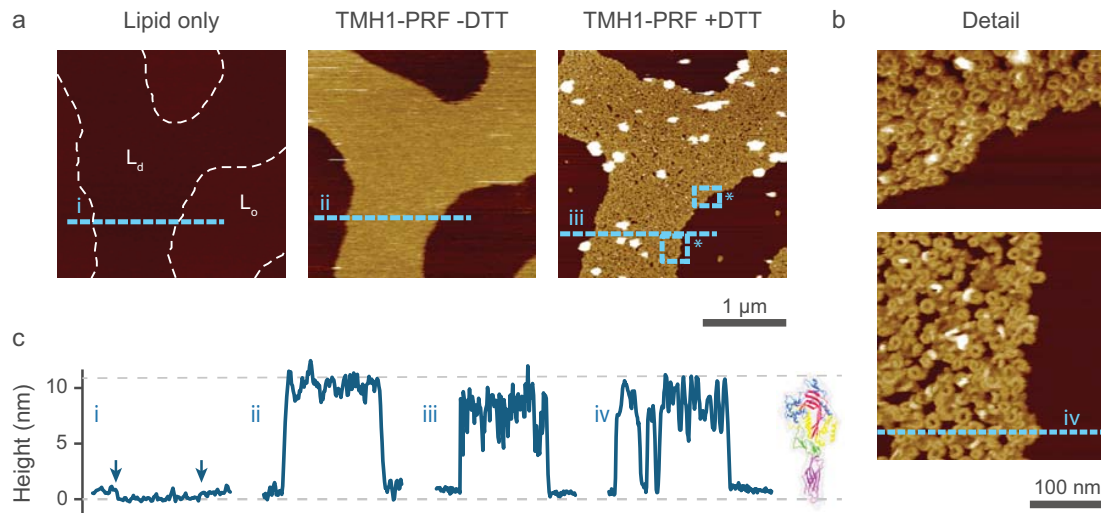


**Supplementary Figure 4. Phases and phase coexistence in ternary DOPC/SM/cholesterol lipid systems.**

**a**, Map of DOPC/16:0 SM/cholesterol mixtures, and the lipid phases in giant unilamellar vesicles (adapted from Veatch and Keller 2005<sup>3</sup>, with information from Marsh 2013<sup>4</sup>). Mixtures in the bottom left corner (DOPC-rich) are in the  $L_d$  state. Membrane order increases by addition of cholesterol ( $L_o$  in the top regions) or 16:0 SM ( $S_o$  in the right corner). Phase separation is observed in mixtures located in the lower right side of the triangular map.

**b**, Map of DOPC/egg SM/cholesterol mixtures as used for our experiments. Mixtures that show phase separation – detected via the appearance of domains with distinct membrane thicknesses – in our experiments are marked with a blue “x”, and the remaining, single-phase compositions with a red “x”. The phase separated mixtures are encircled by a dashed line and further highlighted with a grey background. The areas that show phase separation are similar in the overview based on literature values **(a)** and in our own experiments in **(b)**.

Minor difference may arise because, in contrast to the 16:0 SM used in **a**, the egg SM used in **b** is a mixture of different SM species (though mostly 16:0 SM as per supplier specifications) that inherently shows phase separation. Also note that we tested mixtures containing up to 53% cholesterol. Above ca. 66% in PC/cholesterol mixtures, cholesterol is known to crystallize. The data in both maps was recorded at 37 °C.

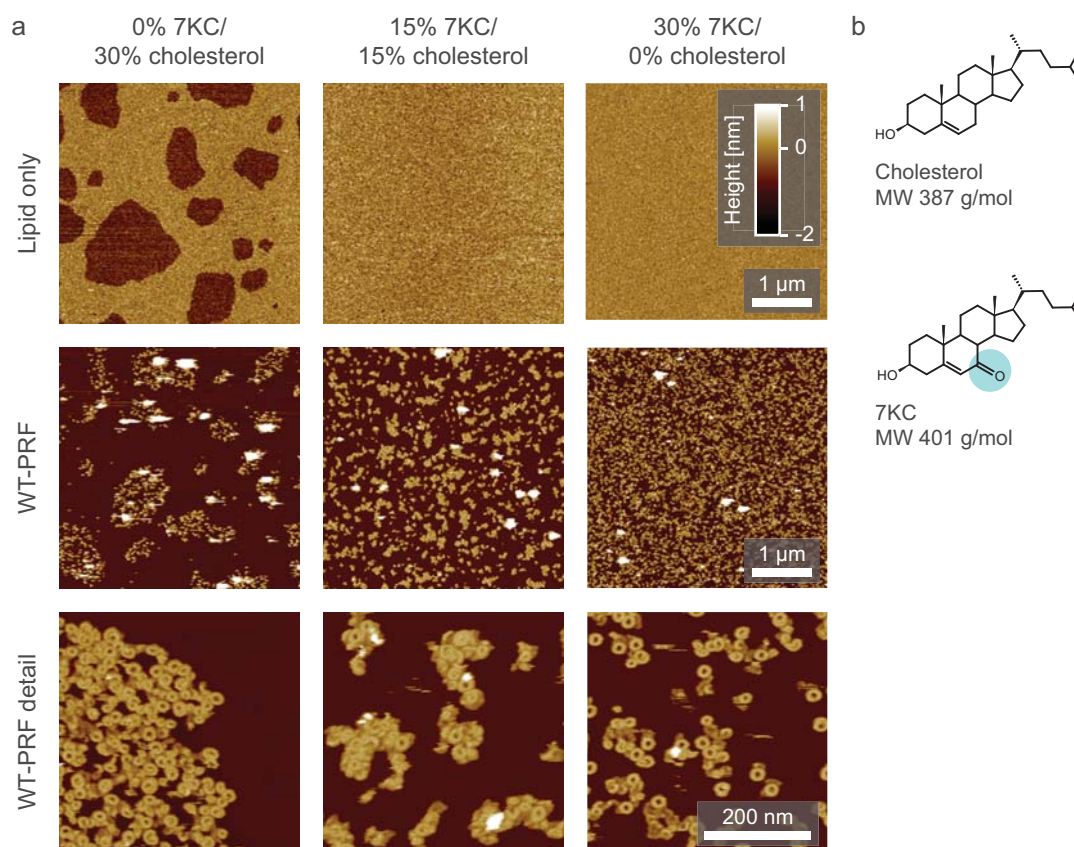


**Supplementary Figure 5. Prepore-locked TMH1-PRF binds to disordered domains on phase separated lipid membranes.**

**a**, AFM images of an approximately equimolar DOPC/egg SM/cholesterol supported lipid bilayer, showing phase separation between liquid disordered ( $L_d$ ) and liquid ordered ( $L_o$ ) domains, with the  $L_o$  phase appearing higher (thicker) than the  $L_d$  phase in the “lipid only” image. The phase boundaries are highlighted by dashed white lines. Prepore-locked perforin (TMH1-PRF -DTT) appears as diffuse plateaus due to its mobile nature<sup>1</sup>, exclusively bound to the  $L_d$  domains. Upon exposure to DTT, these mobile prepores transform into static pores (TMH1-PRF +DTT).

**b**, Higher-magnification images of the areas indicated by the dashed blue rectangles in **a**. The  $L_d$  domain shows a dense coverage of arc- and ring-shaped pores, whereas the  $L_o$  domains remains empty.

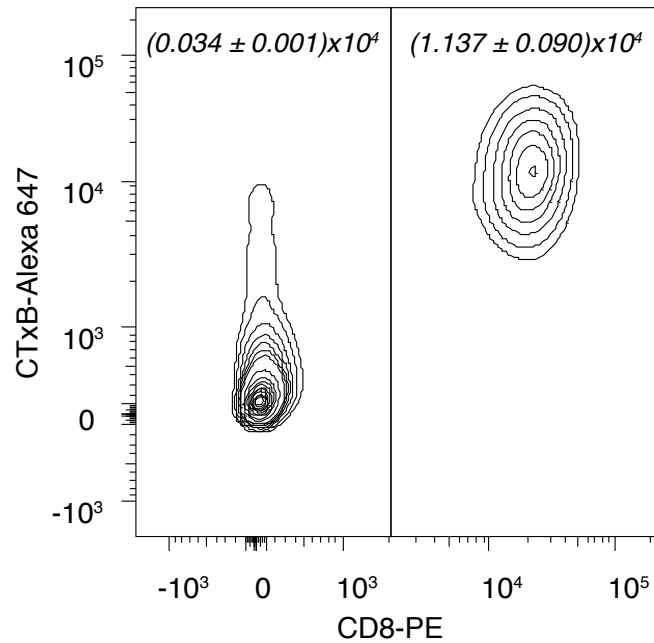
**c**, Height profiles as recorded along the blue, dashed lines in the AFM images in **a** and **b**. The phase separation on the empty membrane (i) is visible as a 0.5-1 nm height difference, and the phase boundaries are indicated by vertical arrows. Addition of TMH1-PRF (-DTT/+DTT, ii-iv) leads to the formation of ca. 11 nm high features, corresponding to the height of perforin prepores and pores<sup>1,5,6</sup>. Grey, dashed lines indicate the height of the membrane (0 nm) and of a perforin monomer (11 nm<sup>5</sup>). The differences in measured perforin height between traces ii, iii and iv are attributed to variations in the applied forces in the AFM experiments. The sample was incubated and imaged at 37 °C. Colour (height) scale as in Fig. 3b.



**Supplementary Figure 6. Effect of 7KC on membrane order, as assessed by AFM.**

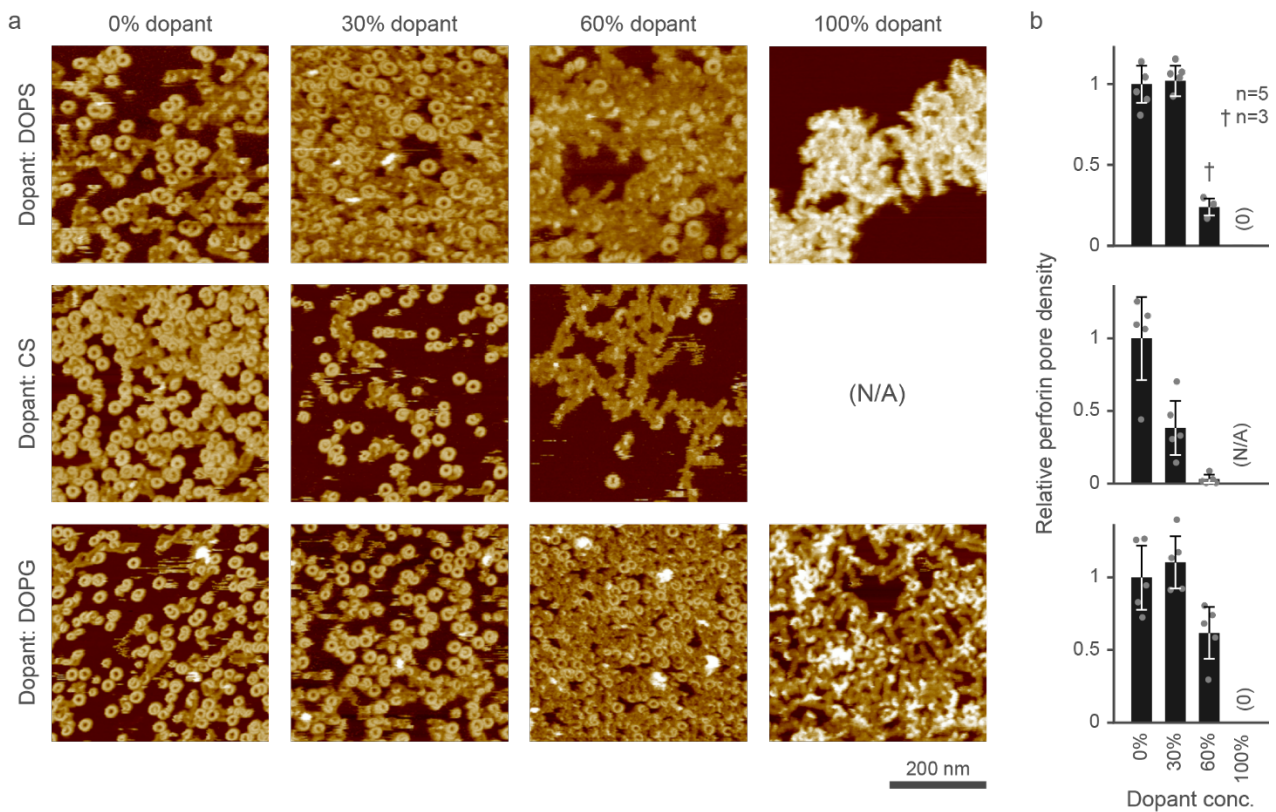
**a**, AFM images of DOPC/egg SM/sterol 20:50:30 supported lipid bilayers, as a function of sterol content (7KC, cholesterol). The images show membranes before and after exposure to 150 nM WT-PRF. Note that in the top row, the colour scale was enhanced to better show phase separation, while the middle and bottom rows use the same colour scale as Fig. 3b-d. For 0% 7KC / 30% cholesterol, these lipids phase-separate into  $L_d$  and  $L_o$  domains (respective dark and bright areas in the “lipid only” image, see also Fig. 3a,b and Supplementary Fig. 4). Exposure to WT-PRF leads to pore formation exclusively in  $L_d$  domains, consistent with Fig. 3 and Supplementary Fig. 4. For 15% 7KC / 15% cholesterol, no phase separation is observed at micrometre length scales, and poriferin pores are formed more uniformly over the sample surface. At nanometre length scales (bottom row), some phase separation persists, here visible by the clustering of poriferin pores (presumably bound to nanometre-scale  $L_d$  domains). For 30% 7KC / 0% cholesterol, poriferin binds uniformly over the whole sample surface without noticeable pore clustering in domains.

**b**, Chemical structures and molecular weights for cholesterol and 7KC, with the additional ketone group highlighted. All samples were incubated and imaged at 37 °C.



**Supplementary Figure 7. GM1 surface staining of CTL and EL4 cells by cholera toxin subunit B (CTxB) Alexa 647.**

GM1 surface staining by recombinant cholera toxin subunit B Alexa 647. GM1 intensity (represented by CTxB) has been plotted against CD8<sup>+</sup> positivity to identify CD8<sup>+</sup> T cells in a 1:1 mixture of EL4 and OTI T cells (cells are gated for same size as detailed for perforin binding experiments in manuscript). Average MFI ( $\pm$  SD) of CTxB-Alexa 647 from 3 independent experiments is included for both CD8 positive and negative cells and provided as a Source Data file.



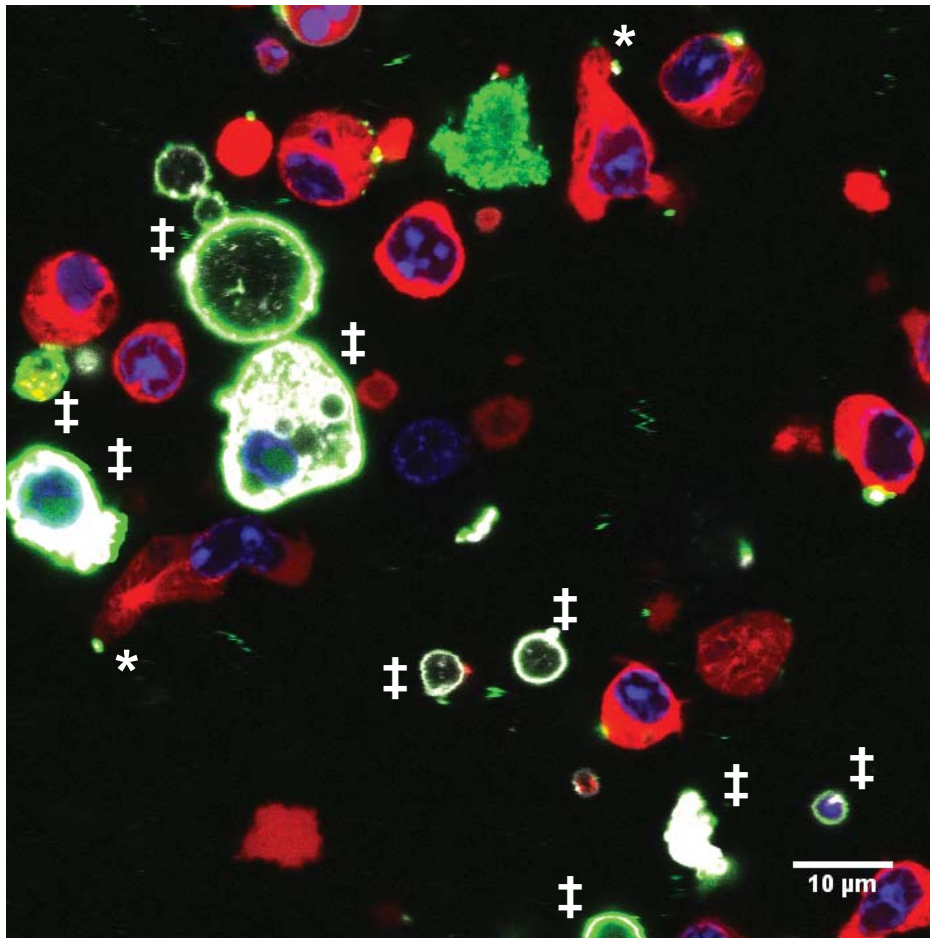
**Supplementary Figure 8. Perforin forms non-porating clusters on the negatively charged membranes.**

Perforin pore formation on DOPC model membranes doped with the negatively charged membrane components DOPS, DOPG (1,2-dioleoyl-sn-glycero-3-phospho-(1'-racglycerol)), and CS (cholesterol sulfate), as assessed by AFM.

**a**, Representative images of the sample surfaces of samples containing 0%, 30%, 60% and 100% of either DOPS, DOPG, or CS in DOPC host membranes (for 100% CS, no supported lipid bilayers could be formed). Colour (height) scale as in Fig. 3b.

**b**, Quantification of pore formation (mean  $\pm$  SD) in the samples shown in a, relative to the 0% dopant/100% DOPC reference. The data on DOPS was reproduced from Fig. 5b, for comparison. Source data are provided as a Source Data file.





**Supplementary Figure 9. Unlike target cells, CTL maintain healthy morphological appearance and mobility one hour after addition of WT-GFP-PRF.**

CTLs (red) with clear WT-GFP-PRF signal (green) localized to punctate regions of non-apoptotic PS (white) 1 hour after addition of perforin. Dead target cells and their debris are stained bright green and white (highlighted by white daggers), because of, respectively, their overall WT-GFP-PRF binding and staining for apoptotic PS. Note that on polarized CTLs, non-apoptotic PS is always located within the uropod (white asterisks). Staining is as in Fig. 7c; the data shown here represent a snapshot from Supplementary Video 2.

## Supplementary References

1. Leung, C. *et al.* Real-time visualization of perforin nanopore assembly. *Nat. Nanotechnol.* **12**, 467–473 (2017).
2. Cohnen, A. *et al.* Surface CD107a / LAMP-1 protects natural killer cells from degranulation-associated damage. *Blood* **122**, 1411–1418 (2013).
3. Veatch, S. L. & Keller, S. L. Miscibility Phase Diagrams of Giant Vesicles Containing Sphingomyelin. *Phys. Rev. Lett.* **94**, 148101 (2005).
4. Marsh, D. *Handbook of lipid bilayers*. (CRC Press, 2013).
5. Law, R. H. P. *et al.* The structural basis for membrane binding and pore formation by lymphocyte perforin. *Nature* **468**, 447–51 (2010).
6. Metkar, S. S. *et al.* Perforin oligomers form arcs in cellular membranes: a locus for intracellular delivery of granzymes. *Cell Death Differ.* **22**, 74–85 (2015).



Minerva Access is the Institutional Repository of The University of Melbourne

**Author/s:**

Rudd-Schmidt, Jesse Alexander

**Title:**

Investigating the mechanism of cytotoxic lymphocyte resistance to perforin

**Date:**

2020

**Persistent Link:**

<http://hdl.handle.net/11343/239080>

**File Description:**

Final thesis file

**Terms and Conditions:**

Terms and Conditions: Copyright in works deposited in Minerva Access is retained by the copyright owner. The work may not be altered without permission from the copyright owner. Readers may only download, print and save electronic copies of whole works for their own personal non-commercial use. Any use that exceeds these limits requires permission from the copyright owner. Attribution is essential when quoting or paraphrasing from these works.